Rehabilitation of Fatigue Sensitive Steel Elements Using Shape Memory Alloy/Fiber Reinforced Polymer (SMA/FRP) Composite Overlays

A Dissertation

Presented to

The Faculty of the Department of Civil and Environmental Engineering

University of Houston

In Partial Fulfillment

of the Requirements for the Degree

Doctor of Philosophy

in Civil Engineering

by

Botong Zheng

December 2016

Rehabilitation of Fatigue Sensitive Steel Elements Using Shape Memory Alloy/Fiber Reinforced Polymer (SMA/FRP) Composite Overlays

Botong Zheng

Approved:

Chair of the Committee
Mina Dawood, Associate Professor,
Civil and Environmental Engineering

Committee Members:

Kaspar Willam, Professor
Civil and Environmental Engineering

Kalyana Nakshatrala, Assistant Professor,
Civil and Environmental Engineering

Gangbing Song, Professor,
Mechanical Engineering

Ken White, Professor,
Mechanical Engineering

Suresh K. Khator, Associate Dean,
Cullen College of Engineering

Roberto Ballarini, Professor and Chair,
Civil and Environmental Engineering

Acknowledgements

This research was funded by National Science Foundation (NSF) and the Department of Civil and Environmental Engineering at the University of Houston.

Dr. Mina Dawood granted me the opportunity of advancing my academic career, mentored me through this five-year journey of knowledge and experience harvesting, pardoned me for every forgivable or non-forgivable fault, encouraged me at all of my valleys, and presented me a role model to pursue for lifetime. It is impossible for me to offer back anything of equal value but my genuine respect and gratitude.

I thank my dissertation committee members, Dr. Kasper Willam, Dr. Gangbing Song, Dr. Kalyana Nakshatrala, and Dr. Ken White for their constructive guidance. My thanks extend to Dr. Roberto Ballarini for the valuable opinions on this research.

I offer my special thanks to the staff of the department, Ms. Betsy Roguer, Ms. Cherish Wallace, Mr. Gerald McTigret, and Mr. Jeffrey Miller. The help from my dear colleagues, Dr. Qian Li, Dr. Mossab El-Tahan, Dr. Cheng Shi, Dr. Hossein Karagah, Mr. Mehmet Sahin, Mr. Ben Wang, Mr. Reza Mousavi, and amazing helpers, Ms. Tracy Donoghue, Ms. Cindy Dong, Mr. Felix Vergara, are acknowledged.

To my love Na, thank you for your unconditional trust and love that have given me reasons and strength to become better. I look forward to building our life together for all the years to come.

To my parents, although you cannot read English fluently, my gratitude and love to you are beyond words.

Rehabilitation of Fatigue Sensitive Steel Elements Using Shape Memory Alloy/Fiber Reinforced Polymer (SMA/FRP) Composite Overlays

An Abstract

of a

Dissertation

Presented to

The Faculty of the Department of Civil and Environmental Engineering

University of Houston

In Partial Fulfillment

of the Requirements for the Degree

Doctor of Philosophy

in Civil Engineering

by

Botong Zheng

December 2016

Abstract

This dissertation presents the details of an experimental and numerical program that was conducted to evaluate the effectiveness of a new type of shape memory alloy (SMA)/fiber reinforced polymer (FRP) patch for repairing fatigue-sensitive steel elements. A nickel-titanium-niobium SMA was combined with carbon fiber reinforced polymer (CFRP) to develop a patching system to reinforce fatigue-sensitive steel elements. This thermally-activated system provides a more simple, practical and accessible method for prestressing composite patches than conventional prestressing approaches. Experimental results indicate that the composite increased the average fatigue life of fatigue sensitive elements by 15 and 26 times at stress ranges of 217 and 155 MPa, respectively. A digital image correlation (DIC) system was employed to study the interfacial debonding between the patch and substrate during fatigue loading. The influence of near-crack debonding on the strengthening effects was further studied using finite element (FE) methods.

A linear elastic fracture mechanics (LEFM)-based numerical framework was established to perform a fatigue crack growth (FCG) analysis of steel elements that are reinforced with the SMA/FRP composite patches. The small crack propagation was taken into account using an equivalent initial flaw size (EIFS) method. The numerical framework was validated using the experimental results and the validated model was used to conduct a parametric study. The numerical study indicated two primary mechanisms by which the patches improved the fatigue lives of the repaired details: (i) activation of the SMA induced compressive stresses in the steel near the crack thereby

increasing the critical crack length at which the element failed, and (ii) the CFRP provided a crack bridging effect which reduced the stress range in the steel locally near the crack thereby reducing the crack propagation rate. As a result, the synergistic effect between the SMA and FRP substantially extends the fatigue life of steel element.

It was also found that the patch was more effective at increasing the fatigue lives of elements that were subjected to lower stress ranges. The research findings also indicated that early installation of the SMA/FRP patch results in much higher fatigue life improvement. However, installation of the patch at late stage of crack propagation, such as in an emergency repair can also significantly increase the fatigue life of cracked components providing an opportunity to mobilize a more permanent solution. Collectively, the research findings demonstrate that SMA/FRP patches are a promising new technology for repair of cracks in steel and other metallic structures.

Table of Contents

Acknowledgements ..... **v**

Abstract ..... **vii**

Table of Contents ..... **ix**

List of Figures ..... **xiii**

List of Tables ..... **xviii**

Chapter 1 : Introduction **1**

1.1 Research objectives 2

1.2 Outline of the dissertation 2

Chapter 2 : Literature review **4**

2.1 Fatigue strengthening of metallic structures using FRP 4

2.2 FRP-metal interface debonding under fatigue loading 9

2.3 Estimation of SIF for FRP-patched elements 14

2.3.1 Analytical models 15

2.3.2 FE models 19

2.4 Fatigue crack propagation model 23

2.5 Small crack propagation analysis theories 28

2.6 Characteristics and applications of shape memory alloys 33

2.6.1 Cyclic behavior of superelastic SMA materials 34

2.6.2 Structural damping applications of SMA members 37

2.6.3 Shape memory effect applications of SMA materials 38

2.6.4 Bond between SMA and FRP 40

2.6.5 A thermally-activated self-stressing SMA/FRP composite for fatigue strengthening 43

2.7 Research significance 45

Chapter 3 : Fatigue strengthening of steel members using a thermally-activated self-stressing SMA/FRP system 46

3.1 The thermally-activated SMA/FRP patch 46

3.2 Specimens and test setup 52

3.3 Failure modes 56

3.4 Debonding of the reinforcing patch during fatigue loading 57

3.4.1 Near-crack debonding 59

3.4.2 Plate-end debonding 63

3.4 Fatigue life results 64

3.4.1 Material constants 66

3.4.2 Fatigue strengthening using CFRP 68

3.4.2 Fatigue strengthening using prestressed SMA wires 70

3.4.3 Fatigue strengthening using SMA/CFRP composite system 71

3.5 Summary and discussion 73

Chapter 4 : Investigation of the near-crack debonding between FRP overlay and steel under fatigue loading 76

4.1 Influence of debonding on the crack growth prediction 76

4.2 Prediction of the interfacial debonding 83

4.3 Parametric study 88

4.4 Summary 93

Chapter 5 : Numerical framework 95

5.1 Description of the numerical framework 95

5.1.1 Initial conditions of the FCG analysis (Step 1) 96

5.1.2 SIF calculation of small crack (Step 2) 98

5.1.3 SIF calculation of long crack (Step 3) 98

5.1.4 Crack growth rate calculation (Step 4) 99

5.1.5 Crack growth curve and fatigue life prediction (Steps 5 and 6) 99

5.2 Experimental validation 100

5.2.1 Value of EIFS 100

5.2.2 Boundary crack length 101

5.2.3 SIF calculation 102

5.2.4 Fatigue life and FCG prediction 105

5.3 Parametric study of the SMA/CFRP system 109

5.3.1 Influence of the number of SMA wires 110

5.3.2 Influence of the initial crack length at time of strengthening 112

5.4 Discussions 113

Chapter 6 : Summary, Conclusions and Future work 115

6.1 The effectiveness of the SMA/FRP patch in fatigue strengthening of steel elements 115

6.2 Near-crack debonding between FRP overlay and steel under fatigue loading 117

6.3 Numerical framework to perform the FCG analysis 118

6.4 Limitations 119

6.5 Future work 120

References 123

Appendix A SMA activation data 135

Appendix B DIC data of SMA/CFRP group of specimens 136

Appendix C DIC data of CFRP group of specimens 139

List of Figures

Figure 2.1 Fatigue life improvement using un-prestressed and prestressed FRP ... 8

Figure 2.2 Crack growth induced debonding (Colombi et al. 2003) 10

Figure 2.3 Observed shape of interfacial debonding (Sabelkin et al. 2006)..... 11

Figure 2.4 Trapezoidal debonded region (Huawen et al. 2010) 12

Figure 2.5 Illustration of fatigue damage zone (adapted from Wu et al., 2010)... 13

Figure 2.6 Central-hole steel coupon reinforced with prestressed CFRP strips ... 17

Figure 2.7 Cracked steel I-beam reinforced with prestressed CFRP patch on the bottom flange 18

Figure 2.8 FE model using three-layer technique (Colombi et al. 2003) 20

Figure 2.9 Typical mesh of the crack tip using collapsed 20-node wedge elements 20

Figure 2.10 Skewed curve crack front along thickness of single-side repair (Lee and Lee, 2005) 21

Figure 2.11 U-R relationships for different materials..... 24

Figure 2.12 Schematic drawing of small crack behavior (adapted from Newman et al., 1999) 30

Figure 2.13 Illustration of EIFS(Adpted from Liu and Mahadevan, 2009)..... 31

Figure 3.1 Temperature and recovery stress relationship of the NiTiNb SMA wire 47

Figure 3.2 SMA wires embedded into CFRP tabs 49

Figure 3.3 Illustration of the process of strengthening steel plate with SMA/CFRP patch 50

Figure 3.4 Compressive stress in the steel during SMA activation 52

Figure 3.5 The beach marking (beach marks digitally enhanced for clarity) 55

Figure 3.6. Final failure of the specimens: a) CFRP; b) SMA; c) SMA/CFRP.... 56

Figure 3.7 (a) Illustration of DIC system; (b) DIC system parameters determination 58

Figure 3.8 Surface strain profile of CFRP patched specimen at different numbers of load cycles 60

Figure 3.9 Crack-induced debonding of the specimen before final CFRP rupture 61

Figure 3.10 Definition and calculation of the debonded area from the DIC results 62

Figure 3.11. Illustration of plate-end debonding using the DIC results..... 64

Figure 3.12. Stress range - fatigue live of the tested coupons 65

Figure 3.13. Experimental data of control coupons: (a) Crack growth curves; (b) crack growth rate vs. ΔK 68

Figure 3.14. Crack growth curves of steel and CFRP groups: a) 217 MPa, b) 155 MPa 69

Figure 3.15. ΔK at difference crack lengths of Steel and CFRP groups: (a) 217 MPa; (b) 155 MPa 70

Figure 3.16. Crack growth curves of Steel and SMA groups 71

Figure 3.17. Comparison between CFRP and SMA/CFRP groups 72

Figure 3.18. ΔK at difference crack lengths of CFRP and SMA/CFRP groups ... 73

Figure 4.1. Quarter FE model details (adapted from Abaqus software (Dassault Systèmes Simulia Corp., 2012)) 77

Figure 4.2. The parameters used to define the debonded region 79

Figure 4.3. SIF values of different values of the parameter *c* 80

Figure 4.4. SIF values of different angles 80

Figure 4.5. SIF values of different curvatures 81

Figure 4.6. SIF values vs. debonded area for different crack lengths 82

Figure 4.7. Crack growth rate for debonded region 83

Figure 4.8. Debonding FE model 84

Figure 4.9 Comparison of surface strain profile obtained from DIC and FE model 86

Figure 4.10 a) Contour of interfacial damage parameter at different crack lengths; b) Comparison of debonded area obtained from DIC and FE model 87

Figure 4.11 Influence of far-field stress on the debonded area, SIF and crack growth rate 89

Figure 4.12 Influence of interface stiffness on the debonded area, SIF and crack growth rate 90

Figure 4.13 Influence of interfacial strength on the debonded area, SIF and crack growth rate 91

Figure 4.14 Influence of energy release rate on the debonded area, SIF and crack growth rate 92

Figure 5.1 Summary of numerical framework..... 95

Figure 5.2: Illustrations of: (a) long crack in single edge-notched specimen, (b) small crack 97

Figure 5.3 Crack growth curve and fatigue life 100

Figure 5.4 Calibration of EIFS value..... 101

Figure 5.5 Boundary crack length..... 102

Figure 5.6 K_{max} in small crack regime 103

Figure 5.7 Debonded region obtained from numerical and experimental results104

Figure 5.8 K_{max} in long crack regime obtained from FE model..... 105

Figure 5.9 Predicted and tested fatigue lives of all of the coupons 106

Figure 5.10 Predicted and experimental FCG curves for FRP groups 107

Figure 5.11 Predicted and experimental FCG curves for SMA/CFRP groups... 108

Figure 5.12 Influence of the number of SMA wires on the fatigue life..... 111

Figure 5.13 Influence of the number of SMA wires on the K_{max} at different crack lengths 112

Figure 5.14 Fatigue crack growth curves of coupons strengthened at different crack lengths 113

Figure A.1 SMA activation of SMA/CFRP-217-1 135

Figure B.1 SMA-CFRP-217-1 136

Figure B.2 SMA-CFRP-217-2 136

Figure B.3 SMA-CFRP-217-3 137

Figure B.4 SMA-CFRP-155-1 137

Figure B.5 SMA-CFRP-155-2 138

Figure C.1 CFRP-155-1 139

Figure C.2 CFRP-155-2 139

List of Tables

Table 2.1 Crack propagation theories used in different studies 26

Table 2.2 Values of material parameters for Paris and Erdogan equation 27

Table 3.1 Test Matrix for all of the configurations 53

Table 3.2 Fatigue lives of tested coupons 66

Table 4.1 Modelling matrix of influence on SIF at the crack tip 79

Table 4.2 Parametric study matrix 88

Table 5.1 Calculated and measured critical crack lengths 105

Table 5.2 Parametric study matrix 109

Chapter 1 : Introduction

Fatigue is a major cause of degradation of infrastructure that is subjected to cyclic loading. It is estimated that more than 80 percent of all brittle fractures are preceded by some degree of crack growth in fatigue (Sanford, 2003). Conventional repair techniques include single tensile overload to retard the crack propagation (Vardar, 1988), drilling crack stop holes to remove the crack tip (Ghfiri et al., 2000), and welding or bolting cover plate to bridge the crack (Domazet, 1996). Over the past 15 years the use of externally bonded fiber reinforced polymer (FRP) composite patches has gained research attention. Research findings indicate that the fatigue lives of fatigue sensitive elements can be increased by 2 to 3 times using externally bonded carbon FRP (CFRP) patches compared to similar un-retrofitted members (Jones and Civjan, 2003; Tavakkolizadeh and Saadamanesh, 2003). Recently, prestressed FRP patches were found to be more effective for fatigue life enhancement than non-prestressed patches (Täljsten et al., 2009; Ghafoori, et al., 2012).

However, the conventional methods of achieving an appropriate level of prestressing not only require heavy equipment, but also are designed for applying global prestressing rather than locally strengthening cracks. Consequently, there is an urgent need to identify innovative techniques to overcome this barrier of practically applying prestressing force to the FRP hence effectively delay or prevent the formation of new cracks or propagation of existing cracks.

1.1 Research objectives

In this research, shape memory alloy (SMA) materials are embedded into FRP matrix to provide prestressing forces when thermally activated. By doing so, this SMA/FRP composite can achieve prestressing forces without the need of specialized equipment. The central hypothesis of this research is that the fatigue life of crack-sensitive steel elements can be significantly extended using this newly developed SMA/FRP patch. Therefore, the objectives of this research are to: 1) Test the central hypothesis by quantifying the fatigue life enhancement that can be achieved using the SMA/FRP composite patches to repair steel members, 2) Understand the working and failure mechanisms of the system,3) Establish a numerical framework to predict the fatigue performance of the retrofitted element, 4) Quantify the influence of different parameters of the patching system on the fatigue life enhancement that can be achieved for fatigue-sensitive steel elements.

1.2 Outline of the dissertation

This dissertation consists of six chapters including this introduction chapter. Chapter 2 presents a literature review of relevant previous research. Firstly, it summarizes the experimental work including using non-prestressed and prestressed FRP to fatigue strengthen both small and large scale specimens. Secondly, it reviews the advancement in numerical simulation of the fatigue crack propagation of FRP-patched metallic structures. Finally, it reviews the research work regarding SMA characteristics and applications.

Chapter 3 presents the details of the experimental program that was implemented to test twenty-seven single edge-notched steel plates with four types of patching configurations. The results helped to quantify the fatigue life enhancement that can be

achieved using the newly developed SMA/FRP patching system. In addition, the bond behavior between the reinforcing patch and the steel substrate under fatigue loading was investigated using a digital image correlation (DIC) system.

Chapter 4 discusses the numerical investigation of the interfacial debonding during fatigue loading. A finite element (FE) model was developed to predict the shape and size of the debonded region. The model was validated by the experimental DIC data. A parametric study using the model was conducted to study the influence of the applied load and interfacial properties on the interfacial debonding.

Chapter 5 describes the established numerical framework to predict the fatigue life and perform the fatigue crack growth (FCG) analysis of steel plates reinforced with the SMA/FRP composite patch. The FE model introduced in Chapter 4 was incorporated in the framework to accurately predict the interfacial debonding (without *a priori* knowledge of the shape of the debonded region) and hence incorporate its effects on the FCG analysis. Second, the crack initiation and the small crack propagation stages were taken into account in this study using an equivalent initial flaw size (EIFS) method. A parametric study was also conducted to better understand the influence of various parameters on the effectiveness of the developed SMA/FRP patching system.

Chapter 6 summarizes the conclusions of this research and limitations of the new application, followed by recommendations for future research directions.

Chapter 2 : Literature review

This chapter reviews the previous experimental and numerical research work related to FRP strengthening of metallic structures, and characteristics of SMA materials, and applications of SMA materials for civil infrastructure. The experimental evidence supporting the use of un-prestressed and prestressed FRP to improve the fatigue performance of fatigue damaged or fatigue sensitive large- and small- scale steel members was reviewed. Independent observations of interfacial debonding between FRP and metal substrates during fatigue loading were introduced. Further, the analytical and FE models that were proposed to evaluate the stress intensity factor (SIF) of steel plates and beams with different strengthening configurations were discussed. The fatigue propagation equations adopted in the previous research work were discussed including their limitations and advantages. The development of the methods for simulating small crack propagation in FCG analysis was reviewed. Finally, research findings regarding the characteristics and applications of SMA materials were reviewed.

2.1 Fatigue strengthening of metallic structures using FRP

Externally bonded FRP composites have been used to rehabilitate fatigue damaged or fatigue sensitive metallic structures in marine (Allan et al., 1988; Grabovac, 2003; McGeorge et al., 2009) and aerospace (Baker, 1984; Umamaheswar and Singh, 1999; Marioli-Riga et al., 2001; Fujimoto and Sekine, 2007) applications. Jones and Civjan (2003) tested 29 steel specimens including 8 center-hole specimens and 21 edge-notched specimens. Three configurations of CFRP systems were adhesively bonded to the cracked steel plates to assess the increase of the fatigue lives that could be achieved.

The parameters studied were the type of CFRP, bond length, bond area, one- and two-sided reinforcement, and prior to- or subsequent to- crack propagation reinforcement. The CFRP overlays more than doubled the fatigue lives of the tested elements with the most significant increases being achieved for double-sided reinforcements, fully bonded CFRP overlays and wire brushed surface preparation. Finite element (FE) models of the tested specimens were developed to analyze the stress concentration at the crack starter. The calculated stress value was used to predict the total fatigue life of the specimen using the material's stress-life (S-N) curves. However, the fatigue life prediction using this method was non-precise and inaccurate. For example, the predicted fatigue lives of a bare coupon and a CFRP-patched coupon were from 90,000 cycles to theoretically infinite life and from 250,000 cycles to infinite life, respectively. The experimentally measured fatigue lives of the bare coupons and CFRP-patched coupons averaged in 173,000 and 358,000 cycles, respectively.

Tavakkolizadeh and Saadamanesh (2003) retrofitted 21 notched steel beams with unstressed 300 mm × 76 mm × 1.27 mm unidirectional pultruded CFRP patches with average tensile strength of 2,137 MPa and modulus of 144 GPa. The beams were subjected to four-point bending fatigue loading. Results showed that the fatigue life of a detail can be extended by 2.6 to 3.4 times using adhesively bonded unstressed CFRP laminates.

Liu *et al.* (2009) investigated the fatigue crack growth behavior of steel plates reinforced with CFRP. The parameters studied using eleven two-side and ten one-side CFRP-reinforced specimens were the type of CFRP, patch thickness, bond length, and bond width. Results showed that normal modulus (NM) and high modulus (HM) CFRP

reinforcements reduced crack growth rates and prolonged fatigue lives by 2.2-2.7 times and 4.7-7.9 times respectively. Increasing the bonded width increased the fatigue life by up to 70% while changing the other parameters increased the average fatigue lives by over 20% for both single-sided and double-sided repairs.

Kim and Harries (2011) investigated the fatigue behavior of notched steel beams repaired with 50 mm wide by 1.4 mm thick CFRP strips with a tensile strength of 2800 MPa and modulus of 155 GPa. The epoxy used to bond the CFRP strips had a tensile strength of 25 MPa and a modulus of 4.5 GPa. A total of six damaged steel beams, of which four were repaired with CFRP strips bonded on the bottom flange, were tested under monotonic or fatigue loading up to failure. A three-dimensional (3-D) nonlinear FE model was developed to analyze the stress values of the tested beams. The fatigue lives of the tested beams were predicted using a strain-life (ε-N) method. The predicted fatigue lives of beams tested at stress ranges of 0.73, 0.42 and 0.21 times of the yielding stress were 15,000, 150,000 and 2,100,000, respectively. The measured fatigue lives at those stress ranges were 20,000, 152,380 and 1,703,020, respectively.

Yu *et al.* (2013) investigated the effect of CFRP reinforcement on steel plates with different degrees of fatigue damage prior to the retrofit. Three of six 500 mm × 100 mm × 8 mm central-hole coupons with different initial crack lengths were strengthened with 200 mm × 40 mm × 1.4 mm CFRP overlays with tensile strength of 3000 MPa and modulus of 190 GPa and tested under tension-tension fatigue loading. Results showed that the CFRP reinforcement extended the average fatigue lives of the cracked steel plates by 97 to 186%.

The effectiveness of prestressing the CFRP patches prior to the installation has also been studied. Täljsten *et al.* (2009) tested 670 mm × 205 mm × 8 mm central hole steel plates bonded with two 400 mm × 50 mm × 1.4 mm CFRP plates. The considered parameters were high (260 GPa) and low (155 MPa) modulus CFRP plates, different types of adhesives (shear strength of 81 MPa and 52.5 MPa), and prestressed and un-prestressed CFRP. The prestressing of the CFRP plates was conducted using a construction rig consisting of two anchor-blocks, one flexible joint, two threaded rods and bolts at each end, two friction joints each having six bolts, a force measurer, and a mounting bed on which every other part was mounted. The CFRP plate was clamped to the friction joint with each bolt tightened to a force of 20 kN. Subsequently, the prestress force was applied by turning the bolts on the threaded rods and monitoring by the force measurer. Prestressing forces of 12 and 15 kN, equivalent to 170 and 214 MPa prestress in the CFRP plate, were considered. Results indicated that installation of non-prestressed laminates increased the fatigue lives of the elements by nearly four times while the crack growth was completely arrested using prestressed laminates. The compressive stress induced in the steel due to the prestressing of the CFRP plates was 7.3 MPa.

Huawen *et al.* (2010) conducted 14 fatigue tests of double-edge notched steel plates that were strengthened with prestressed CFRP laminates. The influence of the applied stress range, CFRP stiffness, and prestressing level on the crack growth was investigated. The specimens reinforced with CFRP with prestress levels of 600, 1000 and 1200 MPa and tested at 100 MPa stress range respectively exhibited 0.7, 1.7 and 3.4 times the average fatigue life of similar un-reinforced specimens that were tested at 80 MPa stress range. Figure 2.1 summarizes the test data of the above mentioned studies of

using prestressed or un-prestressed externally bonded FRP to improve fatigue performance of steel members. The figure can only show a general trend since the strengthening methods of different studies are not directly comparable. It is seen that, using same stiffness of FRP, the prestressed FRP is much more effective in improving fatigue life than un-prestressed FRP.

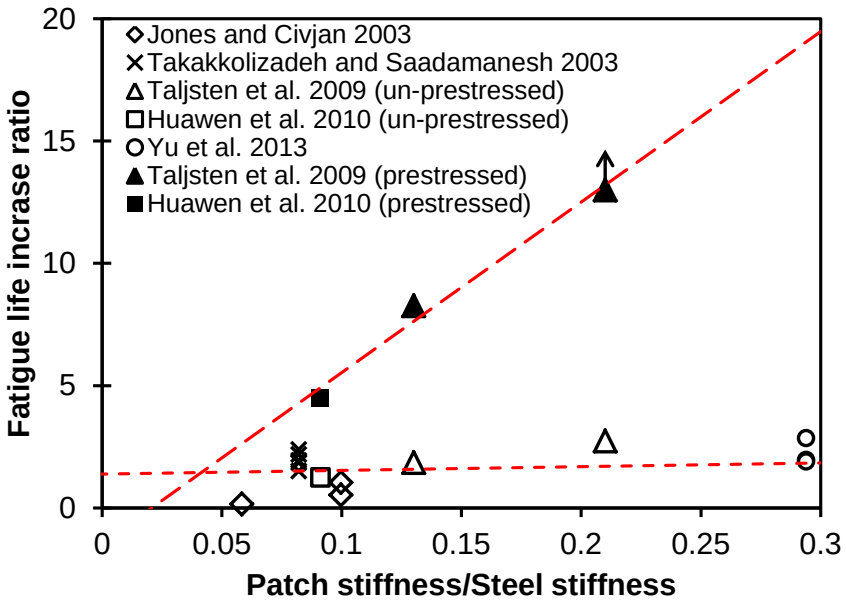

Figure 2.1 Fatigue life improvement using un-prestressed and prestressed FRP

The current technique for prestressing externally bonded FRP plates to steel members requires hydraulic jacks or heavy fixtures to apply the prestress and anchor the FRP (Täljsten *et al.* 2009). This strengthening method is practical for rehabilitation of individual members in a laboratory environment. However, its application may be limited in field installations. Therefore there is an urgent need to identify an innovative method to overcome this technical barrier. Researchers have developed prestressed un-bonded reinforcements which use friction clamps and seating chairs to anchor the CFRP plate to the structure (Ghafoori *et al.*, 2015). However, research found that bonded

reinforcements are more effective than un-bonded reinforcements. Ghafoori *et al.* (2012) investigated the fatigue strengthening of damaged metallic beams using bonded and un-bonded prestressed CFRP plates. In the study, identical beams were strengthened with prestressed CFRP at the same prestress level. The beam with bonded CFRP reinforcement exhibited 70 times the fatigue life of similar beam with un-bonded CFRP reinforcement.

2.2 FRP-metal interface debonding under fatigue loading

FRP patches improve the fatigue behavior and extend the fatigue life of steel members by decreasing the stress range in the steel at the patched segment. The applied load is partially transferred to the externally bonded FRP patches from the steel substrate through the bonded interfaces. The reduced stress range in the steel depends on the relative stiffness of the FRP patch compared to the steel element. The FRP also bridges the crack and reduces the crack opening displacement. Both of these mechanisms rely on the integrity of the bond at the interface. However, debonding has been observed to occur at the FRP/steel interface near the crack during fatigue loading (Colombi, 2003; Sabelkin et al., 2006; Huawen et al., 2010).

Colombi et al. (2003) conducted fatigue testing on CFRP-strengthened central-hole steel coupons. Steel plates with a central hole and two initial cracks were reinforced using two CFRP strips on each side. The coupons were loaded under a constant amplitude cyclic load with far-field stress range of 80 MPa and stress ratio of 0.4. The surface of the CFRP was monitored using optical speckle interferometry during the fatigue loading to record the displacement fields at different stages. It was observed that a debonded region at the adhesive/steel interface was generated as the crack propagated

into the boundary of the bonded CFRP strip. Figure 2.2 illustrates the assumed debonded region at the adhesive/steel interface during fatigue loading by comparing the experimentally recorded and numerically obtained displacement fields. The debonded region was assumed to follow a semi-elliptical shape with an aspect ratio of 1:5. The major axis lies on the crack path and the minor axis lies on the edge of the CFRP strip near the crack mouth. The vertex of the debonded region is ahead of the crack tip by a distance equal to the plastic zone size.

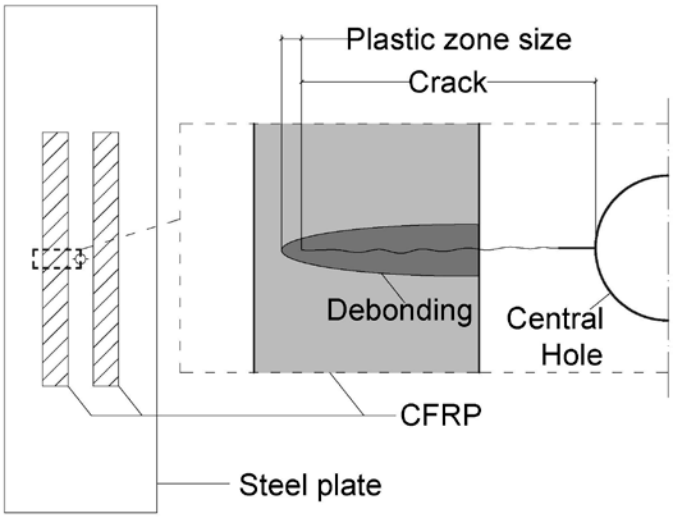

Figure 2.2 Crack growth induced debonding (Colombi et al. 2003)

Sabelkin et al. (2006) studied fatigue crack growth of pre-cracked center-notched aluminum panels repaired with one-side bonded composite patches. 2024-T3 aluminum alloy sheets with thicknesses of 1 mm were prepared with a 12.7 mm long × 3 mm wide center-notch. Three layers of Boron/epoxy composite patch were used to strengthen the aluminum alloy sheets with a thin film of adhesive. Two 1.6 mm thick × 25.4 mm wide × 389 mm long patches were bonded on one side of the specimen oriented along the loading direction. The coupons were fatigue loaded with a stress range of 114 MPa, stress ratio of 0.05, and frequency of 8 Hz. Debonding at the composite/aluminum interface was

only observed along the crack. Figure 2.3 schematically illustrates the observed debonded region after the test. It had the shape of a very slender ellipse with the major axis length equal to the instantaneous crack length and a minor axis length of approximately 2 mm.

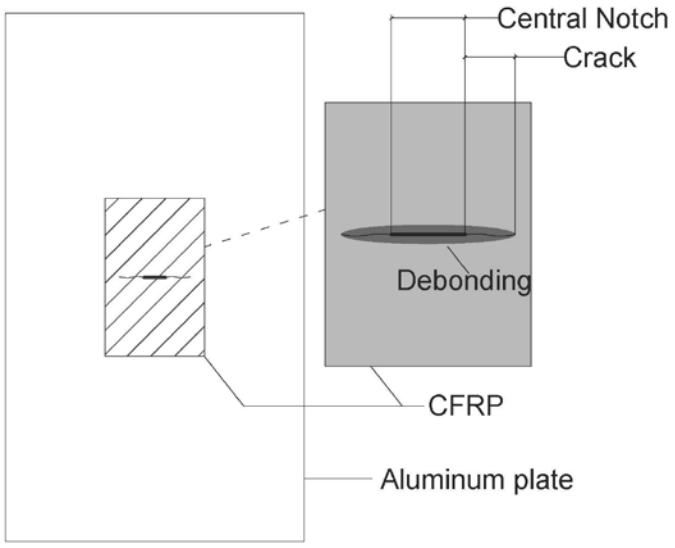

Figure 2.3 Observed shape of interfacial debonding (Sabelkin et al. 2006)

Huawen et al. (2010) conducted fatigue testing of double edge-notched steel plates that were strengthened with prestressed CFRP laminates and reported a different shape of debonding. Figure 2.4 shows the schematic drawing of the observation. Double edge-notched steel plates were patched with CFRP strips on both sides as shown in the figure. The debonded regions were examined after the failure of the specimen and exhibited approximately trapezoidal shapes. Since the observation was made after the rupture of the specimen, the shape of the final debonded region is likely the cumulative trace of the instantaneous debonded region. By comparing the final debonded regions among all of the tested specimens, it was found that specimens bonded with CFRP laminates with higher prestressing levels exhibited smaller debonded regions. For example, the debonded areas were 1225, 762 and 365 mm^2 corresponding to CFRP laminate prestressing levels of 600, 1000 and 1200 MPa.

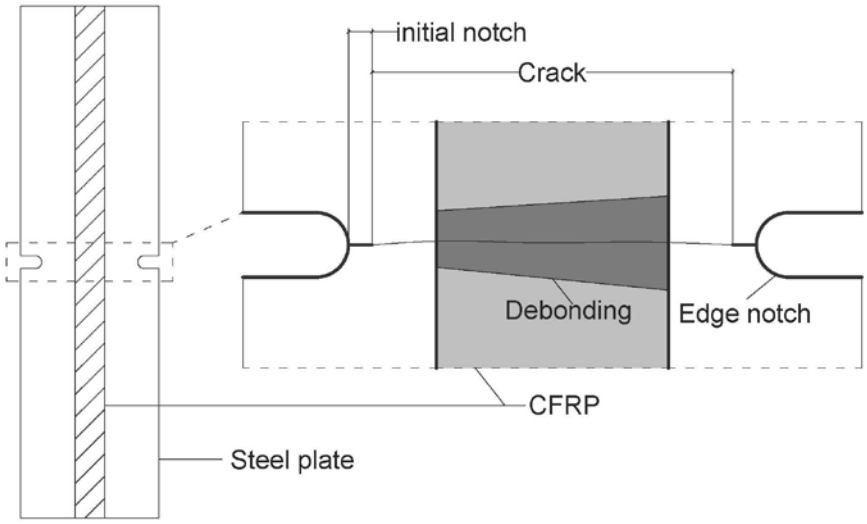

Figure 2.4 Trapezoidal debonded region (Huawen et al. 2010)

Wu et al. (2013b) directly investigated the effect of fatigue loading on the bond behavior between CFRP and steel through seventeen double-lap joint specimens under both monotonic and fatigue loading. Five specimens were tested monotonically up to failure as control specimens. The other twelve specimens were first fatigue loaded with load ratios ranging from 0.2 to 0.6 for certain cycles, the survived ones were subsequently tensioned up to failure. All of the specimens exhibited CFRP-Steel debonding failure. Visual inspection of the debonded interfaces of the control specimens and fatigue loaded specimens indicated no difference. By comparing the residual bond strength and residual stiffness of the control specimens and fatigue loaded specimens, it was found that the fatigue loading had very limited impact on the bond between CFRP and steel. For example, the ratio of the residual strength of the specimens that survived fatigue loading and the strength of the control specimens ranged from 95% to 114%. Accordingly, the concept of the fatigue damage zone, a localized region of debonding between the CFRP and steel due to the influence of fatigue loading, was proposed. Figure 2.5 shows the schematic illustration of the fatigue damage zone (adapted from Wu et al.,

2013). Microscopic examination of the debonded interface indicated that the ratio of the length of the fatigue damage zone and the entire bond length ranged from 0.60% to 3.20%. For example, a specimen survived 10,000,000 fatigue cycles exhibited a fatigue damage zone that was 0.72% of the entire bond-line. This finding illustrated the difference between static-load induced debonding and fatigue-load induced debonding, and suggested that the fatigue-load induced debonding is minimal compared to the static-load induced debonding. It was conclude that the effect of the fatigue loading is constrained within a limited bond area, and the static bond behavior will not be affected even if the specimen experienced considerable fatigue loading.

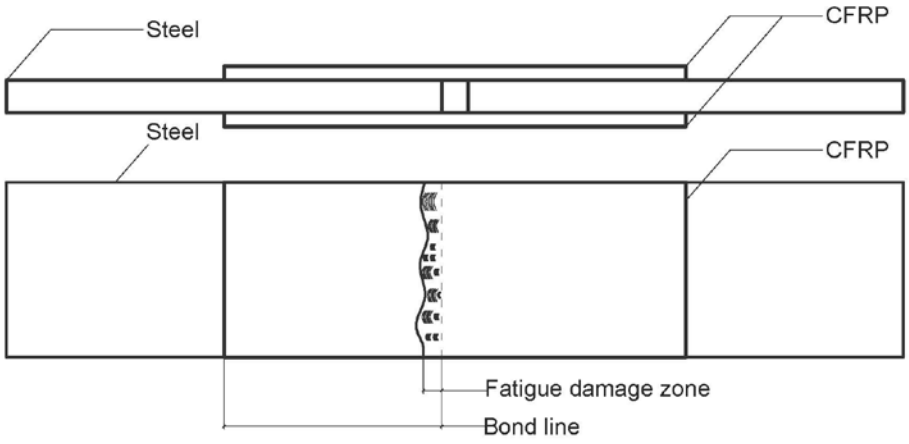

Figure 2.5 Illustration of fatigue damage zone (adapted from Wu et al., 2010)

It was reported independently that the debonding has a non-trivial impact on the predicted crack growth rate. Sabelkin et al. (2006) compared the results of considering or not the debonded region on the predicted SIF values. By incorporating an elliptical debonded region with the major axis length equal to the crack length and minor axis length equal to 2 mm, the calculated SIF values increased by 5% to 10% compared to not incorporating debonding. The increase is slight because the debonded region was assumed as 2 mm along the crack in the study. It should be noted that the SIF has an

approximate cubical influence on the crack growth rate, which further has considerable impact on the predicted fatigue life due to the integration. Wang et al. (2013) studied the FRP strengthening effects on fatigue repair of cracked steel plates experimentally and numerically. In the developed numerical model, the debonded region was assumed as elliptical shape with aspect ratios of 0 (no debonding), 0.15 and 0.25 in order to understand the influence of the assumed debonded region on the fatigue life prediction. The corresponding predicted fatigue lives were 1.45, 1.3 and 1.25 times of a reference number, respectively. This implies that inappropriate assumption of the debonded region could result in inaccurate predictions of the fatigue life. Taken collectively, it is evident that the near-crack debonding was observed for all FRP-patched metallic members; and it has considerable impact on the prediction of the crack growth rate hence the fatigue life. It is suggested that this type of debonding to be incorporated in the numerical models of FRP-metal system. However, more experimental observations and numerical simulations are required for further understanding and validation.

2.3 Estimation of SIF for FRP-patched elements

Most of the previously reported works adopted the linear elastic fracture mechanics (LEFM)-based approach to perform fatigue analyses of FRP-metal system. LEFM has been used to analyze fatigue crack propagation in metallic materials since the 1960s (Irwin, 1957; Paris et al., 1961; Paris and Erdogan, 1963; Rice, 1967). The LEFM-based method consists of two steps: i) calculate the SIF values at the crack tip at different stages during the crack propagation, and ii) estimate the crack growth rates at those stages based on the calculated SIF values using an appropriate crack propagation model. Regarding the FRP-metal system, however, the existing models need to be modified in

order to account for the bridging effects of the FRP. Analytical models need to consider the influence of FRP on the SIF values, while FE models need to incorporate the externally bonded FRP. The bond behavior at FRP-metal interface during fatigue crack propagation was identified as the key element in fatigue life prediction of FRP-strengthened steel structures (Teng et al., 2012).

2.3.1 Analytical models

Liu et al. (2009) studied the fatigue behavior of central-hole steel plate bonded with multiple layers of non-prestressed CFRP sheets. By considering the effect of non-uniform strain levels among multiple layers of CFRP sheets and assuming perfect bond at the adhesive/steel interface, the equivalent modulus of the multilayer composite was expressed as follows:

$$E_C = \frac{E_f t_f + E_a t_a}{n(t_f + t_a)} \sum_{i=1}^{n} k_i \,, \tag{2.1}$$

where E and t denote the Young's modulus and thickness; subscript C, f and a denote composites, carbon fiber, and adhesive, respectively; n is the number of sheet layers; k_i is the ratio between the strain in the i^{th} sheet layer and the strain in the steel plate.

The average stresses at the nominal cross-section of the steel plate, σ_S, for double-sided repair and single-sided repair were expressed as Eq. (2.2) and (2.3), respectively:

$$\sigma_S = \frac{E_S t_S}{E_S t_S + 2E_C (b_C/(b-2a)) t_C} \sigma_0 \text{ and} \tag{2.2}$$

$$\sigma_S = \frac{E_S t_S}{E_S t_S + E_C (b_C/(b-2a)) t_C} \sigma_0 \,, \tag{2.3}$$

where σ_0 is the applied stress, b is the width of steel plate, a is half of the crack length, subscript s denotes steel plate. Subsequently, the mode I SIF, K_I, in the steel was calculated as

$$K_I = \sqrt{\sec(\frac{\pi a}{b})} \cdot \sigma_S \cdot \sqrt{\pi a} \,. \tag{2.4}$$

Similar approach of calculating the SIF for composite patched steel plate was adopted by Yu et al. (2013) in the study of fatigue behavior of CFRP strengthened steel plates with different initial damage degree, β. Feng et al. (2014) investigated the thermal effects on fatigue behavior of CFRP strengthened steel plate. Eq.(2.2) was modified by considering the temperature effect as

$$\sigma_S = \frac{E_S t_S}{E_S t_S + 2\beta_t E_C (b_C/(b-2a)) t_C} \sigma_0 , \tag{2.5}$$

where β_t was used to reflect the thermal influence on the equivalent modulus of composite patch. The value of β_t ranged from 0.13 to 2.4 with temperature, T, changing from -20 to 60^{o}C as

$$\beta_t = 10^{-6}(4.11T^3 + 253.86T^2 + 6642.98T + 197826.6) , \tag{2.6}$$

Taljsten et al. (2009) studied the strengthening of steel plate using prestressed CFRP laminates. Central-hole specimen was reinforced with adhesively bonded prestressed CFRP laminates as shown in Figure 2.6. An approach of superposition of three mode I SIF components was adopted to estimate the resulting SIF value. Figure 2.6 illustrates the three SIF components: i) a bare steel plate with two symmetrical cracks that is loaded at two ends, $K_I^{(1)}$:

$$\Delta K_I^{(1)} = \Delta\sigma_{eff}\sqrt{\pi a}\left(0.5\left(3-\frac{a}{r+a}\right)\left[1+1.243\left(1-\frac{a}{r+a}\right)^3\right]\right), \tag{2.7}$$

where $\Delta K_I^{(1)}$ is the first component of SIF value, $\Delta\sigma_{eff}$ is the effective stress range, a is half of the crack length, r is the radius of the central-hole.

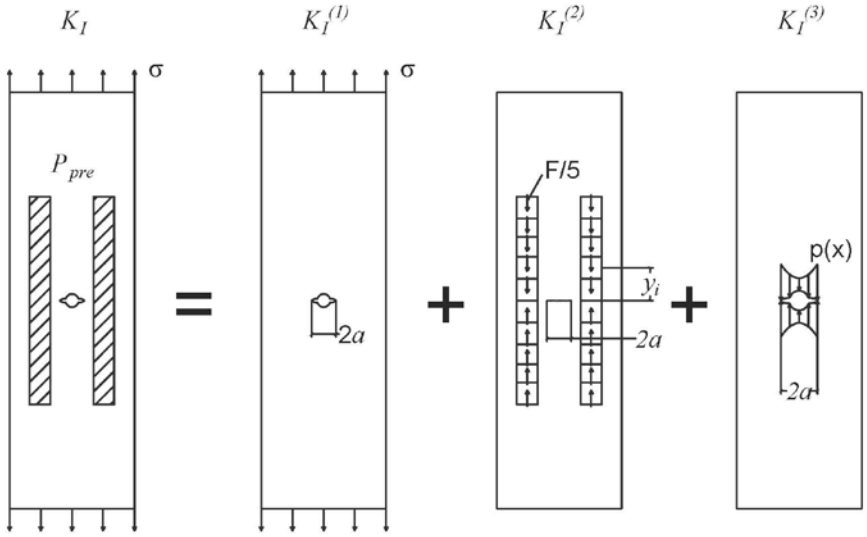

Figure 2.6 Central-hole steel coupon reinforced with prestressed CFRP strips

ii) a steel plate with closed crack in the center loaded with the reaction force from all bonded laminates, $K_I^{(2)}$, which is equal to zero since the crack is fully closed. and iii) a steel plate with two symmetrical cracks loaded with distribution *p(x)* as indicatedin the figure:

$$\Delta K_I^{(3)} = \sum_{i=1}^{5} \frac{-2\sqrt{\pi a}}{\sqrt{\pi}} \int_{x=0}^{x=a} \frac{p(x)}{\sqrt{a^2 - x^2}} dx, \tag{2.8}$$

where $\Delta K_I^{(3)}$ is the third component of SIF value, *p(x)* is calculated from the load distribution of the CFRP laminate in the second component. The SIF range for crack growth analysis is the sum of the three components:

$$\Delta K_I = \Delta K_I^{(1)} + \Delta K_I^{(2)} + \Delta K_I^{(3)}. \tag{2.9}$$

This model fits the applications of using prestressed FRP composite to strengthen metallic plate elements. Ghafoori et al. (2012) investigated the fatigue behavior of

cracked steel beam reinforced with bonded and un-bonded prestressed CFRP laminate. Figure 2.7 illustrates the strengthening approach.

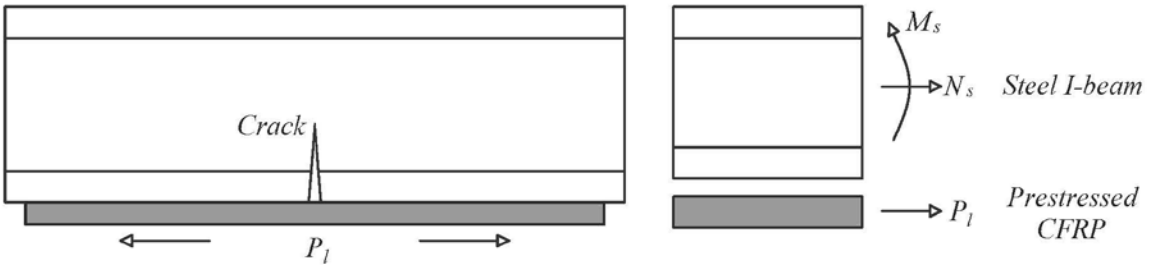

Figure 2.7 Cracked steel I-beam reinforced with prestressed CFRP patch on the bottom flange

An analytical model for calculating the SIF for un-strengthened cracked steel I-beam was introduced by Ghafoori and Motavalli (2011) based on the crack surface widening energy release rate as

$$K_I = \left[\left(-\frac{N^2}{A} - \frac{(M_C - Y_C \cdot N)^2}{I} + N^2(\lambda_1 + \lambda_2) + M_C^2(\eta_1 + \eta_2)\right)\frac{\pi}{t_w(1-\nu^2)}\right]^{\frac{1}{2}}, \qquad (2.10)$$

where N and M are the axial force and bending moment applied to the beam, subscript 'c' and 'uc' denote the cracked and un-cracked sections respectively; Y_C is the difference between the position of neutral axes in the un-cracked and cracked cross-section; A and I are the area and moment of inertia of the un-cracked section of the beam; ν is the Poisson's ratio; t_w is the thickness of the web; λ_1, λ_2, η_1 and η_2 are functions of the beam geometry and crack length that can be found in details in (Ghafoori and Motavalli, 2011). Using Eq. (2.10) and the principle of superposition, the SIF for cracked steel I-beam strengthened with prestressed CFRP is given as a function of crack length, a, external bending moment, M and the tensile force in the CFRP, p_l as

$$K_I^{Overall}(a,M,p_l)=\left(M-p_l\left(t_f+\frac{h}{2}\right)\right)\left[\left(-\frac{1}{I}+(\eta_1+\eta_2)\frac{\pi}{t_w(1-\nu^2)}\right)\right]^{\frac{1}{2}}, \qquad (2.11)$$
$$-p_l\left[\left(-\frac{1}{A}+(\lambda_1+\lambda_2)+Y_C^2(\eta_1+\eta_2)\frac{\pi}{t_w(1-\nu^2)}\right)\right]^{\frac{1}{2}}$$

where t_f is the thickness of the flange, h is the height of web. At a given bending moment, Eq. (2.11) can predict the level of force needed in the CFRP to close the crack in the steel beam. This model could be used to the fatigue analysis of cracked I-beam reinforced with prestressed or non-prestressed FRP on the bottom flange.

2.3.2 FE models

Finite element method was adopted in other studies to calculate the SIF of FRP reinforced metallic members. Colombi et al. (2003) investigated fatigue behavior of steel members reinforced by prestressed composite patches. A two-dimensional (2-D) FE model using the three-layer technique was developed to evaluate the SIF. The model consists of three layers simulating the composite patch, adhesive layer and the steel substrate, respectively, using Mindlin assumptions. Figure 2.8 (adapted from Colombi et al., 2003) illustrates the three-layer technique. The Mindlin theory assumes linear displacement field in the plate thickness. In the bonded region, the displacement at the interface was constrained. The constraint was released in the debonded region. The strain energy release rate, G, at the vicinity of the crack tip was calculated using the standard virtual crack extension method and assuming plane stress conditions. The SIF for mode I opening was expressed as

$$K_I=\sqrt{G\cdot E}, \qquad (2.12)$$

where *E* is the elastic modulus of steel. The three-layer technique was also adopted by Lam et al. (2010) in the study of SIF for cracked steel plate with single-sided CFRP patching.

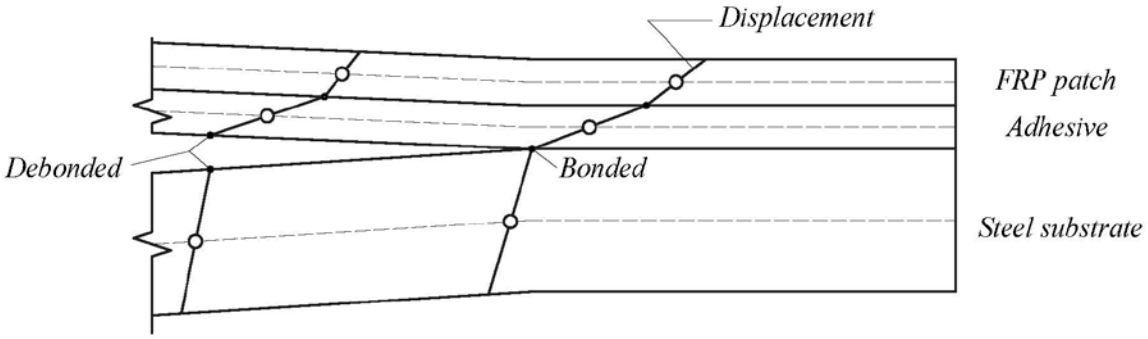

Figure 2.8 FE model using three-layer technique (Colombi et al. 2003)

Lee and Lee (2005) developed a 3-D FE model to analyze the crack propagation in an aluminum plate that was reinforced on one side by a FRP patch. The un-cracked part was meshed with isotropic quadrilateral 20-node brick elements in a relatively coarse manner, while the crack tip was meshed with collapsed wedge elements with the mid-node shifted to the quarter position. Figure 2.9 shows the typical mesh of the crack tip using the collapsed wedge elements.

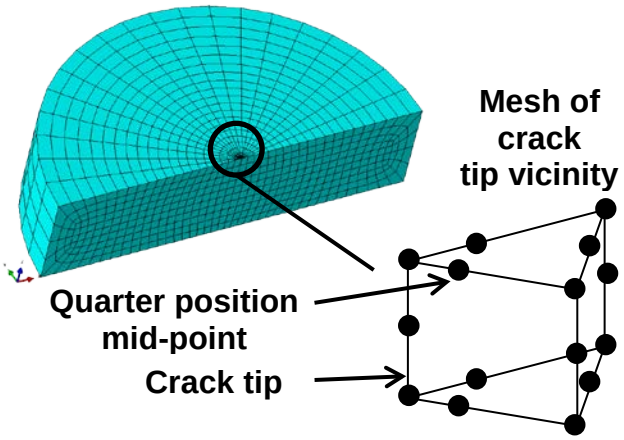

Figure 2.9 Typical mesh of the crack tip using collapsed 20-node wedge elements

The *J*-integral values at the nodes on the crack tip were calculated; hence the mode I SIF was evaluated using the following equation:

$$K_I^2 = J \cdot E', \tag{2.13}$$

where *E'* is the modified modulus that is equal to $E/(1-\nu^2)$ for plane strain and *E* for plane stress, where ν is Poisson's ratio and *E* is the Young's modulus. A successive technique was employed to perform the fatigue analysis. After calculating the SIFs of the nodes on the crack tip at the current location, the local crack growth rates were calculated. The crack growth rate was assumed to remain constant for a given number of cycles and the crack front was propagated accordingly. Since the member was bonded on one side, the propagation rate of the crack at the bonded side was much lower than that at the un-bonded side, which resulted in a skewed crack front. Figure 2.10 illustrates the predicted crack front trace using this method.

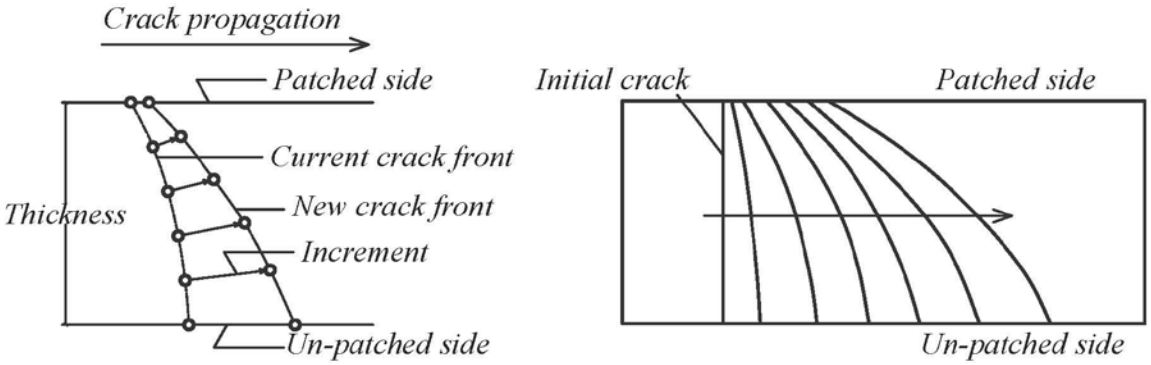

Figure 2.10 Skewed curve crack front along thickness of single-side repair (Lee and Lee, 2005)

Tsouvalis et al. (2009) investigated fatigue behavior of steel plate with single side bonded CFRP. A 3-D FE model with crack tip modeled by collapsed 20-noded wedge elements were developed to calculate the SIF at the crack tip. The predicted SIF values along the thickness were consistent with the findings in Lee and Lee (2005). The SIF

values at the un-patched side were 40, 56 and 80 MPa $m^{1/2}$ for crack lengths of 40, 60 and 80 mm respectively. While the values were approximate 12 MPa $m^{1/2}$ for crack lengths of 40, 60 and 80 mm on the patched side. Therefore, it is recommended that for single side repair of cracked metallic members using FRP patches, the non-uniform propagation of the fatigue crack front should be considered. For double side repairs, a uniform SIF distribution along the thickness, or straight crack front line, provides a reasonable estimate (Wu et al. 2012; Wang et al. 2013). In Ghafoori et al. (2012) and Hmidan et al. (2014), 3-D FE models were developed to simulate cracked steel beam reinforced with CFRP plate on the bottom flange. Uniform SIF distribution along the thickness was assumed.

Yu et al. (2014, 2015, 2016) and Chen et al. (2013, 2014) predicted the crack propagation of CFRP reinforced steel plates using the boundary element (BE) method. One advantage of using the BE method is the lower computational cost due to that only the surfaces of the model are modeled and meshed. The other advantage is attributed to the discontinuous element representing the strain discontinuity at the crack tip. In the BE model, the SIF value for each crack length was obtained using J-integral approach. The steel plate and the CFRP laminates were modeled using quadrilateral shaped, reduced quadratic order elements. The adhesive layer between the CFRP and steel was modeled using continuously distributed linear springs. The normal and shear stiffness values of the springs were determined from the elastic properties of the adhesive epoxy as

$$K_n = \frac{E_a}{t_a}, K_t = K_u = \frac{G_a}{t_a}, G_a = \frac{E_a}{2(1+\nu)}, \tag{2.14}$$

where K_n is the normal stiffness, K_t and K_u are the shear stiffness's, E_a and G_a are the Young's modulus and shear modulus, respectively. t_a is the measured thickness of the adhesive layer and ν is the Poisson's ratio of the adhesive.

2.4 Fatigue crack propagation model

Once the SIF values at different stages during the fatigue loading were calculated, fatigue crack propagation theory is used to predict the crack growth rates at those different crack lengths. The most widely adopted long crack propagation theory was proposed by Paris and Erdogan (1963). The empirical power law relationship between the crack growth rate, *da/dN*, and the stress intensity factor range, ΔK, is expressed as

$$\begin{aligned} \frac{da}{dN} &= C(\Delta K)^m \\ \Delta K &= K_{\max} - K_{\min} \end{aligned}, \tag{2.15}$$

where C and m are material-dependent parameters, K_{max} and K_{min} are the maximum and minimum SIF values corresponding to the maximum and minimum applied stresses, σ_{max} and σ_{min}, respectively. Elber (1970) studied the load-displacement behavior of a fatigue cracked steel plate and found that the crack tip was not fully open until the applied tension load reached the crack opening load, F_{op}. This is recognized as the crack closure effect. The effective stress range, $\Delta\sigma_{eff}$, was defined as

$$\Delta\sigma_{eff} = \sigma_{\max} - \sigma_{op}, \tag{2.16}$$

where σ_{op} is the stress at which the crack tip becomes fully open. Further, Elber (1971) modified the Paris and Erdogan relationship by replacing the stress intensity factor range, ΔK, with the effective stress intensity factor range, ΔK_{eff}, as

$$\frac{da}{dN} = C(\Delta K_{eff})^m$$
$$\Delta K_{eff} = K_{\max} - K_{op}, \quad (2.17)$$
$$U = \Delta K_{eff} / \Delta K$$

where K_{op} is the SIF value under σ_{op}, U is the ratio of ΔK to ΔK_{eff}. In the following decades, the Elber's equation was widely adopted for fatigue crack propagation analysis in metallic structures and the evaluation of U was extensively investigated. Kumar (1992) conducted a systematic study of the stress intensity range ratio, U, using over 50 independent research studies. The majority concluded that U was dependent on stress ratio, R, only, i.e., $U = U(R)$. Figure 2.11 shows four examples of U-R relationship obtained experimentally for aluminum alloy, titanium alloy and steel with yielding stresses of 435 and 379 MPa. It should be noted that inappropriate selection of the U-R relationship is likely to result in prediction errors. For example, using the U-R relationship obtained from aluminum alloy on the fatigue crack propagation analysis in steel material is cautioned.

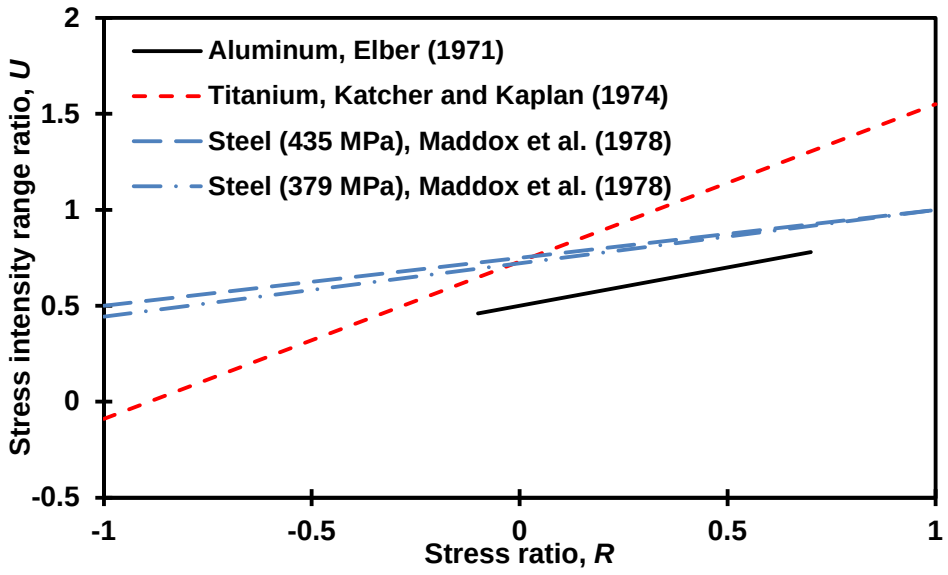

Figure 2.11 U-R relationships for different materials

A similar model was developed through a continuum fatigue model by Lal and Weiss (1978). The model was modified by Zheng and Hirt (1983) as

$$\frac{da}{dN} = B(\Delta K_{eff})^2 \quad , \qquad \Delta K_{eff} = \Delta K - \Delta K_{th} \tag{2.18}$$

where B is a material constant that can be predicted from the tensile fracture strength, σ_f, and fracture strain, ε_f, as

$$B = \frac{1}{2\pi E \sigma_f \varepsilon_f}. \tag{2.19}$$

The effective stress intensity factor range, ΔK_{eff}, in Eq. (2.18) is conceptually and physically different with that was proposed by Elber in Eq. (2.17). ΔK_{eff} in Eq. (2.18) is defined as the difference between the SIF range, ΔK, and the crack propagation threshold, ΔK_{th}, whereas it is the different between the maximum SIF, K_{max}, and the crack opening SIF, K_{op}, in Elber's equation.

Table 2.1 lists which previous studies adopted each of the predominant crack propagation laws. Some studies adopted the Paris and Erdogan equation because the stress ratio, R, was constant for all the tested specimens. For example in Lee and Lee (2005), fatigue tests were conducted to investigate the fatigue behavior of pre-cracked aluminum plates patched with FRP composite patches. All of the un-patched and FRP-patched aluminum coupons were tested at a stress ratio of 0.1. The FRP overlay reduced the stress range in the aluminum while the stress ratio remained unchanged. Therefore, the Paris-Erdogan equation fits the fatigue crack analysis and fatigue life prediction in the study. The two material parameters, C and m, were experimentally calibrated by a curve fit to the log-log plot of da/dN vs. ΔK data. The difference between the predicted and

measured average fatigue lives for all of the tested coupons ranged from 3% to 7%. In some studies, the Paris-Erdogan equation was further modified by involving the crack propagation threshold, ΔK_{th} (Liu and Zhao, 2013; Feng et al., 2014) as

$$\frac{da}{dN} = C(\Delta K^m - \Delta K_{th}^m) \cdot \tag{2.20}$$

Neither advantages nor disadvantages were reported by using this equation.

Table 2.1 Crack propagation theories used in different studies

Crack propagation model	References	Equations
Paris and Erdogan	Lee and Lee (2005); Sabelkin et al. (2006); Tsouvalis et al. (2009); Wu et al. (2012); Yu et al. (2013)	$\frac{da}{dN} = C(\Delta K)^m$
	Liu and Zhao (2013); Feng et al. (2014)	$\frac{da}{dN} = C(\Delta K^m - \Delta K_{th}^m)$
Elber	Huawen et al. (2010); Wang et al. (2013)	$\frac{da}{dN} = C(\Delta K_{eff})^m$
	Liu et al. (2009); Colombi et al. (2015) Hu et al. (2016)	$\frac{da}{dN} = C(\Delta K_{eff}^m - \Delta K_{th}^m)$

Elber's equation was used in cases where stress ratios are different in different coupons. For example, in Huawen et al. (2010), prestressed CFRP was used to reinforce fatigue damaged steel plates. The prestressing force induced compressive stress in the steel and resulted in actual stress ratios in the steel ranging from -0.9 to 0.4 depending on the prestressing level. Therefore, the Elber's equation was used to perform the fatigue crack growth analysis and the fatigue life prediction. The reported difference between the predicted and measured average fatigue lives were 18% and 34% for prestressing levels of 0 and 600 MPa, respectively. The Elber's equation was further modified in some other studies (Liu et al., 2009; Columbi et al., 2015; Hu et al. 2016) as

$$\frac{da}{dN} = C(\Delta K_{eff}^m - \Delta K_{th}^m) \cdot \tag{2.21}$$

Those studies did not clearly demonstrate advantages or disadvantages of this modified approach.

The values of the parameters in these models are critical to the accuracy of the prediction. Table 2.2 summarizes values of the parameters that were used in the mentioned studies and the details of how those values were obtained. The experimental calibration provides more accurate properties. However, for cases that the experimental calibration is limited, the suggested values could be used for an approximate estimation as long as the values are selected properly.

Table 2.2 Values of material parameters for Paris and Erdogan equation

References	Material	Methods	C[a]	m[a]	U	ΔK_{th}
Lee and Lee (2005)	Al 7075-T651	Experimental	[b]	[b]	N/A	N/A
Sabelkin et al. (2006)	Al 2024-T3	Dowling (1999)	1.42×10^{-11}	3.59	N/A	N/A
Liu et al. (2009)	Steel	JSSC (1993)	1.50×10^{-11}	2.75	[c]	2.90
Tsouvalis et al. (2009)	Steel	Experimental	4.40×10^{-12}	3.24	N/A	N/A
Huawen et al. (2010)	Steel	Assumption	Not indicated	3.00	[d]	N/A
Wu et al. (2012)	Steel	JSSC (1993)	1.50×10^{-11}	2.75	N/A	N/A
Yu et al. (2013)	Steel	JSSC (1993)	1.50×10^{-11}	2.75	N/A	N/A
Wang et al. (2013)	Steel	Experimental	2.77×10^{-12}	3.53	$0.69+0.45R$	N/A
Liu and Zhao (2013)	Steel	BS 7910 (2005)	2.30×10^{-12}	3.00	N/A	2.00
Feng et al. (2014)	Steel	Assumption	6.77×10^{-13}	2.88	[c]	2.90
Colombi et al. (2015)	Steel	Experimental	2.43×10^{-12}	3.31	[e]	5.12

[a]the values are adjusted for ΔK in MPa $m^{1/2}$ and da/dN in m/cycle for comparison
[b]the parameters change with the thickness of the tested coupon, $C = 9.26\times10^{-10} \sim 3.45\times10^{-11}$, $m = 2.46\sim3.97$
[c]$U= (1-\sigma_{op}/\sigma_{max})/(1-R)$, σ_{op}/σ_{max} can be found in (Liu et al., 2009)
[d]$U = 1$ ($R \geq 7$), $0.69 + 0.45R$ ($-0.5 \leq R < 0$), 0.465 ($R < -0.5$)
[e]$U = (1-q)/(1-R)$, $q = \sigma_{op}/\sigma_{max}$ (Colombi et al., 2015)

Other than the Paris-Erdogan and Elber's equations, other models have been proposed by considering other parameters such as the critical stress intensity factor, K_c (Forman et al., 1967). However, these models do not necessarily provide more accurate fatigue crack growth analysis or fatigue life predictions (Sanford, 2003). Nevertheless, inappropriate selection of the parameter values may result in inaccurate prediction. One such example is the model proposed by Forman et al. (1967):

$$\frac{da}{dN} = \frac{C(\Delta K)^m}{(1-R)K_c - \Delta K}. \tag{2.22}$$

The computer program NASA/NASGRO 3.0 (2000) adopted a modified version of Eq. (2.22) as

$$\frac{da}{dN} = \frac{C(1-f)^m \Delta K^m \left(1-\frac{\Delta K_{th}}{\Delta K}\right)^p}{(1-R)^m \left(1-\frac{\Delta K}{(1-R)K_c}\right)^q}, \tag{2.23}$$

where f is a plasticity-induced crack closure function that is defined as $f = K_{op}/K_{max}$. Parameters C, m, p and q are empirically fitted constants. Details of using Eq. (2.23) for fatigue crack analyses can be found in (Yu et al., 2014; Chen et al., 2014; Yu et al., 2015; Yu et al., 2016).

2.5 Small crack propagation analysis theories

The size of small cracks was categorized as: microstructurally small cracks (comparable to the grain size of a metal), mechanically small cracks (comparable to the plastic zone size), and mathematically small cracks (typically less than 1 mm) (McEvily, 1998). In this sense, most of the previous studies regarding FRP strengthening metallic members have focused on the fatigue behavior starting from an existing long crack. Namely, the crack initiation and small crack propagation were not considered. However,

it has been reported independently that the majority of the fatigue life of a metallic member with smooth surface was spent during the crack initiation and the small crack propagation stages (Hussain, 1997; Wang et al., 2002; Komano et al., 2007). As a result, the investigation of FRP strengthening un-cracked fatigue-sensitive detail is significant. Also, identifying an effective approach of simulating the crack initiation and small crack propagation may be important.

The behavior of short fatigue cracks is much different from that of long cracks. Figure 2.12 shows the schematic plot of da/dN against the ΔK for small cracks and long cracks (Pearson, 1975; Lankford, 1982; Phillips, 1988; Kaynak, 1996; Newman et al., 1999). The dashed curves show the behavior of small cracks, while the solid curve shows the behavior of a long crack that is obtained from load-reduction (ΔK-decreasing) tests. It can be seen that the small crack not only is able to propagate below the 'crack growth threshold', ΔK_{th}, but also exhibits much higher crack growth rates. Three major causes of the anomalous behavior of small cracks that have been identified during the past decades are: the large size of the plastic zone compared to the crack length, the microstructures including grains and boundaries, and less influence of the crack closure effect. All of these contribute to the deficiency of LEFM to predict the anomalous behavior of small cracks. Lukáš and Kunz (2003) presented a review about the crack nucleation and small crack growth. Quantitative description of microstructurally small cracks and mechanically small cracks were reviewed. It was pointed out that there was no generally accepted and applicable description of the propagation rate of the microstructurally small cracks. Further, the mathematical models for the mechanically small cracks were either inconvenient or left further questions to be answered.

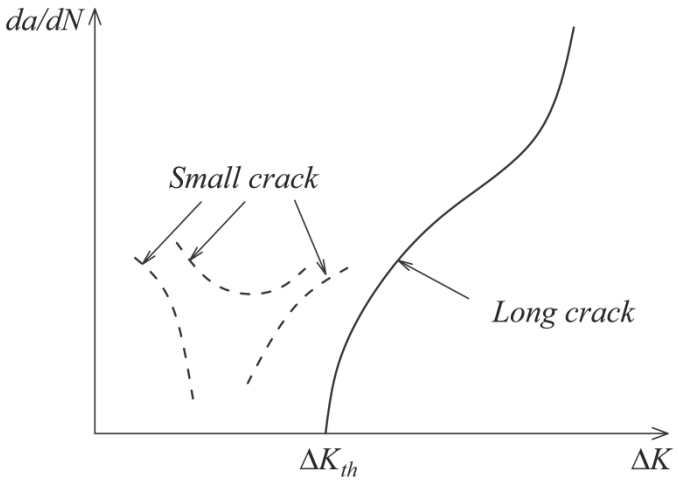

Figure 2.12 Schematic drawing of small crack behavior (adapted from Newman et al., 1999)

The concept of equivalent initial flaw size was developed through an effort to use LEFM to extrapolate the behavior of known large cracks back to "time zero" in order to estimate the initial flaw size (Johnson, 2010). Since the long crack propagation model rather than the small crack behavior was used to perform the extrapolation, the obtained flaw size at "time zero" was not equal to the actual initial flaw size. Figure 2.13 shows the schematic illustration of EIFS. Ideally, the fatigue life, *N*, is calculated by integration of the fatigue crack growth rate along the crack length from the actual initial flaw size (IFS) to the failure crack length, which is the area under the dashed curve in the figure. In the small crack stage, the stochastic small crack growth rate is used; while the LEFM approach can be used in the long crack stage. The EIFS approach, on the other hand, uses the long crack propagation model for all the crack lengths without special treatment of the small crack stage. Doing so would underestimate the average crack growth rate in small crack regime. Therefore, the EIFS value, the starting point of the crack growth analysis, is larger than the real initial flaw size. The predicted fatigue life is the area under the solid curve. In this way, as long as an EIFS value is selected properly so that

the two areas are equal, the predicted and actual fatigue lives will be equal. This method has been given wide attention recently since it avoids the difficulties of measuring the IFS, which is at the level of the grain size; and simulating the small crack growth, which is stochastic in nature. Instead, the identification of an EIFS value indirectly accounts for any nucleation cycles and the mismatch between small crack and long crack propagation rates.

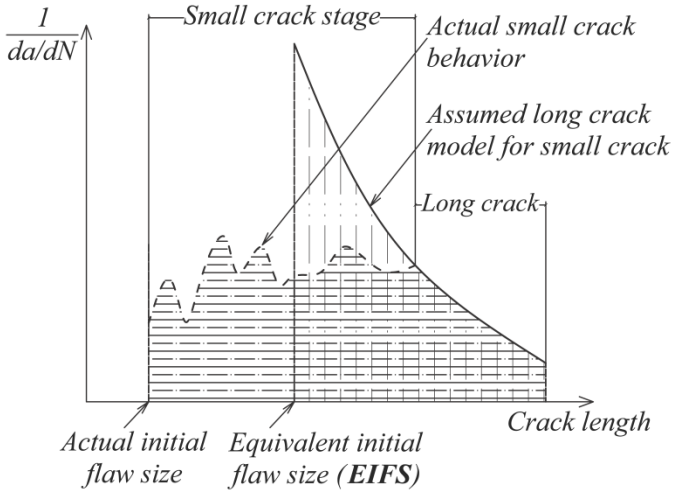

Figure 2.13 Illustration of EIFS(Adpted from Liu and Mahadevan, 2009)

Newman et al. (1999) investigated the prediction of fatigue lives of metallic materials including 2024-T3 and 7075-T6 aluminum alloys and 4340 steel using EIFS concept. The ΔK_{eff} vs. *da/dN* relationships for long cracks of the three materials were obtained from other studies. A crack-closure model that considers the 3-D constraint effects of the crack propagation was employed to perform the entire fatigue life analysis. The EIFS values in the analysis were selected by a trial-and-error approach to find the best fit to the test data. For example, an EIFS value of 20 μm for the aluminum alloys 2024-T3 and 7075-T6 exhibited close fit to the test data for both stress ratios of 0 and -1; an EIFS value of 10 μm was selected for the analysis of steel 4340. Liu and Mahadevan

(2009) proposed a methodology to calculate the EIFS distribution based on Kitagawa-Takahashi diagram. By using the fatigue limit and fatigue crack growth threshold SIF, the EIFS can be calculated independent of the applied load level. Xiang *et al.* (2010) investigated fatigue crack growth under uniaxial loading using the EIFS model. Experimental data for both un-cracked steel and aluminum coupons that were tested under fatigue loading at stress ratios of -1, 0 and 0.1 were collected. Fatigue life prediction using the EIFS approach was carried out and the results were compared with the experimental data. Overall close agreement between the prediction and experimental data was observed for both smooth and notched specimens. Shahani and Kashani (2013) assessed three methods of calculating EIFS values using the experimental data of six compact tension coupons: i) the back extrapolation method, it estimates the EIFS by comparing the measured and predicted fatigue life, ii) the Kitagawa-Takahashi diagram method, it considers the EIFS as a material property, and iii) the time-to-crack-initiation method, it calculates the EIFS by looking for crack length corresponding to zero cycle in the crack length vs. number of cycles (a-N) curve. The first exhibited the best accuracy with the error of predicted fatigue life ranging from 0.008% to 0.026%. The EIFS values that were predicted using this method were found to be dependent on the applied load amplitude. The second method provided the same EIFS value for coupons tested under different load range. The error of the predicted fatigue life ranged approximately from 5% to 50%. The fatigue life prediction using the EIFS values obtained from the third method exhibited insufficient accuracy, especially for the coupons tested under relatively low load range.

Ghafoori et al. (2015) introduced a design criterion for fatigue strengthening of steel beam using prestressed CFRP plates. The constant life diagrams (CLDs) method was used to calculate the required prestressing level to prevent crack initiation. Based on the modified Goodman and modified Johnson criteria, the safe region of the stress amplitude and mean stress of the steel under fatigue loading was identified. The prestress level of the CFRP plate was determined by letting the stress of the beam in the safe region. However, it was pointed out in the paper that the CLD method was only used to prevent fatigue crack initiation. For existing cracks, a LEFM based model shall be used to determine the required prestressing level to arrest the fatigue crack propagation.

2.6 Characteristics and applications of shape memory alloys

Shape memory alloys are a unique class of materials which exhibit superelasticity and shape memory effect. When it is in austenitic phase, SMA materials exhibit a superelastic behavior having large elastic deformation and energy absorption abilities. The most common structural application of SMA has been seismic damping, which leads to extensive investigations on the cyclic behavior of superelastic SMAs (Tobushi et al., 1996; Dolce and Cardone, 2001). Nickel-titanium (NiTi) has been largely exploited due to their superior properties in ductility, strength, fatigue, resistance to corrosion, and biocompatibility (Miyazaki et al., 1986; Maletta et al., 2012).

When it is in martensitic phase, considerable recovery stress can be generated using SMAs by restraining the thermally-induced shape transformation (Sittner et al., 2000; Bollas et al., 2007). The shape memory effect has drawn much attention for novel applications such as weld-free pipe coupling (Jee et al. 2006) and confinement of concrete members (Andrawes et al., 2010; Shin and Andrawes, 2010). In these

applications, it usually requires unique types of SMA with wide thermal hysteresis rather than traditional NiTi alloy.

In addition, SMAs have been embedded into FRP matrices to fabricate SMA/FRP composite materials. Fiber reinforced polymer (FRP) composites have been widely used as load carrying members due to their light weight and versatility. Martensitic shape memory alloys (SMA) are embedded in FRP components to actively tune the properties of the composites (Epps and Chandra, 1997; Baz et al. 2000; Song et al., 2000a; Song et al., 2000b; Icardi, 2001; Loughlan et al., 2002). Similarly, SMAs are embedded in FRP components to increase the energy dissipation capacity of the composites (Turner 2005; Liu et al., 2007, Wierschem and Andrawes, 2010; Raghavan et al., 2010). In both cases the effectiveness of the martensitic SMA/FRP composite relies on establishing an effective bond between the two materials.

2.6.1 Cyclic behavior of superelastic SMA materials

Miyazaki et al. (1986) investigated the effect of low cycle fatigue on the pseudoelalsticiy of nickel-titanium (NiTi) alloys. It was found that stress cycles: i) increased the residual strain, ii) decreased the critical stress inducing martensitic transformation, and iii) decreased strain hysteresis. These effects occurred during stress-induced transformation rather than in the elastic range. Therefore, the superelasticiy could be stabilized by increasing the critical stress inducing the transformation. Aging and annealing treatments were used to raise the critical stress. Results showed that the combined treatment of aging and annealing followed by a cyclic training was most effective in stabilizing pseudoelasticity. The stress-strain curve of the treated alloy hardly changed after 100 stress cycles.

Graesser and Cozzarelli (1991) exploited the application of NiTi SMA material in seismic isolation. A modified SMA hysteretic model based on the Ozdemir's model (Ozdemir, 1976) was proposed. Cyclic tests consisting of five successive cycles with ±3.0% peak strain at 1.0×10^{-4} and $3.0 \times 10^{-4} sec^{-1}$ strain rates were conducted to investigate the full hysteresis of NiTi alloy. The full hysteresis loop exhibited non-symmetric response in tension and compression. For each repeated cycle, the loop was observed to shift by small increment. Results also showed that the yielding points for tension and compression varied slightly due to the increase of strain rate; while the inelastic uniaxial response was rate-dependent. Finally, results indicated close agreement between the modified model and the experimental results.

Tobushi et al. (1996) conducted high cycle rotating-bending fatigue tests on NiTi alloy wires in air and water to investigate the influence of martensitic and rhombohedral-phase transformations on the thermomechanical properties. The tests were conducted at different constant temperatures with a rotational speed of 500 rpm. Results showed that the fatigue life of the NiTi wire reached up to 10^6 cycles when the surface strain was in rhombohedral-phase transformation region in air; and it was 10^7 cycles in water.

Dolce and Cardone (2001) conducted cyclic tensile tests on NiTi SMA wires to investigate the suitability of using SMA wires as key components for seismic protection devices. SMA wires with diameters of 1-2 mm and length of 200 mm were tested at 0.01 to 4 Hz frequency with peak strain of up to 10%. Also, cyclic testing under temperature ranging from -10^oC to 40^oC was conducted. Results indicated that the stress cycles considerably decreased the energy absorption capability of the SMA wires at the first few cycles. The behavior stabilized in the following loading cycles. It was recommended that

pre-training should be used to achieve stable behavior of the SMA wires in seismic applications. The SMA wires tested under temperatures and loading frequencies within the useful range for seismic applications exhibited stable behavior.

Malécot et al. (2006) studied the cyclic behavior and thermal dissipation of SMA material by testing three materials of nickel-titanium (NiTi), austenitic and martensitic copper-aluminum-beryllium (CuAlBe) alloys. Results showed the strain rate had a significant impact on the mechanical behavior of NiTi alloy but not the CuAlBe alloys. A model based on a general thermodynamic framework with complete heat equation was proposed to predict the cyclic behavior of SMAs. A method of modeling the nonlinear behavior of SMA during dynamic loading was presented. The combined model was used to predict the behavior of the tested material and validated by the experimental data.

Tyber et al. (2007) investigated the multiscale material characterization of NiTi SMA for structural applications. NiTi bar with diameters of 31.8, 19.1 and 12.7 mm were used in the research. It was found that low temperature heat treatment resulted in precipitation. The hot-rolled bars demonstrated a one-step forward and reverse martensitic transformation.

Torra et al. (2009) investigated using NiTi and CuAlBe alloys for seismic control applications considering fatigue, time and temperature, and loading effects. It was found that the CuAlBe alloy was not suited for practical use of damping against seismic conditions due to its insufficient fatigue life. However, results indicated NiTi alloy could be used in damping of stay-cables.

Maletta et al. (2012) conducted strain-controlled fatigue tests of twenty pseudoelastic NiTi alloy dog-bone coupons up to failure. The fatigue loading was divided

into two steps: i) cycles to stabilization, i.e. no residual strain after stress cycles, and ii) cycles to failure. The coupons were loaded to different maximum strain levels ranging from 0.7 to 4.5 %. It was found that the cycles to stabilization was insensitive to the applied maximum strain level and close to 100 cycles. For the coupon loaded with 0.7% maximum strain level, the cycles to stabilization was 120; while it was 140 for the coupon loaded with 4.5% maximum strain level. The cycles to failure, however, changed substantially with respect to the applied maximum strain level. The fatigue life for 0.7% and 4.5% maximum strain level were 13495 and 340 cycles respectively.

2.6.2 Structural damping applications of SMA members

Tamai and Kitagawa (2002) investigated using SMA components as structural dampers. An exposed-type column base anchorage and a SMA braced frame were proposed. The restoring force of the SMA material was studied through tension tests. A numerical model was developed to predict the restoring force of the SMA under seismic conditions.

Andrawes et al. (2004) evaluated four different models for austenitic SMA behavior in terms of accuracy and ease of implementation. A nonlinear elastic model, a trigger line model, and a one-dimensional thermomechanical model with and without considering the cyclic loading effects were employed to predict the seismic behavior of a bridge and a frame models. Results indicated that despite the obvious different behaviors for the SMA in each model, the predicted structural responses using the four models were similar. For example, in the analysis of the bridge model, the maximum predicted hinge openings for the four models were 2.65, 2.69, 2.95 and 3 inch, respectively. Similar

tendency was observed for the frame analysis. These results recommended that using simplified models in predicting structural behavior of SMA in seismic applications.

McCormick et al. (2007) studied the seismic performance of concentrically braced frames using superelastic SMA braces in comparison to traditional systems. The maximum inter-story drift and residual roof displacement of SMA and steel braced frames for three-story and six-story cases were studied. Results showed that the average peak inter-story drifts for steel braced frames were 8.1 and 4.7% for three- and six-story frames; they were 1.8 and 1.9% for SMA braced structures. For the residual roof displacement, they were 1.8 and 0.57% for steel braced structures; while 0.15 and 0.2 % for SMA braced structures.

Zhang and Zhu (2008) performed the numerical analysis of a full scale three-story steel frame equipped with NiTi SMA wire dampers. Cyclic tensile tests were conducted to calibrate the parameters in the employed one-dimensional SMA material model. The stabilized SMA properties after 100 cycles of training were used. The analyses of the seismic response of the three story frame equipped with unprestrained and prestrained SMA wires were conducted. Results showed both types of dampers could reduce the peak drift ratios of the frame, while both types of dampers tend to increase the peak acceleration of the frame due to the their increased stiffness. The prestrained SMA damper was generally more effective in reducing the drift ratio and acceleration than the unprestrained one.

2.6.3 Shape memory effect applications of SMA materials

Prestrained shape memory alloy (SMA) materials exhibit a unique thermo-mechanical response through which, when they are heated, they return to their un-

prestrained geometry. By restraining this transformation, prestrained SMAs can be used to apply recovery forces, or prestressing forces, to structural elements. This property of SMA materials has been exploited to develop composites that are able to actively tune their mechanical response. Shimamoto *et al.* (2004) reported an investigation using nickel-titanium (NiTi) shape memory alloy wires to actively control the strength of an SMA/epoxy composite. In the study, prestrained SMA fibers were embedded into an epoxy coupon, which had a side crack at one edge. By heating the composite, the shape memory effect of the SMA reduced the stress at the crack tip by inducing compressive stress in the epoxy. Furthermore, the stress intensity factor (SIF) at the crack tip decreased as the prestrain level increased. For composites with a SMA volume fraction of 0.47% and prestrain level of 0.05 mm/mm, the SIF at the crack tip was reduced by 60%.

Tsoi *et al.*, (2004) investigated the thermo-mechanical behavior of nickel-titanium-copper (NiTiCu) SMA composites. SMA wires with prestrain levels of 0, 1, 2, 3, 4 and 5% were embedded between two layers of aramid pre-preg. The composite specimens were tested using a tensile testing machine. The SMA-composite generated recovery stresses of up to 115 MPa. Bollas *et al.*, (2007) investigated the capability of SMA wires as stress generators in epoxy/aramid fiber composites at both macro- and micro- scale. In the study, a single SMA wire was embedded between two pre-impregnated plies of aramid fiber. The cured composite specimen was axially restrained. Results showed that during heating activation, the SMA wire was able to generate a gross cross-section stress of 5 MPa and a stress in the SMA wires of 227 MPa.

Shin and Andrawes (2010) studied the use of SMA spirals in confining concrete members. Cylinders wrapped with SMA spirals, with GFRP sheets, and with SMA

spirals and GFRP sheets were tested to evaluate the effectiveness of the SMA material in confining concrete columns. Results showed the specimens strengthened with SMA spirals exhibited 24 times the ultimate strain of the un-strengthened ones. In another study (Zafar and Andrawes, 2013), NiTi SMA wires with diameter of 500 μm were embedded into glass FRP (GFRP) matrix to fabricate a SMA/FRP composite rebar with 3.2 mm × 3.2 mm square cross-section. The composite rebar was used as flexural reinforcement in a small scale concrete T-beam with 250 mm length, 51 mm depth, 64 mm flange width and 25 mm web width. The beam was tested under 3-point bending. Results showed that the SMA/FRP composite rebar could reduce the accumulation of permanent damage and residual displacement.

2.6.4 Bond between SMA and FRP

Several researchers have studied the effect of surface treatment methods on the bond behavior of SMA. Jonnalagadda et al. (1997) investigated the effect of the surface treatment of SMA wires embedded in an epoxy matrix on the bond strength using pull-out tests. Different surface treatments were investigated: untreated, acid-etched, hand sanded, and sandblasted. Sandblasting provided the highest bond strength, while acid etching and hand sanding were less effective methods of enhancing the bond properties. Jang and Kishi (2005) examined different methods of acid etching to increase the bond strength between NiTi SMA wires and carbon FRP (CFRP). They found that the bond strength increased 3% to 18% compared to the untreated wires. Acid etching with a 3% hydrofluoric acid and 15% nitric acid solution produced the highest bond strength of the treatment methods studied. The increase in the interfacial bond strength was attributed to the surface roughness caused by the acid etching. Sadrnezhaad et al. (2009) evaluated the

bond behavior between austenitic NiTi SMA and a silicone-based matrix for medical applications. SMA wires with different surface treatments were investigated under scanning electron microscopy and pull-out tests were conducted to determine the morphological and bonding interactions with the silicone matrix. Acid etching and oxidization increased the frictional forces at the interface which led to an increase in the bond strength.

Using scanning electron microscopy Lau et al. (2002) examined the debonding failure mechanism of prestrained martensitic SMA wires embedded in an epoxy matrix. For wires that were prestrained up to 8% debonding occurred at the SMA-epoxy interface when the wires were heated beyond the austenitic finish temperature (A_f). Heating caused the surrounding epoxy to expand while the SMA wires contracted due to the shape memory effect. This induced large shear stresses which led to debonding of the highly prestrained wires. As such, it was recommended to prestrain the SMA wires to less than 8% to reduce the interfacial shear stresses.

Poon et al. (2005a, 2005b) studied the interfacial bond behavior of prestrained martensitic SMA wires embedded in an epoxy matrix. A model was developed to predict the debonding behavior, initial debonding stress, and critical bond length (Poon et al., 2005a). The maximum debonding stresses at different activation temperatures were predicted and compared with experimental results. The model accurately captures the change in the critical embedment length with the increase of the activation temperature. Also, a phase-stress-displacement diagram was developed that can be used to determine the critical pull-out stress of prestrained martensitic SMA wires embedded in an epoxy matrix during activation (Poon et al., 2005b). Wang et al. (2011) developed a closed-form

solution to analyze the stress distribution along the SMA-epoxy interface when the shape memory effect of a SMA wire embedded in cylindrical epoxy matrix is activated. A finite element analysis was also conducted to validate the closed-form model. Both the closed-form solution and the finite element analysis indicate that the maximum interfacial shear stress is located at the ends of the SMA wire while the maximum axial stress is at the midpoint of the embedded SMA wire. Both the axial stress and the interfacial shear stress increased with the increase of the actuation temperature. The maximum interfacial shear stresses were proportional to the prestrain level, while the maximum axial stress in the SMA increased nonlinearly.

Payandeh et al. (2009) examined the bond behavior of martensitic NiTi wires embedded in a cylindrical epoxy matrix by pull-out tests. Three heat treatments were applied to the NiTi wires in order to achieve three martensitic transformation characteristics. The effect of the loading rate on the debonding behavior was also studied. A digital camera behind a polariscope was used to observe the debonding process during the test. Based on the test results it was concluded that the bonded part of the wire cannot experience transformation since transformation induces large strains. Debonding occurred if the debonding load was smaller than the transformation load. In a companion study the effect of the martensitic transformation on the debonding initiation of martensitic SMA wires embedded in an epoxy matrix was investigated (Payahdeh et al., 2010). It was found that the maximum interfacial shear stress depends on the wire's elastic modulus. The interfacial shear strength for specimens with SMA wires was less than that of specimens with steel wires. Based on the experimental observations the interfacial shear strength was about 9 MPa for specimens that exhibited no phase

transformation, and 14 MPa when martensitic transformation occurred. Payandeh et al. (2012) studied the effect of the martensitic transformation on the debonding initiation in non-prestrained SMA wire-epoxy matrix composites. SMA wires were embedded in an epoxy coupon to achieve 6% and 12% SMA volume fractions. Epoxy coupons with SMA volume fractions of 6% were tested in tension at 20^{o}C, 80^{o}C, and 90^{o}C, while specimens with SMA volume fractions of 12% were tested at 80^{o}C and 90^{o}C. Increasing the SMA volume fraction enhanced the mechanical behavior of the composite. Increasing the test temperature increased the tensile strength of the composites while the tensile strength of the epoxy decreased. The martensitic transformation occurred in multiple locations in the embedded wires causing a bonded/debonded pattern.

2.6.5 A thermally-activated self-stressing SMA/FRP composite for fatigue strengthening

El-Tahan *et al.* (2015) developed a SMA/FRP patching system for repairing fatigue sensitive or fatigue damaged steel members. The system consists of a SMA patch providing recovery stress under thermal-activation, and a FRP overlay bridging the fatigue crack. A wide thermal hysteresis nickel-titanium-niobium (NiTiNb) alloy wire with diameter of 0.77 mm was used to fabricate the SMA patch. Single wire testing showed that the wire was able to generate 390 MPa of recovery stress under thermal activation. The recovery stress in the wire was retained when cooled to room temperature. Further, by heating up to 165^{o}C and cooling to room temperature the wire for 12 cycles, the recovery stress in the wire reduced by 18%. The SMA patch was fabricated by embedding the SMA wires into CFRP matrix. A critical development length of 51 mm was identified through pull-out tests. Also, a wire spacing of 0.89 mm

appeared to be able to prevent premature debonding of the wires from CFRP patches due to influences between adjacent wires. It was found that targeted heating of the wire did not affect the bond between SMA and FRP, although the 165^{o}C activation temperature of the SMA wires exceeds the softening temperature of the epoxy. The SMA patch embedded with ten 0.77 mm diameter SMA wires generated a prestressing force of 1750 N. Monotonic tensile testing showed that the capacity of the patch was twice the prestressing force.

In a subsequent study, El-Tahan and Dawood (2016) investigated the fatigue behavior of the SMA patch. Ten 0.77 mm diameter × 306 mm long NiTiNb SMA wires were embedded 102 mm at two ends into CFRP tabs leaving the central 102 mm exposed for thermal activation. A total of 14 coupons were fabricated and tested under tension-tension fatigue loading. Two prestressing levels, 250 and 390 MPa, and four stress ranges, 20, 50, 80 and 200 MPa were considered. Results showed that when the maximum stress in the SMA wire due to the prestress and the applied loading was below the stress required to cause debonding of the SMA from the FRP, the prestress level decreased by 8%, 12% and 23% after 2 million load cycles at stress ranges of 20, 50 and 80 MPa, respectively. When the maximum stress in the SMA was greater than the onset load of debonding, and the SMA wires were partially activated, a sudden loss of 40% prestress was observed. Coupons with full activation of the SMA wires completely lost the prestress after approximate 30,000 fatigue cycles. Taken collectively, it was suggested that the combined maximum stress in the SMA should be lower than the stress at the onset of debonding in fatigue applications to prevent loss of prestress.

2.7 Research significance

This research fulfills the urgent need of identifying an innovative fatigue strengthening technology by exploiting the newly developed SMA/FRP composite patching system that is able to practically apply prestress to FRP material and potentially effectively improve the fatigue performance of cracked steel element. Through fatigue testing of fatigue sensitive steel coupons patched with this composite the effectiveness is quantified.

The fatigue cracking related interfacial debonding of FRP-metal system is investigated in this research. First, through the experimental data, the initiation and propagation mechanisms of the debonding are revealed. Further, based on the understanding a numerical model that is able to simulate the debonding is developed and validated using the experimental data. This model may be used to other similar studies regarding FRP-metal system under fatigue loading.

A comprehensive numerical framework was developed to simulate the fatigue crack growth of SMA/FRP composite reinforced steel elements. This framework is able to incorporate the accurately predicted interfacial debonded region and the small crack propagation regime, which have not been previously presented. In addition, the other components of this framework are selected by considering the advantages and disadvantages of all the existing models, which is instructional to other similar studies.

Chapter 3 : Fatigue strengthening of steel members using a thermally-activated self-stressing SMA/FRP system

This chapter presents the experimental work conducted to quantify the fatigue life improvement that can be achieved using the developed thermally-activated SMA/FRP strengthening system. The fabrication and installation of the SMA/FRP patching system is introduced and explained. The strengthening effects and mechanism are discussed based on the experimental results. It also investigates the interfacial debonding between the SMA/FRP patch and the steel substrate during fatigue loading. The influence on the fatigue strengthening using the system is identified.

3.1 The thermally-activated SMA/FRP patch

The SMA/FRP patch used in this research consists of a SMA patch with 46 SMA wires embedded, and a CFRP overlay made of HM carbon fiber. The SMA wires were employed to replace the conventional prestressing method by applying compressive stress to the steel substrate. The CFRP overlay was designed to bridge the crack path and protect the underlying SMA patch.

The SMA material employed in this research is nickel-titanium-niobium (NiTiNb) alloy that has a wide thermal hysteresis to maximize the retention of the recovery stress when the ambient temperature decreases to room temperature after thermal activation. Specifically, the NiTiNb SMA wires used in this research were manufactured by Intrinsic Devices Inc.. The wires were provided with a recoverable prestrain of 0.05 mm/mm and a grit blasted surface. As reported by the manufacturer, the austenite start temperature, A_s,

austenite finish temperature, A_f, martensite start temperature, M_s, and the martensite finish temperature, M_f, are 50˚C, 165˚C, -65˚C and -120˚C, respectively. Figure 3.1 shows the results of three wires tested to obtain the temperature-recovery stress relationship. The wire was fixed between two grips connected to a load cell, and then heated to record the temperature-recovery stress relationship. The wire was initially at 25˚C. By heating the wire, a recovery stress was generated with the increase of the temperature. After heating the wire to 160˚C, the recovery stress in the wire was 400 MPa. When the wire was cooled to room temperature, the recovery stress remained constant as shown in the figure. The theoretical temperature-recovery stress relationship below 25˚C is plotted as a dashed line in the figure. Others have indicated that in similar patches with multiple SMA wires the recovery force that can be achieved is proportional to the number of wires (El-Tahan et al., 2015; El-Tahan and Dawood, 2016).

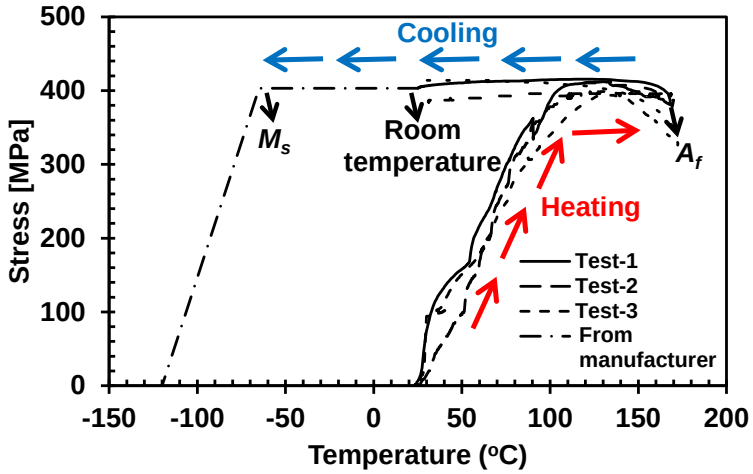

Figure 3.1 Temperature and recovery stress relationship of the NiTiNb SMA wire

In order to attach the SMA wires to the surface of the element to be repaired, the SMA wires were embedded in CFRP tabs. The NiTiNb SMA wires, HM carbon fibers (Mitsubishi Dialed K637400) and Araldite 420 saturating resin were used to fabricate the

patch. Each end of the 0.78 mm diameter × 230 mm long SMA wires was sandwiched between two layers of 0.19 mm thick HM carbon fiber fabric. The wires had a spacing equal to the wire diameter and an embedment length of 76 mm at each end. Forty-six wires were used in each patch. To hold the wires in position, 0.78 mm diameter × 230 mm long superelastic NiTi wires were placed in between each pair of neighboring NiTiNb wires, as shown in Figure 3.2(a). The wires were all temporarily held in place using transparent tape. The wires were positioned on top of one layer of carbon fiber fabric with 76 mm embedment length. The NiTiNb wires were stitched to the fabric using needle and thread along four transverse lines. The same procedure was repeated on the other end. The tape and the NiTi spacers were then removed leaving the NiTiNb wires stitched in position to one layer of the CFRP. Subsequently, the carbon fabric was saturated with Araldite 420 resin and sandwiched between two plastic molds. The patch was left to cure for 7 days. Figure 3.2(b) shows the SMA patch after curing. The SMA wires in the middle segment were intentionally exposed to facilitate the thermal activation after being attached to the surface of the steel element.

Figure 3.3 illustrates the process of strengthening the single edge-notched steel plate using the SMA patch and a CFRP overlay. Figure 3.3(a) shows the 914 mm long × 102 mm wide × 6.4 mm thick bare steel plate to be strengthened. A 6.35 mm deep, 60 degree edge notch was generated at the center of one edge to induce a stress concentration, as shown in the figure. Figure 3.3(b) shows the plate surface after sandblasting with #4 blast sand and cleaning with 70% isopropyl alcohol and acetone prior to the installation of the SMA patch. The SMA patches were bonded to both sides of the steel plate using a two-part structural epoxy, Spabond 345. The exposed SMA

wires were placed over and perpendicular to the anticipated crack path, as shown in Figure 3.3(c).

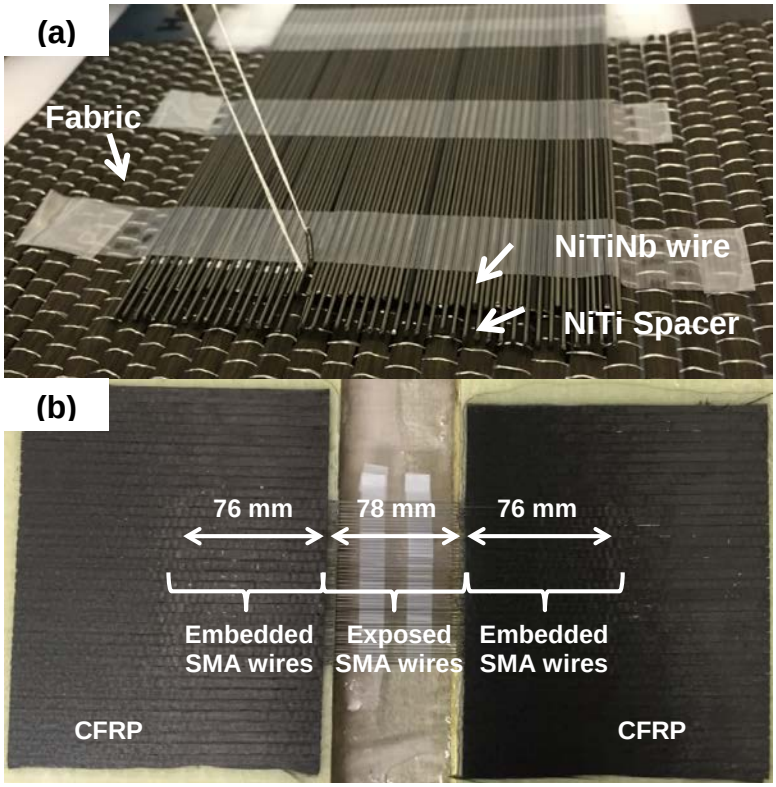

Figure 3.2 SMA wires embedded into CFRP tabs

The SMA wires were activated after the epoxy cured for seven days. As illustrated in Figure 3.3 d), the CFRP tabs on both sides of the plate were thermally isolated using glass fiber insulation and aluminum foil tape to prevent debonding between the SMA wires and the CFRP matrix and between the CFRP and steel substrate. Fiberglass batt insulation was cut into a 90 mm wide × 250 mm long strip. The strip was wrapped around the specimen to cover the CFRP tabs on both sides of the steel plate such that the insulation covered a 10 mm length of the exposed SMA beyond the end of the CFRP tab. Aluminum foil tape was used to affix the fiberglass insulation to the specimen and to provide an additional thermal barrier The objective of the insulation was to prevent

direct heating of the CFRP patch in the embedment region by the forced air. Previous results that evaluated thermal distributions in electrically heated NiTiNb demonstrated that for heating times on the order of 10 minutes, thermal conduction along the wires did not result in any appreciable increases of temperature outside of the activated region of the wire (El-Tahan et al. 2015).

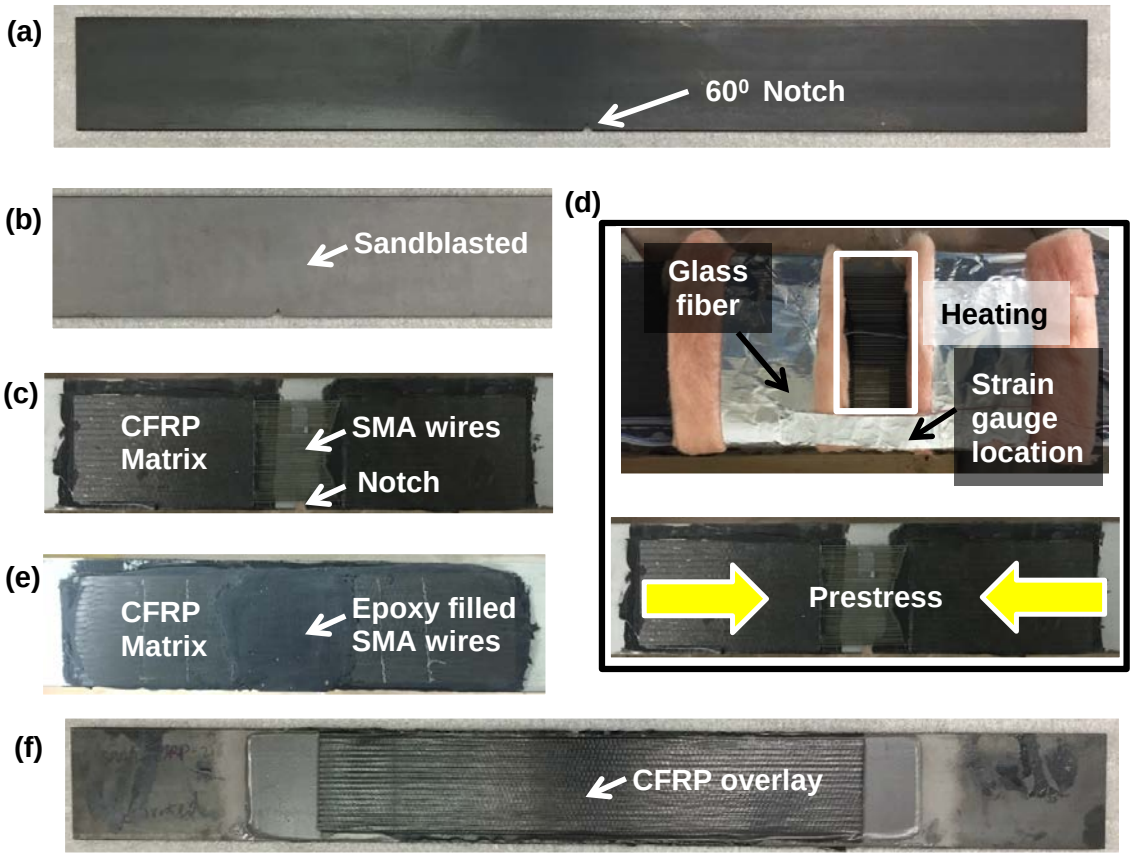

Figure 3.3 Illustration of the process of strengthening steel plate with SMA/CFRP patch

Two strain gauges were installed close to the notch root on both sides of the steel substrate to record the strain in the steel during and after the activation. Two thermocouples were placed beneath the SMA wires to record the temperature change. Three specimens, each with one 0.78 mm × 200 mm NiTiNb wire embedded into a HM CFRP tab, were tested to determine the potential for debonding of the SMA/CFRP patch

during activation. It was found that by heating the wires up to 160^{o}C while restrained (corresponding to a recovery stress in the wires of 400 MPa), no debonding occurred at the SMA/CFRP interface. However, others have observed debonding of the NiTiNb wires from the CFRP tabs at stresses of 400 MPa when using the same materials (El-Tahan and Dawood, 2016). They recommended that the combined stress in the SMA wires due to activation plus the maximum stress induced in the wires due to fatigue loading be kept below the debonding stress of 400 MPa. Thus, in the repair application, the exposed SMA wires were conservatively heated up to 120^{o}C using a digitally controlled forced-air heating device and left to cool to room temperature. The same procedure was repeated on the other side of the coupon.

Figure 3.4 shows the relationship between the compressive stress in the steel and the temperature in the SMA wires during the heating process corresponding to step (d) in Figure 3.3. By activating the first side to 120^{o}C, an average compressive stress of 7 MPa was generated in the steel. By activating the other side, the average compressive stress reached a peak value of 19 MPa. Immediate removal of the heating resulted in a sudden decrease of compressive stresses due to thermal contraction of the steel (between 50s and 90s and between 230s and 280s) followed by gradual increase of the stresses due to thermal contraction of the SMA wires (between 90s and 220s and between 290s and 450s). The residual compressive stress in the steel after cooling to room temperature was approximate 17 MPa. The other coupons in the SMA and SMA/CFRP groups exhibited similar trends and magnitudes of residual compressive stresses.

The exposed SMA wires were covered with a structural epoxy paste after activation as shown in Figure 3.3(e) to protect the wires and provide a flat surface on

which to bond the CFRP overlay. Finally, two layers of HM carbon fiber were overlaid on top of the SMA patch. The fiber was impregnated with Araldite 420 epoxy and installed using a hand lay-up technique. Figure 3.3(f) shows the completed repair.

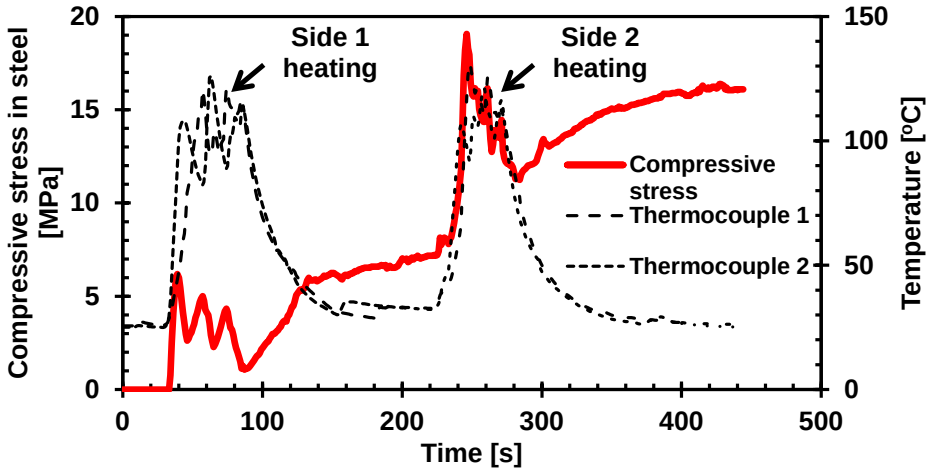

Figure 3.4 Compressive stress in the steel during SMA activation

3.2 Specimens and test setup

Four groups of coupons were prepared and tested under high-cycle tension-tension fatigue loading in this research. Table 3.1 summarizes all of the tested specimen configurations. The tested groups included: (i) un-strengthened, plain steel control coupons, (ii) coupons patched with CFRP only, (iii) coupons patched with prestressed SMA patches only (without the CFRP overlay), and (iv) coupons patched with the SMA/FRP composite patches. Three stress ranges (the difference between the maximum and minimum values of the stress component in the loading direction), 217 MPa, 155MPa and 93 MPa were considered with a nominal stress ratio (the ratio between the minimum and maximum values of the stress component in the loading direction) of 0.1. Each testing configuration was assigned a two-part designation. The first part indicates the specimen detail: plain steel control coupons (Steel), coupons repaired with CFRP

only (CFRP), coupons repaired with SMA patches only (SMA), and coupons repaired with SMA patches overlaid with a CFRP overlay (SMA/CFRP). The second part indicates the far-field stress range of the fatigue test in MPa. Three replicates were tested for each configuration and each specimen has a unique third part serial number to distinguish among multiple repetitions of the same test configuration.

Table 3.1 Test Matrix for all of the configurations

Configuration Designation	Far-field stress range [MPa]	Stress range [MPa]/ stress ratio after strengthening	Reinforcement (each side)
Steel-217	217	217/0.1	Unpatched, control coupons
Steel-155	155	155/0.1	
Steel-93	93	93/0.1	
CFRP-217	217	187/0.1	2 layers of HM CFRP
CFRP-155	155	133/0.1	
CFRP-93	93	80/0.1	
SMA-155	155	155/0	46 SMA wires
SMA/CFRP-217	217	133/0	46 SMA wires & 2 layers of HM CFRP overlay
SMA/CFRP-155	155	187/0.03	

Three steel tension coupons and three Charpy test coupons were fabricated and tested according to ASTM E8 (2013a) and ASTM E23 (2012), respectively. The average measured elastic modulus, yield stress, and room-temperature Charpy V-notch energy of the steel are 200 GPa, 400 MPa, and 67 J respectively. All of the steel plates that were used in this research were fabricated from one batch of material to minimize inter-sample variability. The tensile strength, elongation and elastic modulus of the HM CFRP, obtained from tension coupons tested according to ASTM D3039 (2014), are 345 MPa, 0.0025 mm/mm, and 138 GPa, respectively. The elastic modulus, tensile strength and ultimate strain of the Araldite 420 resin, obtained by coupon test according to ASTM D638 (2010), are 3.05 GPa, 62 MPa and 0.022 mm/mm, respectively. The elastic

modulus, tensile strength and ultimate strain of the Spabond 345 epoxy are 2.26 GPa, 34 MPa and 0.018 mm/mm, respectively.

The fatigue coupons were tested in a MTS servo-hydraulic testing frame with a capacity of 500 kN. All of the coupons were tested under constant amplitude sinusoidal tension-tension fatigue loading with frequency of 10 Hz. A DIC-based non-contact measurement system, ARAMIS, was used to record the strain contours on the surface of the CFRP overlay on one side of the coupons during the fatigue loading. To determine the crack length in the steel substrates at different numbers of fatigue cycles, the beach marking technique (Yu *et al.,* 2013) was employed. Figure 3.5 shows part of the loading history of a specimen and the fracture surface with beach marks to illustrate this technique. Half-amplitude loading cycles were conducted at predefined intervals as shown in Figure 3.5(a). During these reduced amplitude loading packets the crack propagation rate decreased substantially generating a dark band on the fracture surface as shown in Figure 3.5(c). These bands, which were formed at known cycle counts, were used to calculate the crack length at a given number of applied cycles. Since the half-amplitude cycles did not substantially propagate the crack, they were not considered in the total cycle count. The maximum and minimum applied loads were recorded every ten cycles to ensure consistency of the loading protocol. It is seen that the beach marks were slightly asymmetric with respect to the mid-thickness plane due to the difference of the recovery forces of the SMA wires on both sides. Figure 3.5(b) shows the crack front trace on the fracture faces of a single coupon after complete fracture. For convenience, the behavior of the coupons was compared at different stages throughout the loading corresponding to the instances of the reduced-amplitude beach marking cycles. At a

given stage in the loading, the applied number of load cycles, N, was related to the beach marks by counting from the last beach mark and calculating the associated number of full-amplitude loading cycles. If the sample failed during the full-amplitude loading cycles, the number of cycles at failure was taken directly from the test frame controller (after subtracting the cumulative number of reduced-amplitude beach marking cycles). If failure occurred during the reduced-amplitude beach marking cycles, the number of cycles at failure was conservatively taken as the last number of full-amplitude cycles prior to failure. As illustrated in Figure 3.5(b), the crack length corresponding to the i^{th} beach mark, a_i, in this research was measured from the root of the 60° edge notch to the i^{th} beach mark at the mid-thickness of the coupon.

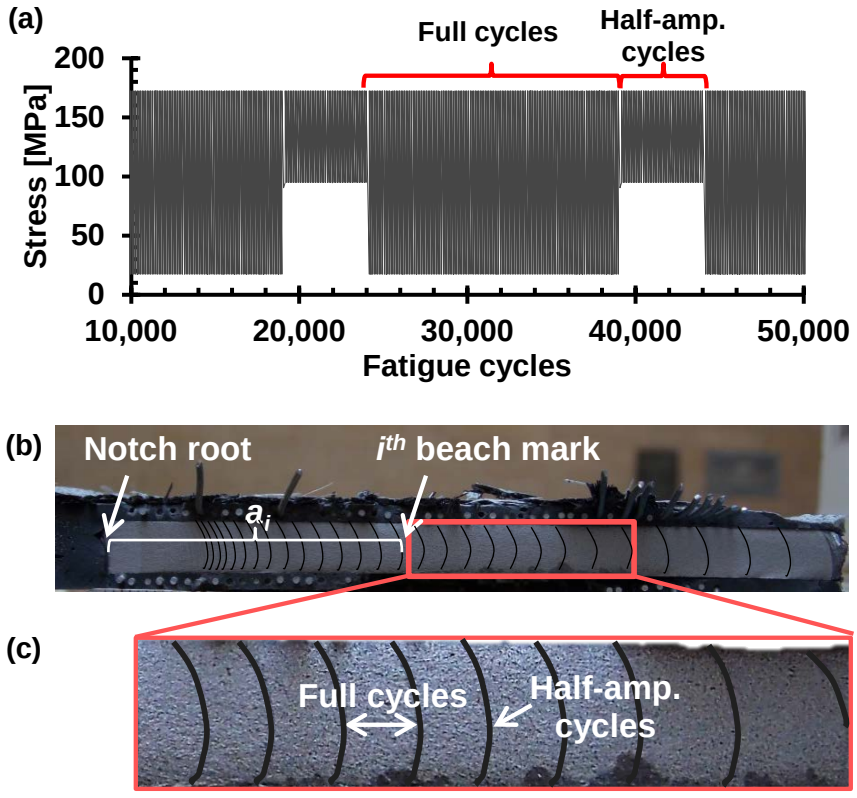

Figure 3.5 The beach marking (beach marks digitally enhanced for clarity)

3.3 Failure modes

All of the coupons experienced abrupt failures due to the rupture of the steel when the crack reached a critical length after a certain number of loading cycles. At this stage, the reinforcement attached to the surface of the steel either fractured in the plane of the crack or debonded from the substrate. Figure 3.6 shows the failure of the coupons with different reinforcing configurations. Both debonding and fracture of the CFRP reinforcement were observed among the CFRP patched coupons after failure as shown in Figure 3.6 (a). Figure 3.6 (b) shows the typical failure of the SMA-reinforced coupons. The SMA wires pulled-out of the matrix. No fractured wires were observed. The CFRP tabs remained bonded to the steel after failure.

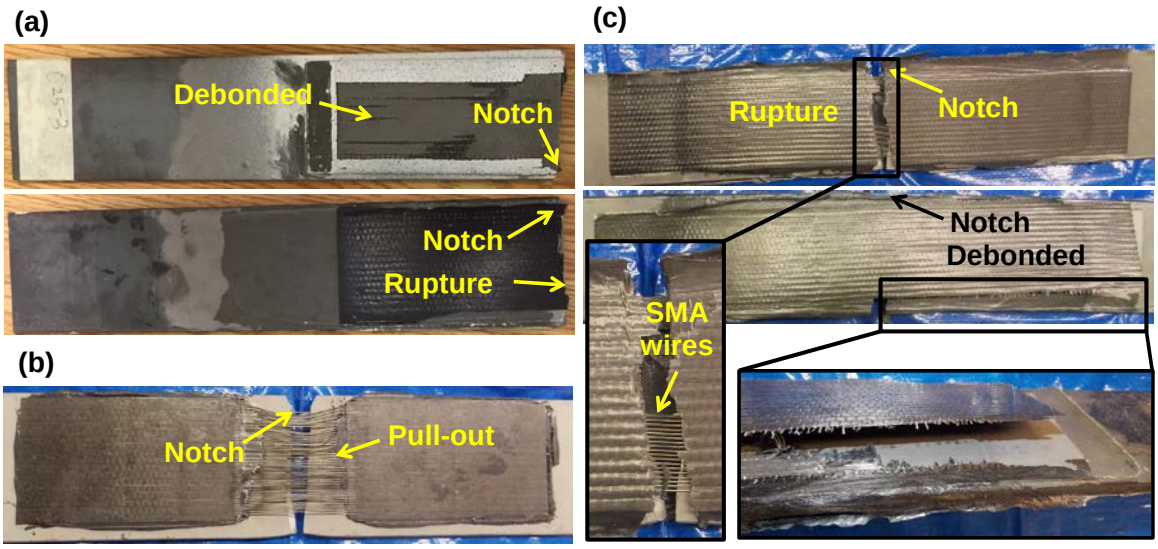

Figure 3.6. Final failure of the specimens: a) CFRP; b) SMA; c) SMA/CFRP

Figure 3.6 (c) shows the failure of the SMA/FRP-reinforced coupons. Both fracture and total debonding of the reinforcement were observed upon failure. For the specimens that exhibited fracture of the reinforcement, the CFRP fractured while the embedded SMA wires remained mostly intact, although a few wires fractured. For all

individual specimens, the failure of the reinforcements on two sides of the coupon could be the same (both fracture or both debonding) or different (one fracture and one debonding). However, fracture and debonding were mutually exclusive on one side.

3.4 Debonding of the reinforcing patch during fatigue loading

During the fatigue loading, the crack in the steel initiated from the root of the edge notch and propagated towards the far edge of the steel plate. An infrared thermal scanner with a precision of 0.1˚C was used to monitor the temperature change of the SMA and SMA/FRP patches during the fatigue loading. The temperature change on the surface of the patches was limited to 2^{o}C, which was consistent with the noise floor of the system.

The DIC system was used to measure the longitudinal strain profiles on the surface of the CFRP overlay during the fatigue loading. Figure 3.7(a) illustrates the measurement technique of the DIC system. The surface of the specimen was painted with stochastic black speckles on a white background before testing. During testing the two 12 megapixel cameras of the DIC system simultaneously took gray scale pictures of the specimen at fixed time intervals (Gom mbH, 2007). In these pictures, each pixel is related to a number in gray scale (i.e. 0 indicates white, 255 indicates black). A matrix of the pixels, which is called a facet, can be identified by its unique gray scale matrix. As shown in the figure, Facet #1 is mathematically different from Facet #2. In this way the position of a facet can be traced in subsequent pictures. By measuring the 3-D coordinates of the centers of facets, a displacement field of the specimen with respect to the reference picture (stage 0) which was taken before loading is obtained.

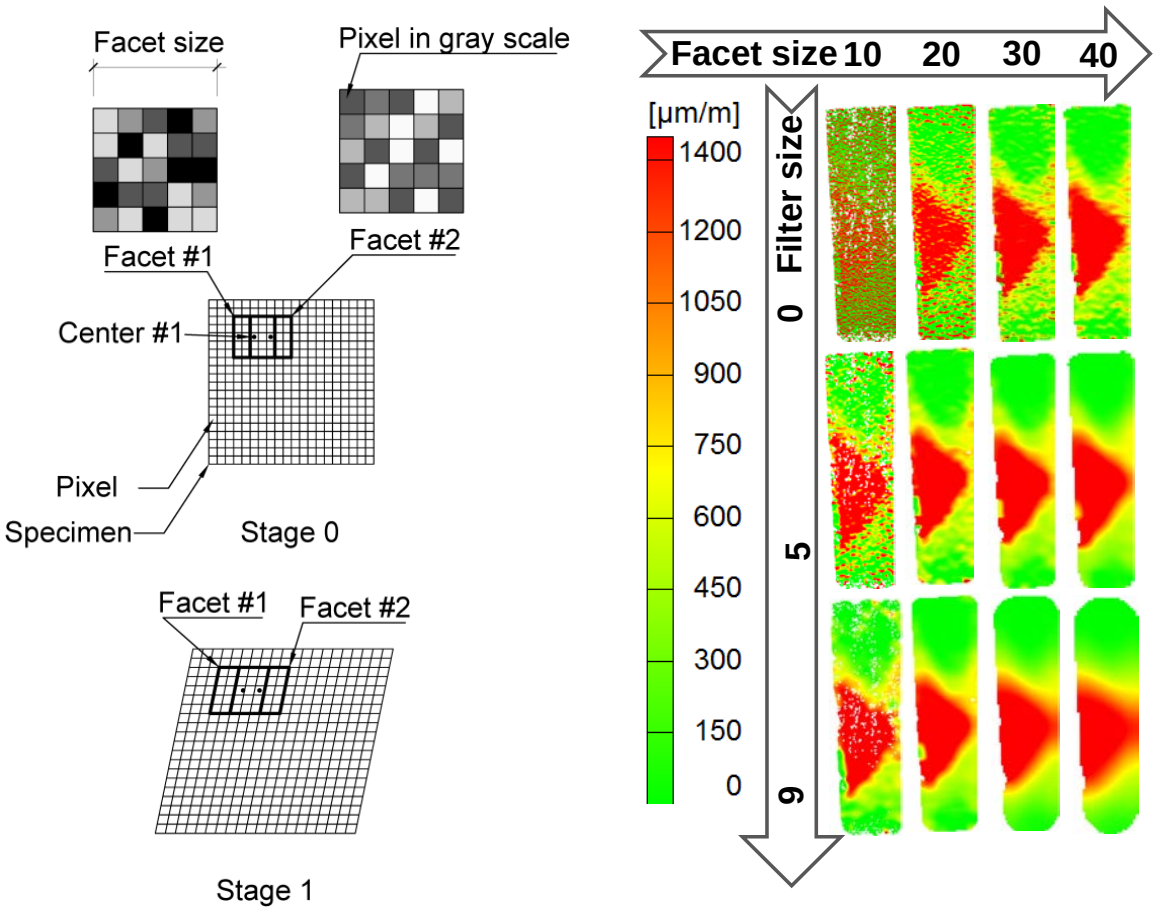

Figure 3.7 (a) Illustration of DIC system; (b) DIC system parameters determination

The calculation of the strains during post-processing of the captured images depends on five parameters: facet size, facet step, computation size, filter size, and filter step. The facet size indicates the number of pixels used to define a single facet. The facet step (the distance between facets) is recommended by the manufacturer to be 80% of the facet size. In this research the computation size (the number of facets used to calculate the strain at a point), was taken as its minimum allowable value, three, to maximize the accuracy of identifying the debonded region. Using a larger computation size results in more smoothed, and less precise strains. To plot contours of results, this data is further filtered (smoothed) by the software. The degree of smoothing is defined by the filter size

and filter runs. The filter size indicates the number of adjacent data points that are considered in the smoothing while the filter run indicates the number of consecutive times that the filtering operation is applied (taken as 50% of the filter size, rounded up, as recommended by the manufacturer).

In this research the computation size remained constant and equal to three. Of the remaining parameters, two were varied independently (facet size and filter size) and the other two were prescribed as discussed above. Figure 3.7(b) displays the influence of the facet size and filter size, on the longitudinal strain contours. When the facet size is too small, there are void points in the strain profile. When the filter size is too large, the results begin to lose data at the four corners of the image. Inspection of Figure 3.7(b) indicates that regardless of the post-processing parameters selected, the presence of a distinct, approximately triangular, strain concentration is captured and the size and shape of the strain concentration remain consistent. In this research the facet size, facet step, computational size, filter size, and filter runs were taken as 30, 24, 3, 5 and 3, respectively. These parameters resulted in smooth strain contours, while retaining data throughout the field of view.

3.4.1 Near-crack debonding

Using the DIC collected data, two types of debonding, near-crack debonding and plate-end debonding, were observed while the crack was propagating underneath the reinforcing patches. Figure 3.8 displays the longitudinal strain contours on the CFRP surface that were obtained from specimen CFRP-155-3 using the DIC system at different stages during the fatigue loading. The figure indicates the number of loading cycles, the crack length, and the instantaneous load at which each of the images was recorded. The

length of the fatigue crack at each stage was determined from the beach marks and the crack location is superimposed on the strain contours for clarity.

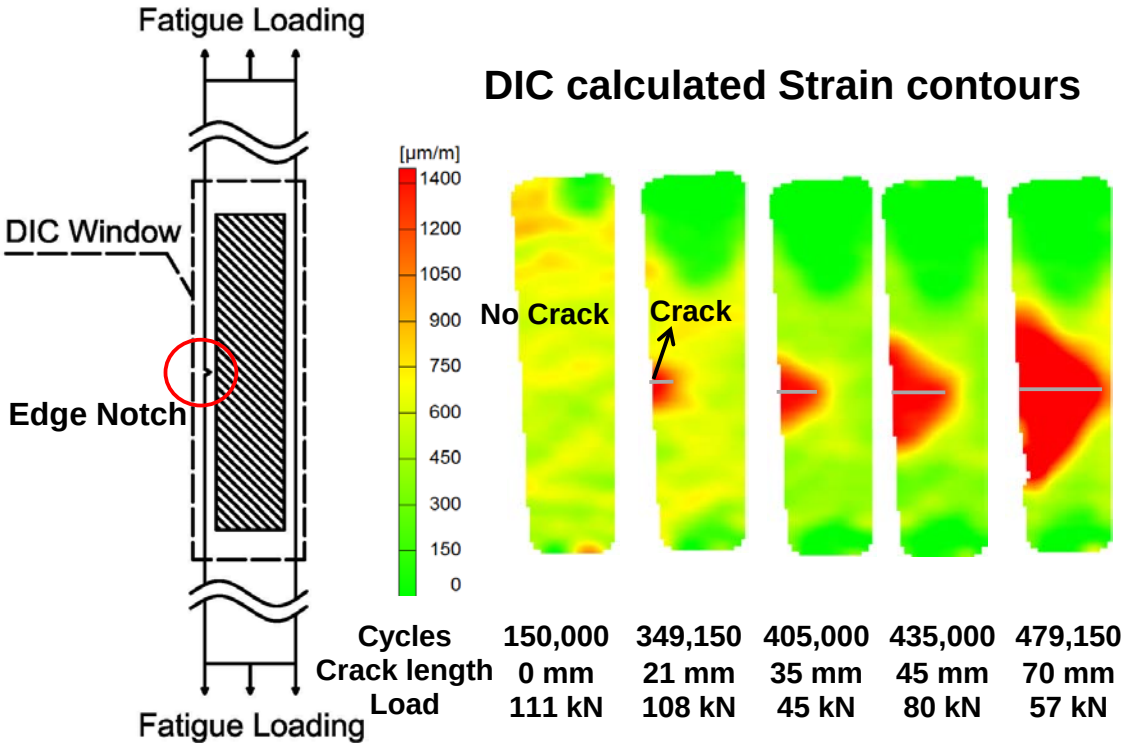

Figure 3.8 Surface strain profile of CFRP patched specimen at different numbers of load cycles

No strain concentration was observed in the first contour at 150,000 fatigue cycles since the crack had not propagated underneath the CFRP overlay. After 349,150 cycles the strain concentration around the crack indicates the presence of a debonded region that extended from the crack tip to the edge of the CFRP patch towards the edge of the plate where the crack mouth was located. The shape of the debonded region was initially semi-elliptical but evolved into an approximately triangular shape as the crack propagated. The coupon failed by rupture after 488,250 cycles with a final crack length of 85 mm. Similar patterns and trends of the strain concentrations and the corresponding crack lengths were observed for the other coupons with CFRP overlays. Figure 3.9 shows the longitudinal

strain contours during fatigue loading of specimen CFRP-155-2 on the side where CFRP ruptured at failure. The size of the strain concentration near the left edge of the specimen became progressively larger as the fatigue loading continued, as shown in the figure, indicating the propagation of debonding prior to ultimate failure by fracture of the steel plate and rupture of the CFRP patch. Examining Figure 3.8 and Figure 3.9 indicates that the CFRP overlays exhibit similar near-crack debonding during fatigue loading regardless of the final failure modes of the CFRP.

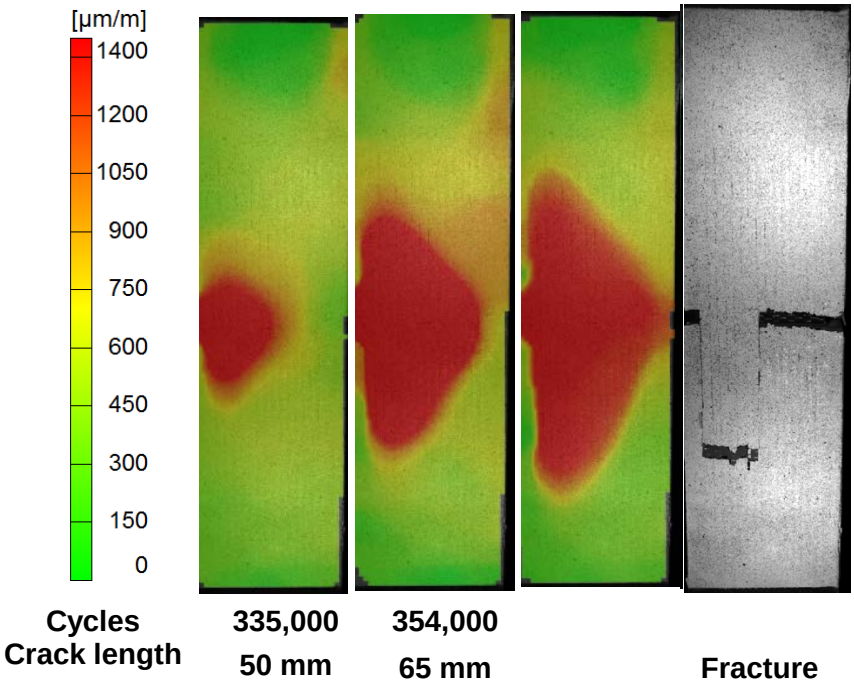

Figure 3.9 Crack-induced debonding of the specimen before final CFRP rupture

Figure 3.10 displays the 3-D surface plot of the gradient of the longitudinal surface strains ($\partial\varepsilon_{xx}/\partial x$ in the figure) calculated from the strain data obtained from the DIC system at a crack length of 70mm. The size and shape of the debonded region of the patches was determined from the DIC measurements by considering this strain gradient. Since the strain gradient is proportional to the adhesive shear stress (τ_{xz} in the figure), a

contour of high strain gradient corresponds to the debonding front where adhesive shear stresses are high. The strain gradient in the debonded region that is bounded by this contour is negligible since there is no transfer of shear stress in the debonded region. Considering the noise floor of the DIC measurements, a strain gradient less than 0.002 μm/m/m enclosed by the high strain gradient contour was taken to indicate debonding.

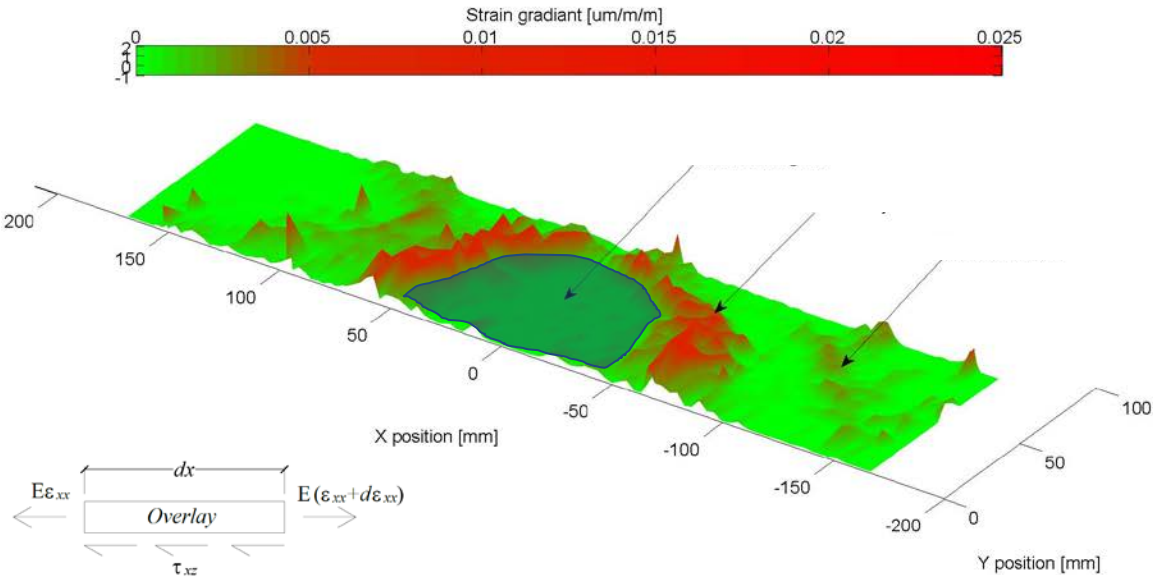

Figure 3.10 Definition and calculation of the debonded area from the DIC results

The calculated debonded area at crack lengths of 21, 35, 45 and 70 mm are 2, 286, 577 and 1564 mm^2 respectively. Previous studies regarding the use of DIC system indicated that the displacement data obtained by the DIC system were close with those measured by conventional LVDT (Beizaee et al., 2016). However, it was found that the DIC system exhibited inconsistencies on measuring of brittle materials (Mohammadipour et al., 2013). Turner (2014) proposed a peridynamics-based algorithm to circumvent the challenges of using DIC on discontinuities such as fracture and fragmentation. In the regions where DIC is accurate and effective, the traditional approach determines the

displacement. While in discontinuous regions, the displacement field is solved for using peridynamics. By doing so, the full-field displacement can be achieved.

The experimental observations in this research suggest that the fatigue loading does not impact the debonding directly. Rather, fatigue loading causes propagation of the crack in the steel and the increase of the crack length drives the propagation of the debonded region. Therefore, the size and shape of the debonded region at any stage during the fatigue loading can be determined based on the maximum fatigue load and the crack length at that stage. This is consistent with previous findings that debonding between the CFRP and steel due to the influence of fatigue loading is minimal compared to the static load induced debonding (Wu et al., 2013).

3.4.2 Plate-end debonding

Figure 3.11 illustrates the plate-end debonding of a coupon that was reinforced with a CFRP overlay. The picture to the left of the figure indicates the monitoring window of the DIC system with respect to the coupon. Following are six longitudinal strain contours on the surface of the coupon that were obtained from the DIC at different stages during the fatigue loading. The number of cycles at which each contour was captured is indicated below each contour. During the fatigue loading, the initiation of debonding of the CFRP from the steel at one end of the plate was observed through visual inspection before reaching 2,000 load cycles. The front of the debonded region was capture when it propagated into the monitoring window, as shown in the third contour in Figure 3.11.

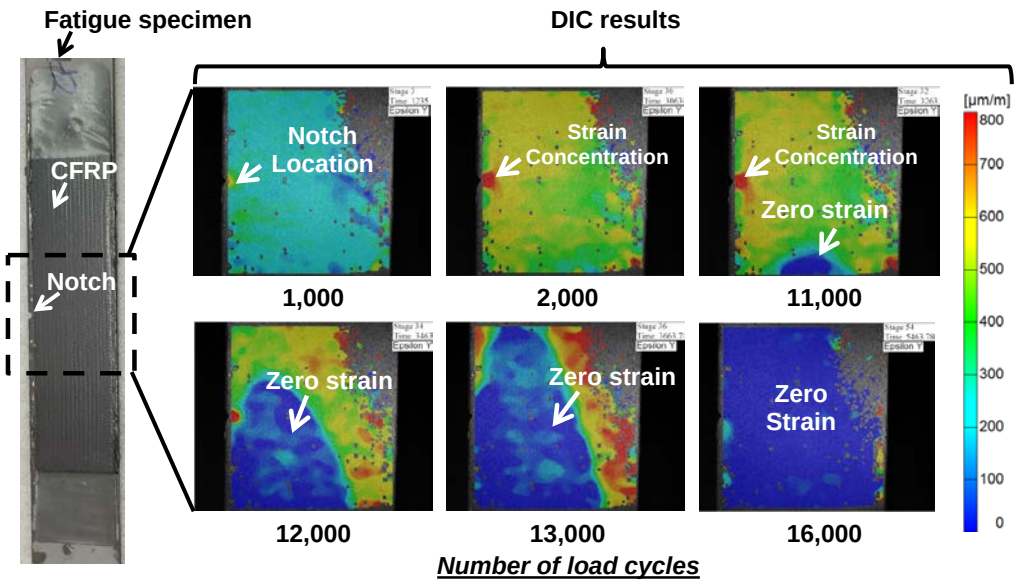

Figure 3.11. Illustration of plate-end debonding using the DIC results

The region of zero-longitudinal-strain indicates that the patch had debonded from the steel. In the subsequent contours the debonded region advanced towards the plane of the crack and eventually completely passed the crack plane by 16,000 load cycles. This type of debonding undermines the fatigue life improvement that can be achieved by the reinforcing patch. The plate-end debonding was largely attributed to the pealing stress at the plate-end. Higher applied maximum fatigue load was more likely to induce this type of debonding. The initiation of plate-end debonding was typically observed to occur when the crack length approached 10 mm. Since the activated SMA wires counteracted the crack opening, this may have delayed or prevented the plate-end debonding. Therefore, plate-end debonding was only observed for coupons that were reinforced with CFRP only and tested at the 217 MPa stress range.

3.4 Fatigue life results

Figure 3.12 plots the measured fatigue lives of the tested coupons against the far-field stress range and Table 3.2 summarizes the fatigue lives of all the tested coupons.

The fatigue lives for AASHTO fatigue categories B', C, D and E (AASHTO, 2012) are also indicated in the figure for comparison. The unpatched control coupons had fatigue lives that fell below those of AASHTO fatigue category E. Installation of the CFRP patch increased the average fatigue life of the coupon to 3.0 times that of the control coupons at a stress range of 217 MPa, and 8.7 times that of the control coupons at a stress ranges of 155 MPa. CFRP patched specimens that were tested at a stress range of 93 MPa exhibited fatigue lives of more than 2 million cycles without any appreciable crack propagation. Thus, the CFRP patch was able to upgrade the life of fatigue detail from below that of AASHTO category E to that of category C at 93 and 155 MPa stress ranges. At the 217 MPa stress range, the CFRP patches upgraded the life of the fatigue detail to that of category D for the specimen without plate-end debonding, while plate-end debonding undermined the fatigue life extension that could be achieved for the other two coupons.

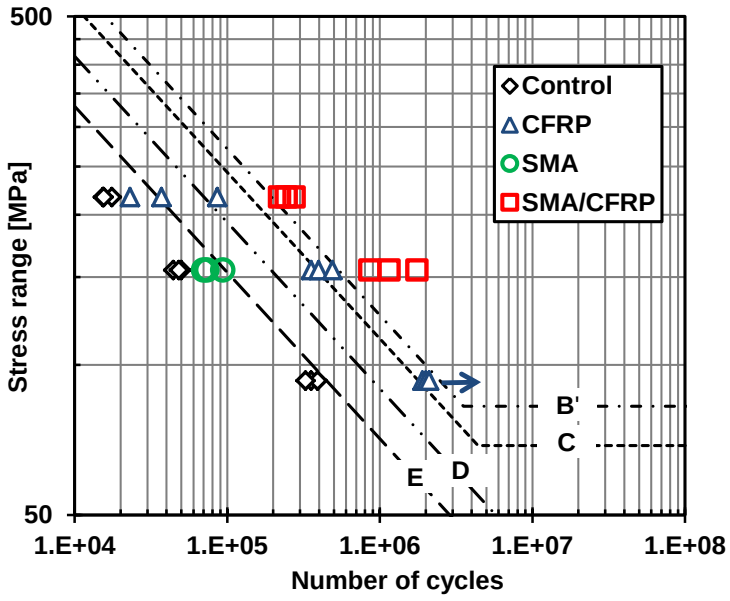

Figure 3.12. Stress range - fatigue live of the tested coupons

Table 3.2 Fatigue lives of tested coupons

Stress range [MPa]	Steel	CFRP	SMA	SMA/CFRP
93	354,542	2,000,000[a]	N/A	N/A
	390,947	2,000,000[a]	N/A	N/A
	326,101	2,000,000[a]	N/A	N/A
155	44,265	354,000	93,458	862,284
	49,868	396,000	73,495	1,151,907
	48,171	488,250	69,918	1,749,704
217	17,500	23,000	N/A	220,000
	15,297	37,000	N/A	274,846
	15,500	86,000	N/A	243,463

[a]fatigue testing runout after 2,000,000 cycles

The coupons that were patched with prestressed SMA patches exhibited an average fatigue life that was 1.7 times that of the control group at a stress range of 155 MPa. This reinforcement did not increase the fatigue life sufficiently to upgrade the detail to beyond AASHTO category E. The coupons that were patched with SMA/FRP patches exhibited average fatigue lives that were 15.3 times and 26.4 times those of the unpatched coupons for stress ranges of 217 MPa and 155 MPa, respectively. Since the coupons that were patched with CFRP only exhibited infinite fatigue life at 93 MPa stress ranges, it is expected that the SMA/CFRP configuration can perform at least as well. This corresponds to upgrading the fatigue detail from below AASHTO category E to above category B' for stress ranges from 93 to 217 MPa.

3.4.1 Material constants

In order to quantify the stress intensity factor in the steel at different crack lengths to understand the influence of the reinforcing system, the material constants in the Elber's equation were calibrated using the test data from the control coupons (Colombi et al., 2015). Algebra of Eq. (2.17) gives:

$$\log\frac{da}{dN} = \log C + m\log U + m\log(\Delta K), \tag{3.1}$$

where C and m are material parameters that need to be determined experimentally. U was determined using load ratio, R, as shown in Figure 2.11. The crack growth rate was determined from the crack length, a, versus elapsed cycles, N, according to ASTM E647 (2013b), in discrete form, as

$$\left(\frac{\Delta a}{\Delta N}\right) = \frac{a_{i+1} - a_i}{N_{i+1} - N_i}. \tag{3.2}$$

Figure 3.13(a) shows the crack growth curves for all nine of the coupons in the control group. The three groups of curves in the figure indicate the three stress ranges that were considered in the testing. Each pair of consecutive data point in the figure was used to calculate one value of the crack growth rate, $\Delta a/\Delta N$. The corresponding values of ΔK for single edge-notched plates of finite width, b, with crack length, a, were calculated as (Tada et al., 2000):

$$\Delta K = F\Delta\sigma\sqrt{\pi(a+c)} \text{ and} \tag{3.3}$$

$$F = \sqrt{\frac{2b}{\pi(a+c)}\tan\frac{\pi(a+c)}{2b}} \cdot \frac{0.752 + 2.02((a+c)/b) + 0.37(1-\sin\frac{\pi(a+c)}{2b})^3}{\cos\frac{\pi(a+c)}{2b}}, \tag{3.4}$$

where c is the notch depth. Since the computed crack growth rate is an average rate over the a_{i+1} - a_i increment, the average crack length (a_{i+1} + a_i)/2 was used to calculate ΔK. A total of 108 data points were gathered from the experimental results and plotted in Figure 3.13(b), the least squares method was used to calibrate the material parameters. The calibrated material parameters C and m are 3.38×10^{-14} and 3.29 respectively.

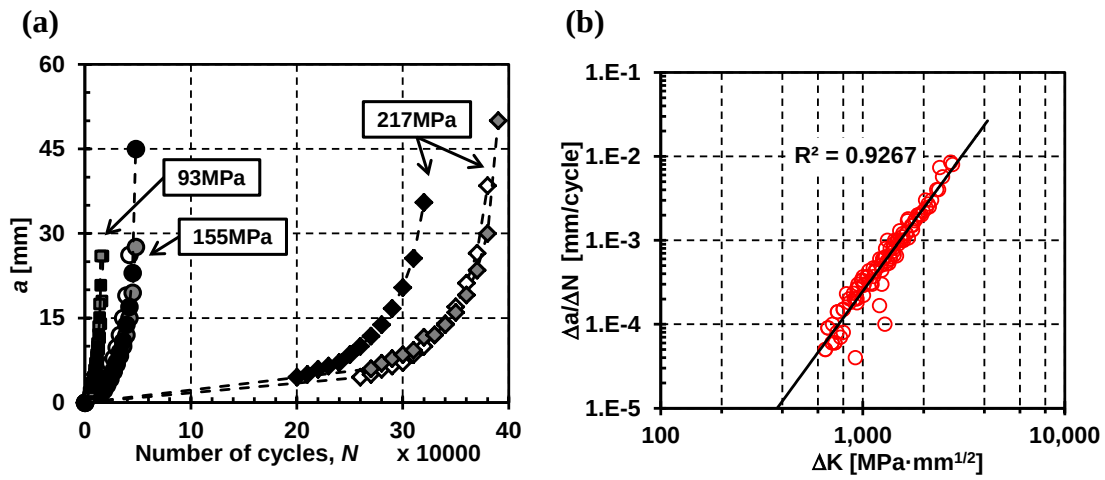

Figure 3.13. Experimental data of control coupons: (a) Crack growth curves; (b) crack growth rate vs. *ΔK*

3.4.2 Fatigue strengthening using CFRP

The CFRP overlay extended the fatigue life of the single edge-notched specimen by decreasing the stress range at the notch root or at the crack tip. The axial stiffness of the CFRP patches is 14% of the total stiffness of the patched plate. As a result, installing the CFRP patches decreased the stress range in the steel by 14% while the stress ratio was not changed. The reduced stress range and corresponding stress intensity factor range resulted in slower crack initiation and crack growth rate, which resulted in a longer fatigue life. Figure 3.14(a) and (b) show the crack growth curves for the CFRP patched coupons loaded at 217 and 155 MPa stress ranges, respectively, compared to the control coupons. The CFRP-patched coupons that were loaded at 93 MPa stress range are not presented since no appreciable crack propagation was observed during the fatigue loading. The scatter of the fatigue lives of the CFRP group of coupons that were tested at 217 MPa (shown in Figure 3.14 (a)) is due to the plate-end debonding of the CFRP reinforcement during the fatigue loading.

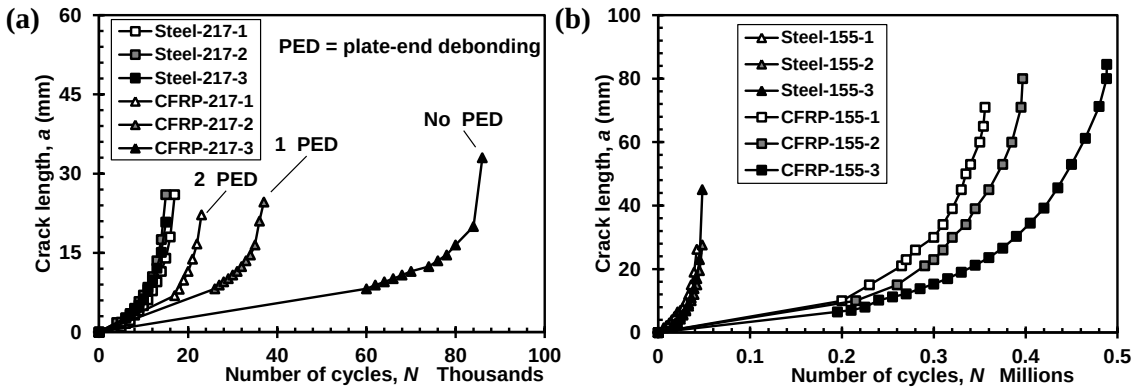

Figure 3.14. Crack growth curves of steel and CFRP groups: a) 217 MPa, b) 155 MPa

CFRP-217-1 exhibited plate-end debonding on both sides resulting in a fatigue life of 23,000. CFRP-217-2 exhibited plate-end debonding on one side resulting in a fatigue life of 37,000. CFRP-217-3 did not exhibit plate-end debonding resulting in a fatigue life of 86,000. During the fabrication of the coupons, the recognized best practice for surface preparation and bonding was used. Therefore, the relatively high scatter in the fatigue lives and the differences in plate-end debonding reflect the inherent variability and uncertainty associated with the bonded interface. At a stress range of 155 MPa (shown in Figure 3.14 (b)), none of the CFRP patched coupons exhibited plate-end debonding resulting in relatively more consistent fatigue life results. The slight scatter was due to the inherent variability of the specimens.

The crack growth rates, $\Delta a/\Delta N$, at different crack lengths were obtained from the crack growth curve. With the material parameters, C and m, calibrated from the control group, the corresponding values of ΔK were evaluated. Figure 3.15(a) and (b) plot the ΔK versus crack lengths for control and CFRP patched coupons that were tested at a 217 MPa and 155 MPa stress ranges, respectively. Best fit lines were generated for each group to facilitate comparison. It can be seen that the CFRP patches decreased the stress

intensity factor for a given crack length compared to the unpatched coupons. In the meantime, due to the decreased stress intensity factor at a given crack length, the crack was able to propagate further before reaching the fracture toughness of the steel. With slower growth rate and longer critical crack length, the average fatigue lives of the steel elements were increased to 3.0 and 8.7 times those of the un-patched control coupons at 217 and 155 MPa stress ranges, respectively.

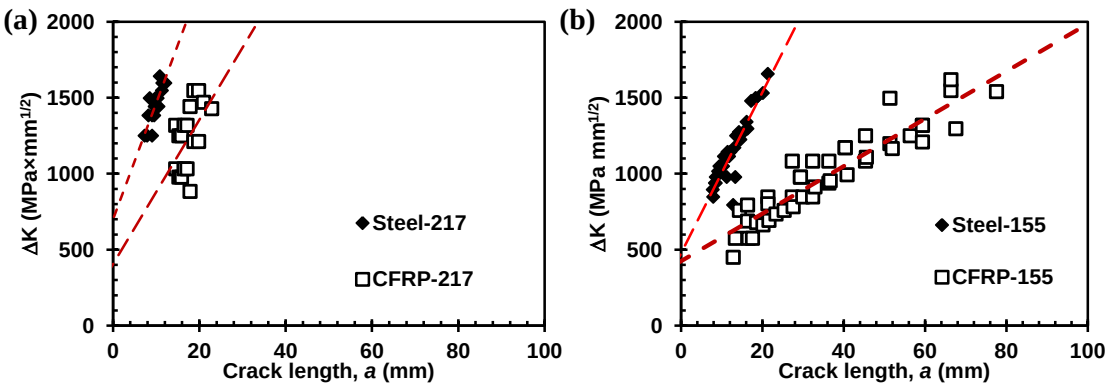

Figure 3.15. *ΔK* at difference crack lengths of Steel and CFRP groups: (a) 217 MPa; (b) 155 MPa

3.4.2 Fatigue strengthening using prestressed SMA wires

The prestressed SMA patch extended the fatigue life of the single edge-notched specimen primarily by reducing the stress ratio, which eventually reduced the effective stress intensity factor range at the crack tip. The modulus of the activated SMA wire was 70 GPa (data from the wire test). The axial stiffness, *EA*, of the SMA wires is less than 2% of the stiffness of the steel substrate. As a result the stress range reduction induced by the SMA wires was minimal. However, the prestressed SMA wires applied compressive stresses to the steel, which reduced the stress ratio from 0.1 to nearly 0. Figure 3.16 compares the crack growth curves of the control coupons and the SMA patched coupons that were tested at a stress range of 155 MPa. No plate-end debonding was observed for

this group of specimens. The scatter in SMA-155 group was due to the variability of the specimens.

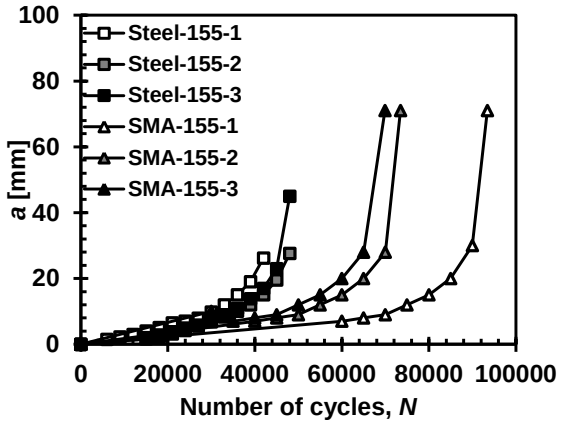

Figure 3.16. Crack growth curves of Steel and SMA groups

This group of specimens was designed to study the effect of the prestressing force induced by the SMA wires exclusively of the presence of the CFRP overlay bridging the crack to evaluate whether the combined effect of the SMA/CFRP patch was equivalent to the simple sum of the components or if there was a synergistic effect between the components. The test results indicate that reducing the stress ratio at the crack through prestressing forces induced by the activated SMA wires provides only a moderate improvement in the fatigue life. This is attributed to the fact that the relatively small axial stiffness of the SMA-only patches does not significantly reduce the stress range near the crack or provide any appreciable crack-bridging effect.

3.4.3 Fatigue strengthening using SMA/CFRP composite system

Figure 3.17 (a) and (b) compare the crack growth curves between the coupons of SMA/CFRP and CFRP groups that were tested at 217 MPa and 155 MPa stress ranges, respectively. None of the SMA/CFRP coupons exhibited plate-end debonding. The

SMA/CFRP patches substantially increased the fatigue lives of the coupons relative to the CFRP-reinforced specimens.

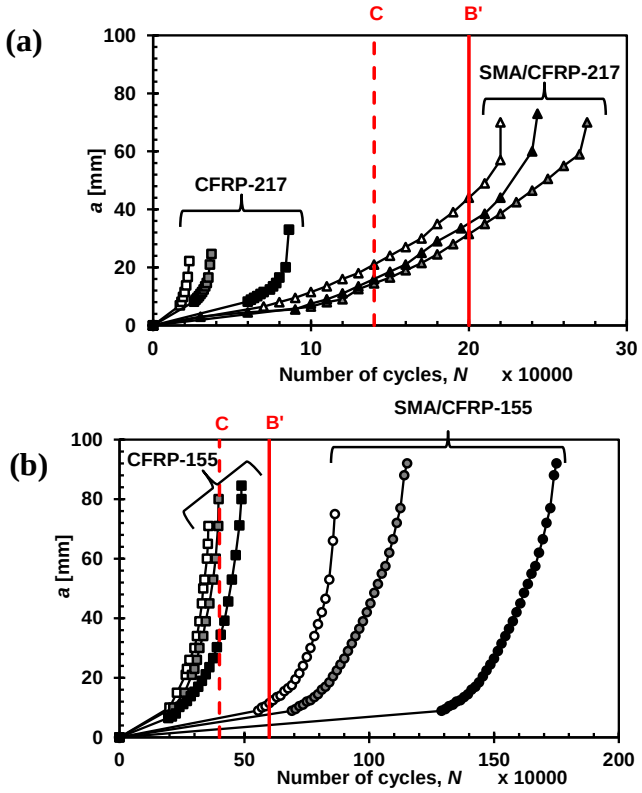

Figure 3.17. Comparison between CFRP and SMA/CFRP groups

The coupons reinforced only with CFRP exhibited fatigue lives below the AASHTO fatigue category C limit. In Figure 3.17 (b), the scatter of the fatigue life for the SMA/CFRP coupons was due to the combination of the inter-specimen variability and differences in the recovery forces generated by the SMA wires. However, the coupon with the lowest fatigue life still exceeded the AASHTO category B' limit.

Figure 3.18 shows the ΔK values for the coupons that were patched with CFRP and SMA/CFRP patches at different crack lengths. The SMA/CFRP patches decreased the stress intensity factor at a given crack length even more than the CFRP patches. With slower growth rates the average fatigue lives of the coupons were increased to 15.3 and

26.4 times those of the control coupons at stress ranges of 217 and 155 MPa, respectively using the SMA/CFRP patches.

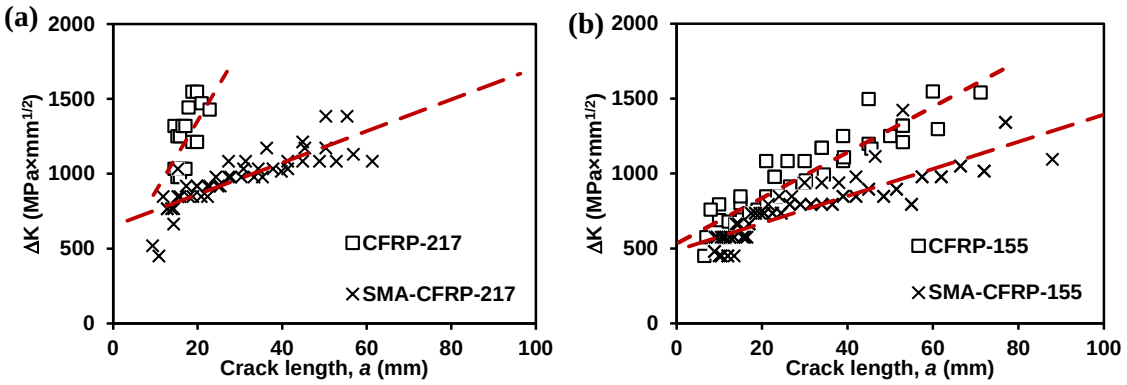

Figure 3.18. *ΔK* at difference crack lengths of CFRP and SMA/CFRP groups

It should be noted that the stress intensity factor based models are phenomenological models that provide no physical insight regarding processes occurring during crack propagation. Other models have been proposed to relate the fatigue crack growth rate with the plastic zone size ahead of the crack tip. The estimation of the plastic zone size were estimated by several studies (Irwin, 1957; Edmunds and Willis, 1977). The size of the plastic zone depends on parameters such as yield stress of the material, thickness of the specimen, and applied loading conditions (Wang, 1993). Recent research work has experimentally demonstrated the correlation between the plastic zone size and the fatigue crack propagation rate and believed that the plastic zone size was an better parameter than any other previously proposed LEFM and elasto-plastic fracture mechanics (EPFM) (Chikh et al., 2008).

3.5 Summary and discussion

This chapter summarizes the experimental program that quantifies the effectiveness of the newly-developed thermally-activated SMA/CFRP patch for

extending the fatigue lives of fatigue-sensitive steel details. The approach exploits the unique thermomechanical properties of SMA wires to apply compressive stress to the steel members. Four groups of single edge notched coupons were reinforced with different reinforcement configurations and tested under tension-tension fatigue loading up to failure at three different stress ranges. The results showed that the thermally-activated SMA/CFRP composite patch increased the average fatigue lives of the edge-notched steel plates to 26.7 and 15.3 times those of the un-patched plates at 155 MPa and 217 MPa stress ranges respectively. This improvement was equivalent to upgrading the fatigue detail form less than an AASHTO category E detail to better than a category B' detail. In comparison, the specimens that were patched only with CFRP had average fatigue lives that were 3 and 8.7 times those of the unpatched samples at stress ranges of 155 and 217 MPa, respectively. The prestressed SMA wires alone prolonged the average fatigue life to 1.7 times that of the unpatched coupons at a stress range of 155 MPa. This indicates that the thermally-activated patching system is more effective than the simple sum of the reinforcing effects of the CFRP and the prestressed SMA wires. It is evident that there is a synergistic effect between the CFRP and prestressed SMA wires in strengthening fatigue sensitive steel member. The results suggest that the thermally-activated SMA/CFRP patch is a promising system for improving the lives of fatigue-sensitive metallic elements.

Near-crack debonding was observed for all of the coupons that were patched with CFRP and SMA/CFRP patches during the fatigue loading. This has a negative impact on the fatigue life improvement that can be achieved but is largely unavoidable. The experimental findings in this research suggest that the increase of the crack length rather

than the fatigue loading drives the propagation of the near-crack debonded region. This was used to develop a numerical model, discussed in chapter 4, that was able to predict the near-crack debonding at any stage during fatigue loading based on the applied maximum fatigue load and the instantaneous crack length. Plate-end debonding, on the other hand, was only observed for CFRP-217-1 and -2. This implies that the plate-end debonding is likely to occur when the maximum applied stress is relatively high, which is 60% of the yielding stress in this research. The fatigue life of the coupons reinforced with CFRP overlays were decreased by 57% and 73% due to one-side and two-side plate-end debonding.

Chapter 4 : Investigation of the near-crack debonding between FRP overlay and steel under fatigue loading

The existence of debonding in FRP-patched cracked metallic elements was observed in the experimental data in Chapter 3 and multiple previous studies. However, the mechanism of the initiation and propagation of the debonding still remains unidentified. This chapter highlights the importance of accurately predicting the size and shape of the debonded region in accurately predicting the fatigue crack growth and fatigue life. It also presents a numerical modeling approach that can be used to predict the size and shape of the debonded region in cracked steel elements that are repaired using externally bonded FRP patches. The model is validated by comparison to experimental results and DIC based measurements. The validated model is used to conduct a parametric study to investigate the influence of different parameters on the predicted stress intensity factors and crack growth rates in patched cracked steel elements.

4.1 Influence of debonding on the crack growth prediction

A 3-D FE model was developed using the commercial finite element package Abaqus v. 6.12 (Dassault Systèmes Simulia Corp., 2012) to predict the mode I SIF, K_I, at the crack tip of a single edge-notched tension coupon that is patched with FRP. Different hypothetical shapes and sizes of debonded regions were considered to illustrate the impact of debonding on the prediction of the stress intensity factor and crack growth rate. Figure 4.1 presents the quarter FE model, consisting of two solid components, the steel substrate and the CFRP patch, and the interface connecting them. The steel and the CFRP were modeled using 3-D, 20-node continuum elements with reduced integration, and

hourglass control. Each model consisted of 16,000 elements and 81,000 nodes. A static pressure boundary condition of 170 MPa was applied at the end of the steel plate to simulate the applied far-field tensile load. The crack face was modeled by applying a free boundary condition as shown in the figure, while a symmetry boundary condition was applied to the rest of the un-cracked segment. The stress singularity at the crack tip was represented using classical 3-D, wedge-shaped crack tip elements, which are collapsed 20-node elements with edge nodes shifted to the 1/4 point along the edges as illustrated in Figure 4.1. Different crack lengths were simulated by varying the length of the region where the free boundary condition was defined.

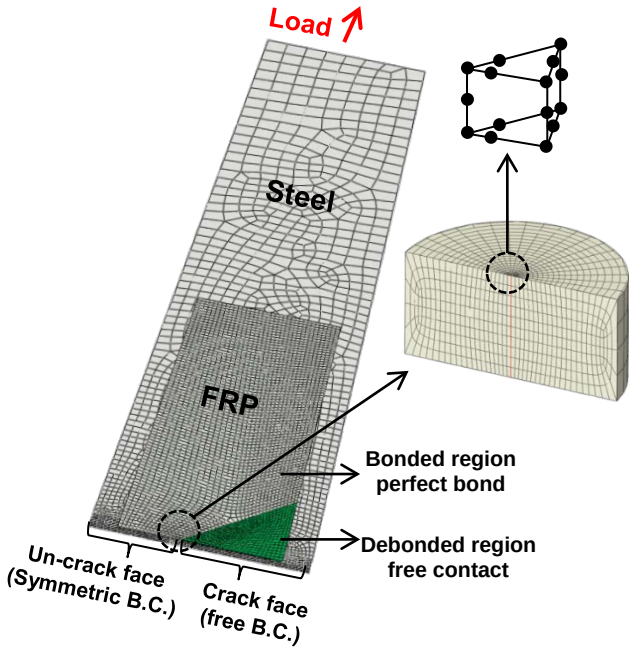

Figure 4.1. Quarter FE model details (adapted from Abaqus software (Dassault Systèmes Simulia Corp., 2012))

The geometries and material properties that were adopted in the model were the same as those used for the tested coupons. The steel plate was totally 914 mm long, 102 mm wide, and 6.4 mm thick; the CFRP patches were each totally 356 mm long, 76 mm

wide, and 1 mm thick centered on the surface of the steel. The steel was modeled as a linear, elastic material with Young's modulus of 200 GPa and Poisson's ratio of 0.3. The CFRP material was modeled as a transverse isotropic material with five independent elastic constants: longitudinal modulus (E_1) of 138 GPa, transverse moduli ($E_2 = E_3$) of 9 GPa, shear moduli in the transverse plane ($G_{12} = G_{13}$) of 4.4 GPa, and Poisson's ratios ($\nu_{12} = \nu_{13}$, and ν_{23}) of 0.3 and 0.3, respectively.

In order to control the size and shape of the debonded region in this first stage of the analysis the debonded region was modeled without any bond between the steel and the CFRP while the remaining portion of the CFRP was assumed to be perfectly bonded to the steel. In this initial study, hypothetical shapes and sizes of the debonded region were considered to highlight the importance of incorporating debonding in the simulations. To that end, three parameters, c, α and h were introduced to describe the geometry of the debonded region as shown in Figure 4.2. The distance between the crack tip and the vertex of the debonded region is defined as c. The angle α defines the extent of the debonded region along the edge of the patch. The parameter h defines the curvature of the parabolic arc of the debonding front. A value of zero results in a triangular debonded region. The crack length is a and the width of the specimen is b. The interfacial traction-separation law was subsequently incorporated into the model as described in the following section of this paper, which provides a means of predicting the size and shape of the debonded region for given crack lengths and patch configurations.

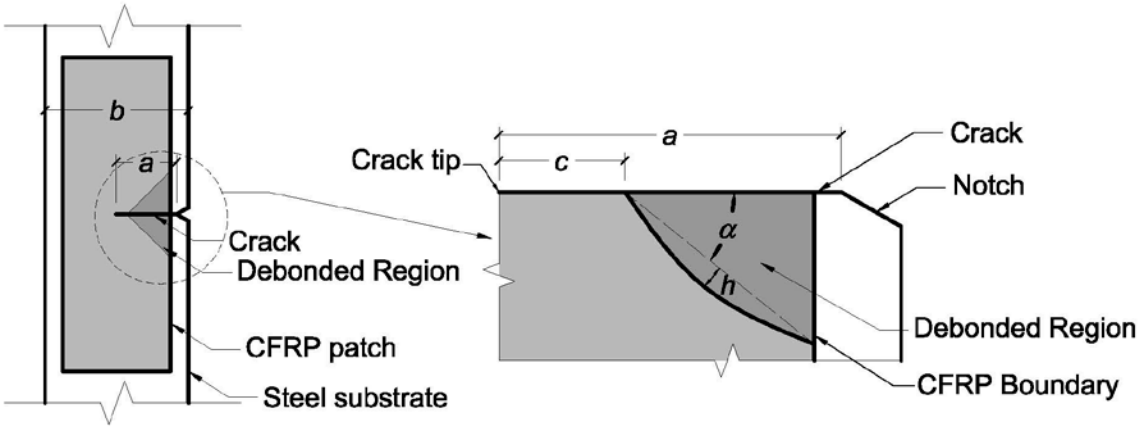

Figure 4.2. The parameters used to define the debonded region

Abaqus calculates the SIF at the crack tip from the J-integral (Rice, 1978) of the tubular surface enclosing the crack tip/line (Dassault Systèmes Simulia Corp., 2012). The SIF at the crack tip was calculated for different shapes and sizes of the debonded region. Crack lengths of 40 mm and 50 mm were considered. The shape and size of the debonded region was changed by varying one of the three parameters c, α and h as summarized in Table 4.1.

Table 4.1 Modelling matrix of influence on SIF at the crack tip

Group	c [mm]	α [˚]	h [mm]
1	20,15,10,0	45	0
2	0	45,35,25,15	0
3	0	45	15,10,5,0

Figure 4.3 shows the debonded regions for constant values of α and h and different values of c. The SIF at the crack tip corresponding to each debonded region were calculated and are plotted in the figure. For both 40 mm and 50 mm crack lengths, the SIF at the cracktip decreases as c increases. Specifically, when c increased from 0 mm to 20 mm, the SIF decreased by 57% (from 2827 MPa$\sqrt{\text{mm}}$ to 1217 MPa$\sqrt{\text{mm}}$) for the 50 mm crack and by 67% (from 2412 MPa$\sqrt{\text{mm}}$ to 807 MPa$\sqrt{\text{mm}}$) for the 40 mm crack.

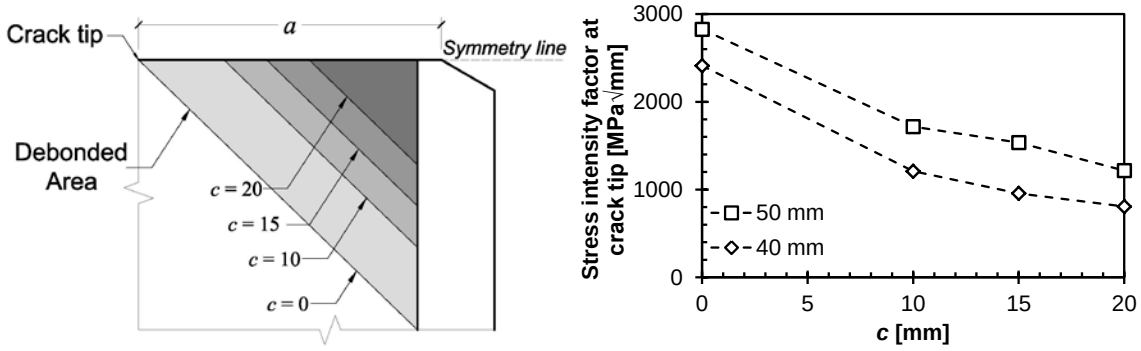

Figure 4.3. SIF values of different values of the parameter *c*

Figure 4.4 plots the SIF at the crack tip for cases when *c* and *h* were both set equal to 0 mm while the angle of inclination of the debonded region, α, was varied from 15˚ to 45˚. It can be seen that the SIF increases linearly as the angle, α, increases. When the angle was equal to 15˚ (debonding localized along the crack), the SIF values for 40 mm and 50 mm crack length were 1340 MPa$\sqrt{\text{mm}}$ and 1372 MPa$\sqrt{\text{mm}}$, respectively. When the angle was increased to 45˚ (debonding extending substantially beyond the crack), the corresponding SIF values were 2412 MPa$\sqrt{\text{mm}}$ and 2827 MPa$\sqrt{\text{mm}}$, representing increases of 80% and 106%, respectively. The influence of the angle on the SIF is more dramatic when the crack is longer. This indicates a similar trend to that of the influence of the parameter *c* that the stress intensity factor is higher when the debonded area is larger.

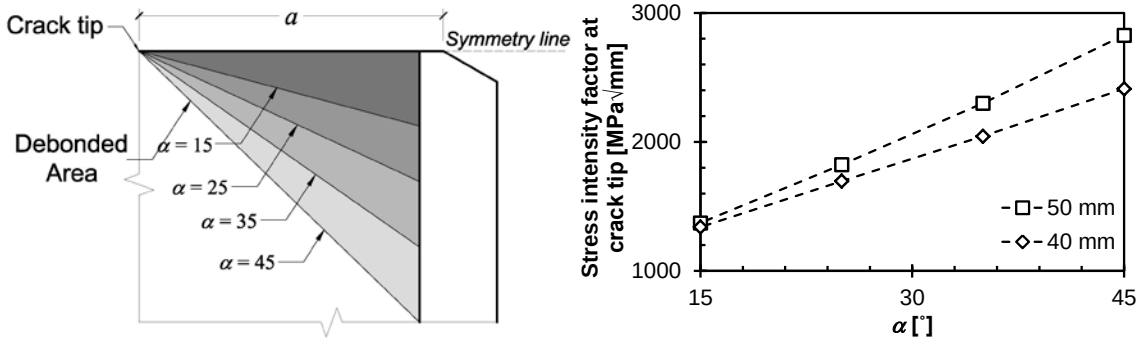

Figure 4.4. SIF values of different angles

Figure 4.5 presents the SIF for cases when c and α were set equal to 0 mm and 45˚ respectively while h was varied from 0 to 15 mm. The value of h defines the shape of the third edge of the debonded region; a higher value of h corresponds to a more curved debonding front and a somewhat larger debonded area. It can be seen in the figure that when h equaled zero (linear debonding front), the SIFs at the crack tip were 2412 MPa√mm and 2827 MPa√mm for crack lengths of 40 mm and 50 mm respectively. When h was increased to 15 mm, the corresponding values of the SIF at the crack tip increased to 3259 MPa√mm and 3959 MPa√mm, representing increases of 35% and 40%, respectively.

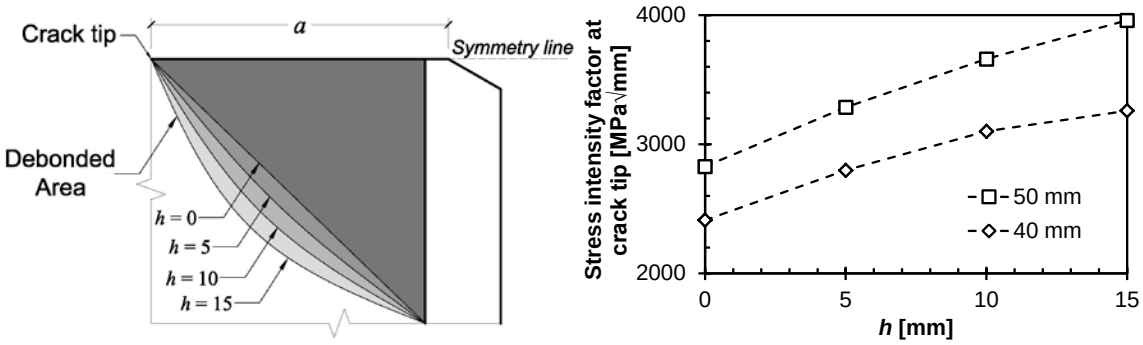

Figure 4.5. SIF values of different curvatures

Figure 4.6 plots the influence of the area of the debonded region on the SIF for all of the analyzed parameter groups. The relationship between them can be reasonably approximated by a linear trend line with slope of 2.74 and 2.18 for crack lengths of 40 mm and 50 mm respectively, although the linear trend provides a better fit for the shorter crack length.

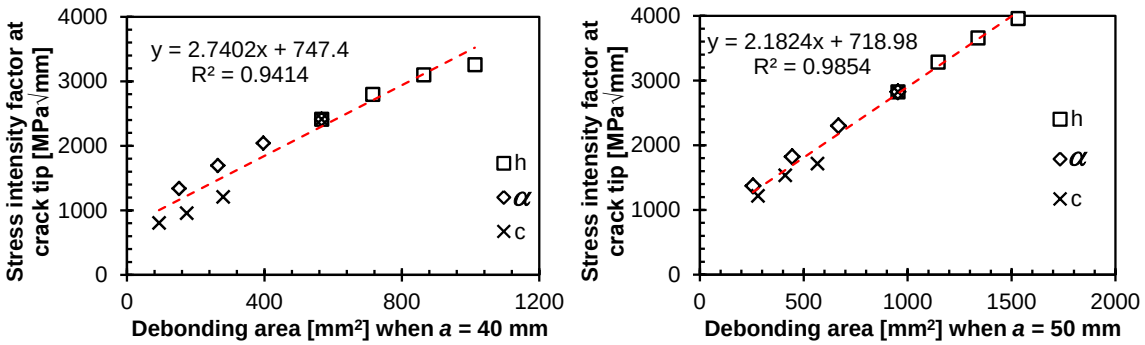

Figure 4.6. SIF values vs. debonded area for different crack lengths

Based on the SIF at the crack tip, the corresponding crack growth rate, *da/dN*, can be predicted using the material parameters *C* and *m*, which were determined to be 3.38×10^{-14} and 3.29, respectively. The influence of the debonding on fatigue behavior prediction can be better understood by plotting crack growth rates as a function of the area of the debonded region in Figure 4.7. The figure indicates that a slight change of the debonded region results in a substantial change of the crack growth rate. For example, as shown in Figure 4.7(b), increasing the size of the debonded region by 6 times increases the predicted instantaneous crack growth rate by 23 times from 1.7×10^{-4} mm/cycle to 3.9×10^{-3} mm/cycle. Similarly, in Figure 4.7(e), a slight change of the shape of the debonded region from a linear debonding front to a parabolic debonding front increases the predicted instantaneous crack growth rate by 162% from 6.1×10^{-3} mm/cycle to 1.6×10^{-2} mm/cycle.

The numerical results indicate that by assuming different shapes and sizes of the debonded region along the crack in the FE model of a single edge-notched tension coupon with bonded CFRP patches, the calculated SIF at the crack tip and the corresponding crack growth rates are substantially different. Therefore assuming the shape and size of the crack-induced debonding when modeling the fatigue behavior of

FRP patched cracked steel elements could lead to substantial inaccuracies in the predictions of fatigue lives.

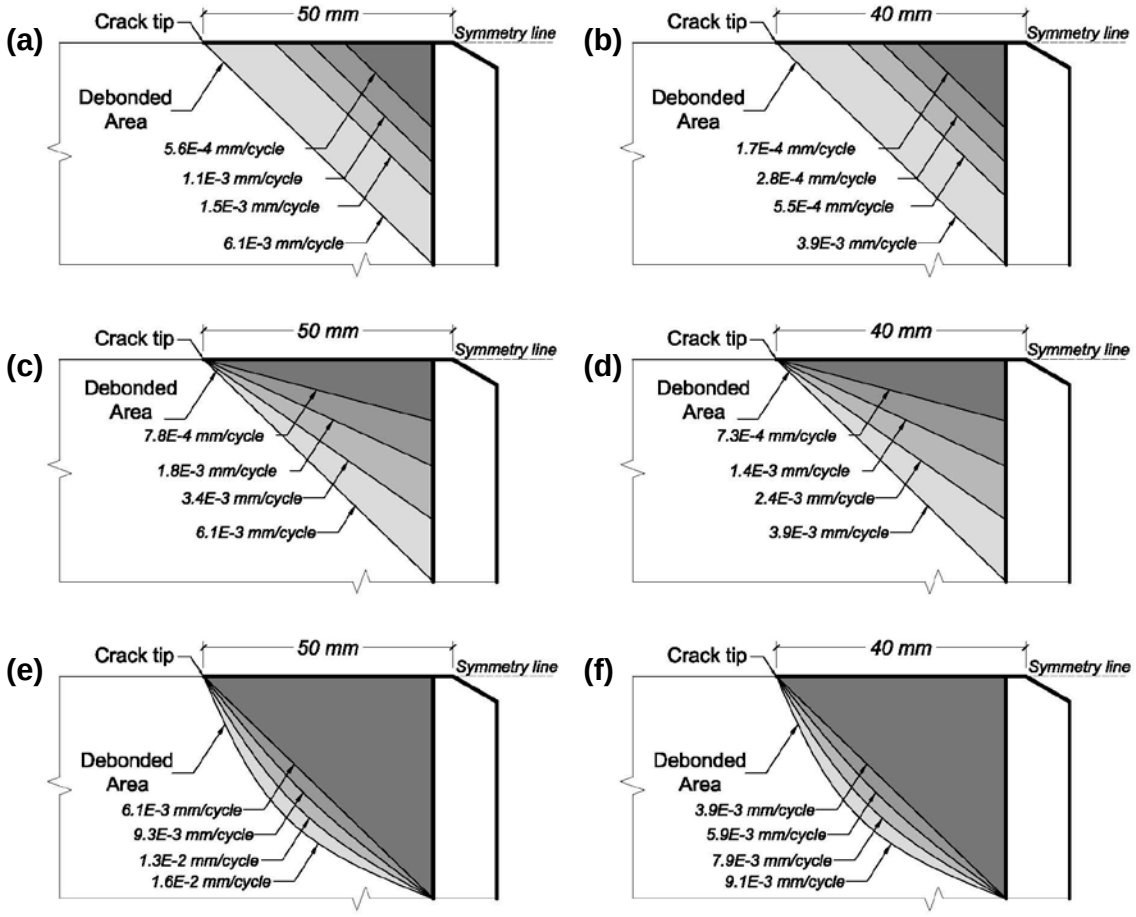

Figure 4.7. Crack growth rate for debonded region

4.2 Prediction of the interfacial debonding

By incorporating an interfacial traction-separation model into the numerical model, it can predict the size and shape of the debonded region for different crack lengths and maximum applied load levels. Figure 4.8 shows the quarter FE model and mesh. Static pressure was applied at the end of the steel plate to simulate the applied far-field tensile load. The applied stress value was 170 MPa, which is the same as the maximum far-field stress applied on the tested specimens.

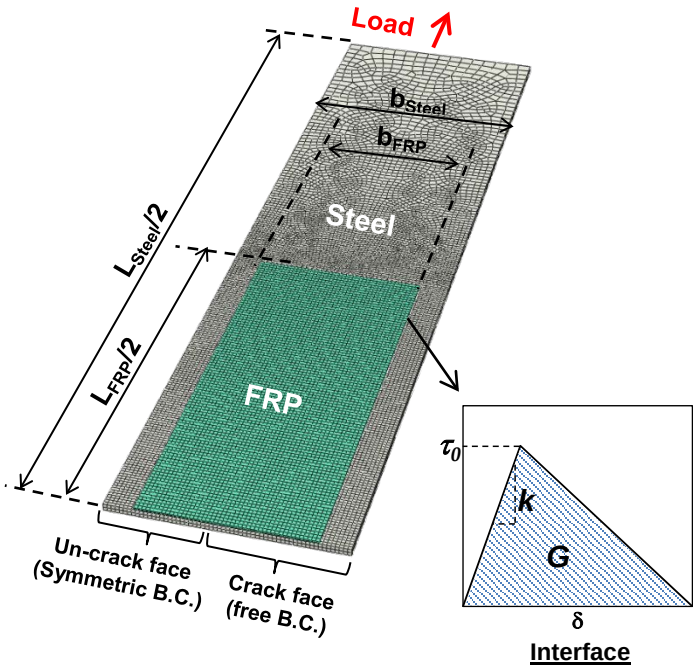

Figure 4.8. Debonding FE model

Figure 4.8 shows the governing traction-separation model of the cohesive zone simulating the CFRP/steel interface (Dassault Systèmes Simulia Corp., 2012). A linear traction-separation/bond-slip behavior was assumed before the initiation of damage at the interface:

$$\begin{Bmatrix} \tau_t \\ \tau_s \\ \sigma_n \end{Bmatrix} = \begin{bmatrix} k_{tt} & & \\ & k_{ss} & \\ & & k_{nn} \end{bmatrix} \begin{Bmatrix} \delta_t \\ \delta_s \\ \delta_n \end{Bmatrix}, \tag{4.1}$$

where τ_t and τ_s are two in-plane shear tractions, and σ_n is the normal traction. The directions denoted by the subscripts *t*, *s* and *n* are indicated in the figure. The corresponding separations are denoted by δ_t, δ_s and δ_n. In this study, only the in-plane tractions and slips were considered since the normal tractions at the interface close to the crack are compressive rather than tensile, and therefore do not induce debonding. This can be observed by analogy to the double-lap shear coupon (Hart-Smith, 1973). The

remaining stiffness components, k_{tt} and k_{ss}, are defined by the traction-separation model. Since the in-plane stiffnesses are taken to be equal, they are denoted simply as *"k"*.

The failure mechanism at the interface consists of a damage initiation criterion and a damage evolution model. Damage is assumed to initiate when the following condition is satisfied

$$\lambda = \left\{\frac{\tau_s}{\tau_0}\right\}^2 + \left\{\frac{\tau_t}{\tau_0}\right\}^2 = 1, \tag{4.2}$$

where λ is the damage parameter, and τ_0 is the interface shear strength. Once the damage initiates, a linear softening law is employed to simulate the damage evolution. The energy release rate, *G*, defines the damage evolution behavior. Fawzia, et al. (2010) and Wu, et al. (2012) determined the values of *k*, τ_0, and *G* for bonded joints that were fabricated using the same adhesive materials and similar installation techniques as those that were used in this study as 600 MPa/mm, 20 MPa and 0.12 N/mm respectively.

Figure 4.9 compares the measured and predicted strain contours on the CFRP surface at different crack lengths. Four longitudinal strain profiles of the CFRP patch during loading are presented with increasing numbers of cycles and crack lengths from left to right. In each profile, the upper portion was obtained using the DIC system while the lower portion was computed using the proposed FE model. The upper strain profiles of the CFRP overlay from left to right were captured after the specimen experienced 349150, 405000, 435000, and 479150 fatigue cycles. The corresponding crack lengths were 21, 35, 45, and 70 mm, respectively.

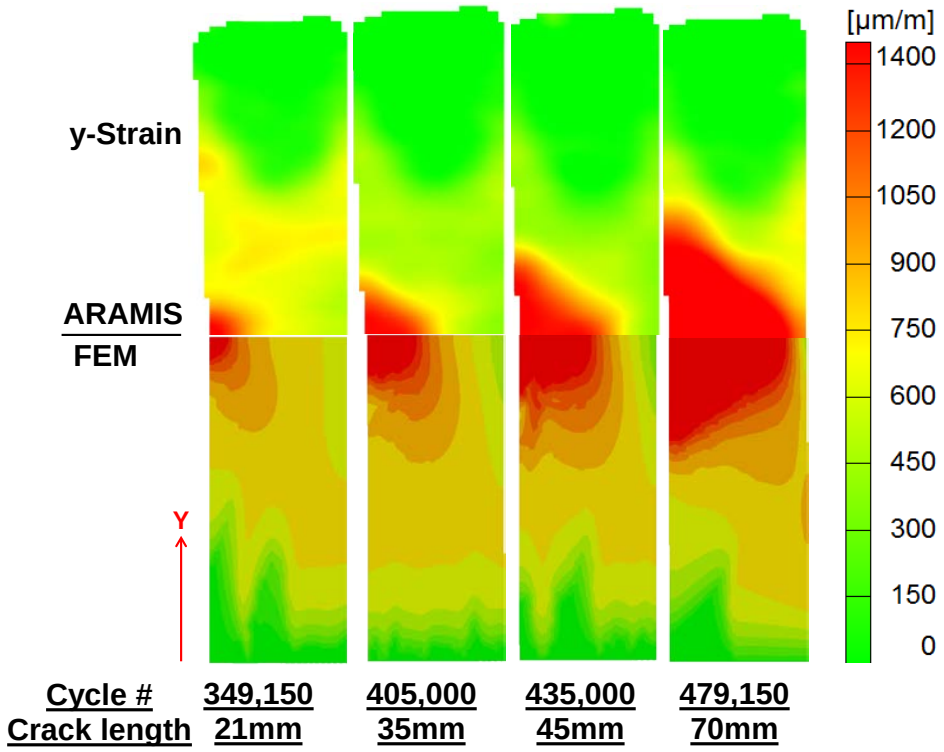

Figure 4.9 Comparison of surface strain profile obtained from DIC and FE model

At a given crack length, the size of the debonded region is maximized when the applied load in the fatigue cycle reaches its maximum value. In the subsequent tens or hundreds of unloading and loading cycles the size and shape of the debonded region remains essentially constant given that the crack propagation is stable and relatively slow. Thus, each strain contour shown in Figure 4.9 represents the debonding pattern that was induced by the maximum applied load in the fatigue cycle for the corresponding crack length, regardless of the instantaneous applied load. Therefore, in the numerical model the maximum fatigue load was used to predict the size and shape of the debonded region for each crack length.

The lower strain profiles in Figure 4.9 were obtained from the numerical model with the same crack lengths and a constant stress of 170 MPa, which is equal to the

maximum far-field stress that was applied in the experimental fatigue cycles. The close agreement between the measured and predicted strain profiles indicates that the shape and size of the debonded region at any stage during the fatigue loading can be predicted based on the crack length and the maximum magnitude of the applied load in the fatigue cycle at that crack length. Thus, the complete fatigue history of the repaired detail does not need to be known to predict the debonding pattern. The size and shape of the debonded region was more directly evaluated using the numerical results. Figure 4.10 (a) plots the values of the damage parameter, λ, at the interface (underneath the CFRP) at stages corresponding to those in Figure 4.9; debonding is considered to occur where λ is equal to 1.

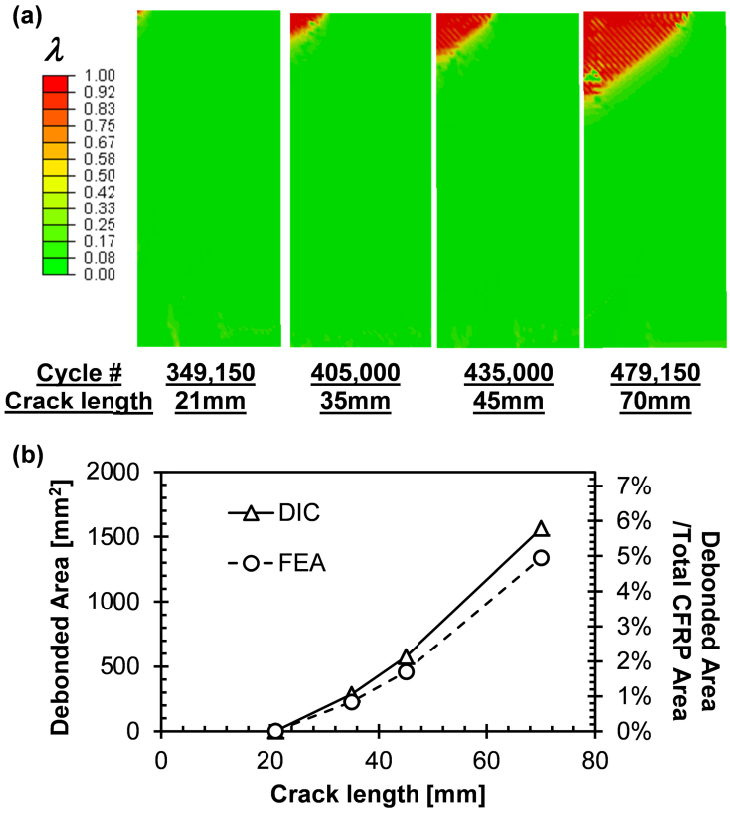

Figure 4.10 a) Contour of interfacial damage parameter at different crack lengths; b) Comparison of debonded area obtained from DIC and FE model

The debonded region, extends from the crack tip to the edge of the patch in an approximately triangular shape, but could possibly also follow an arc. The predicted debonded area at crack lengths of 21, 35, 45 and 70 mm are 2, 227, 460 and 1388 mm^2 respectively. Figure 4.10 (b) plots the comparison of the debonded area obtained from the DIC (described previously) and the FE model. The left and right vertical axes indicate the values of the debonded area and the ratio between the debonded area and the total CFRP area respectively. The maximum difference between the DIC and FE results is 226 mm^2, namely 0.83% of the total CFRP area.

4.3 Parametric study

A parametric study was conducted using the developed FE model to investigate the influence of several parameters on the size and shape of the debonded region. Considered parameters include the maximum magnitude of the applied far-field stress, σ_f, the interfacial stiffness, k, the interfacial strength, τ_0, and the energy release rate, G at the interface. The crack length was selected as 71 mm in order to have larger debonded region and magnify the influence of the investigated parameters. Table 4.2 summarizes the modeling matrix for the parametric study.

Table 4.2 Parametric study matrix

Group	σ_f [MPa]	k [MPa/mm]	τ_0 [MPa]	G [N/mm]
1	90, 125, 170, 250	600	20	0.12
2	170	300, 600, 1200	20	0.12
3	170	600	15, 20, 25	0.12
4	170	600	20	0.06, 0.08, 0.12, 0.16

The applied far-field static stress was set equal to 90, 125, 170 and 250 MPa for a crack length of 71 mm. The predicted debonded region corresponding to each applied stress level is presented in Figure 4.11. The area of the debonded region, A, and the SIF at

the crack tip, K_I, are plotted against the applied far-field stress in the figure. Below each contour the figure also indicates the calculated crack growth rate.

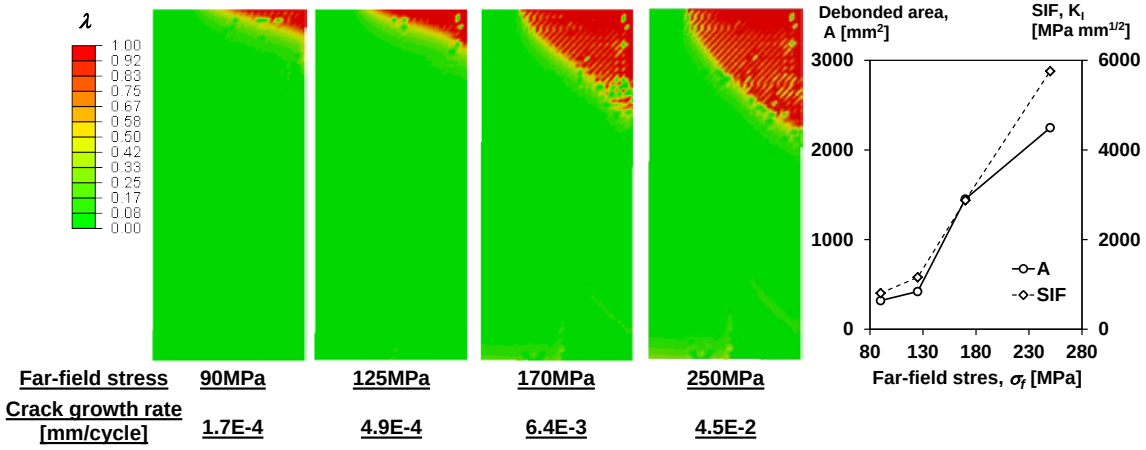

Figure 4.11 Influence of far-field stress on the debonded area, SIF and crack growth rate

In the first contour, the applied stress is 90 MPa. The debonded region is 25 mm shorter than the crack length (the parameter c is equal to 25 mm). The angle, α, is 20˚ and the third edge is straight, h is equal to 0. As the load increases in the following contours, the apex of the debonded region approaches the crack tip in the direction of the crack. The angle also increases as the load increases. When the far-field stress reaches 170 MPa, the length of the debonded region is equal to the crack length in the crack direction. The angle α is 45˚ and h is 2 mm. With further increase of the applied stress to 250 MPa, the debonded region in the crack direction remains unchanged, while the angle and the curvature of the third edge increase accordingly. It can be seen that for a given crack length, higher loads result in a larger debonded region.

Examining the figure indicates that increasing the magnitude of the maximum applied far-field stress in a fatigue cycle from 90 to 250 MPa (increase of 2.8 times), increases the SIF and the crack growth rate by 7.1 and 261 times, respectively. The

applied far-field stress had a two-fold effect on the SIF. On the one hand, the SIF is proportional to the applied stress since:

$$K_I = h(a)\sigma_f, \tag{4.3}$$

where $h(a)$ is a function of crack length, a, depending on the specimen geometry; on the other hand, the applied stress impacts the debonded area, which further influences the SIF. The influence on the crack growth rate, da/dN, is even more dramatic since the crack growth rate is related to the SIF by a power of 3.29.

The interface stiffness, k, was varied from 300 to 1200 MPa/mm while the other parameters remained unchanged. The resulting debonding contours are presented in Figure 4.12. The area of the debonded region, A, and the SIF at the crack tip, K_I, are plotted against the interface stiffness in the figure. The figure also indicates the crack growth rate below each contour.

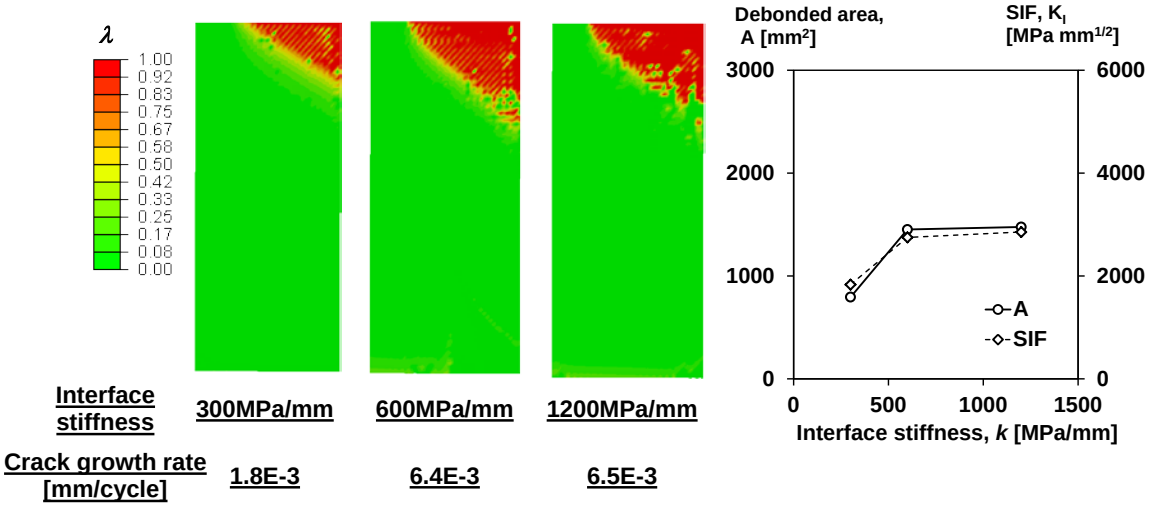

Figure 4.12 Influence of interface stiffness on the debonded area, SIF and crack growth rate

It can be seen from the figure that the debonded region becomes slightly larger as the interfacial stiffness increases. By increasing the interface stiffness from 300 to 1200

MPa/mm, the debonded area increased to 1.8 times its initial value. This indicates that, all else being equal, a stiffer interface between the CFRP and the steel results in a larger debonded area. The corresponding SIF and crack growth rate increased up to 1.6 and 3.6 times their initial values. Compared to the effect of the applied load, increasing the interface stiffness has a relatively small impact on the debonded area, SIF, and crack growth rate.

The interfacial strength, τ_0, was varied from 15 to 25 MPa while the other parameters were kept unchanged. The corresponding debonded regions are presented in Figure 4.13. The debonded area and the SIF are plotted against the interfacial strength in the figure, while the corresponding crack growth rates are indicated below each contour. The figure indicates that the size of the debonded region decreases by 70% when the interfacial strength increases by 67%. The SIF and the crack growth rate decreased by 55% and 90%, respectively when the interfacial strength was increased by 67% from 15 MPa to 25 MPa.

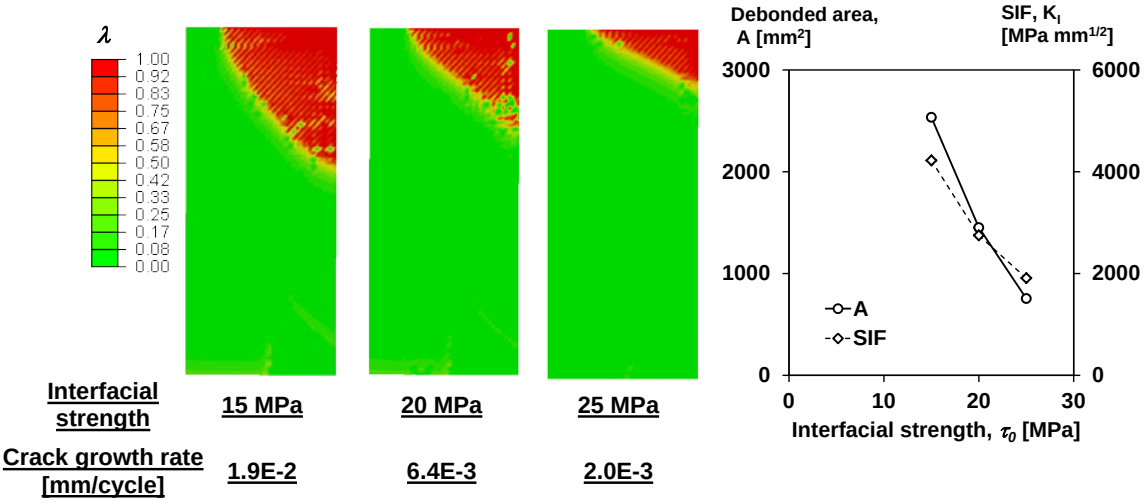

Figure 4.13 Influence of interfacial strength on the debonded area, SIF and crack growth rate

The energy release rate, *G*, was varied from 0.06 to 0.16 N/mm. The resulting debonding contours are presented in Figure 4.14. The figure also presents the debonded area, SIF and crack growth rate. It can be seen from the figure that the debonded area decreases slightly as the energy release rate increases. Increasing the energy release rate to 2.67 times decreases the debonded area by 30%, while the SIF and the crack growth rate decreased by 22% and 52% respectively. This indicates that the toughness of the interface has a relatively small impact on the debonded region, specifically, the tougher the interface the smaller the debonded region.

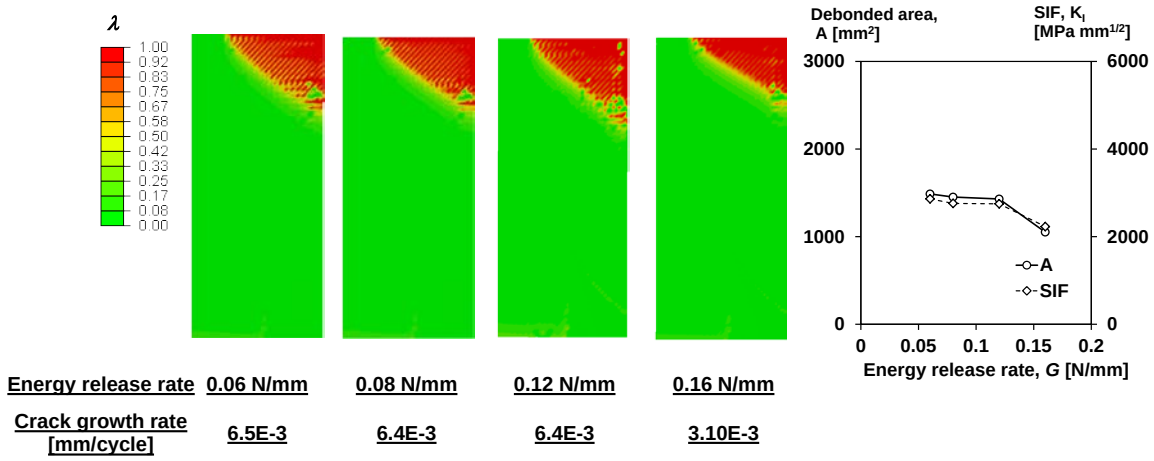

Figure 4.14 Influence of energy release rate on the debonded area, SIF and crack growth rate

The results indicate that the applied load and the interfacial strength have the most significant impact on the size and shape of the debonded region near the crack, and correspondingly, on the stress intensity factor and crack growth rate in the underlying steel element. In contrast, changing the interfacial stiffness and the energy release rate has a relatively minor influence on the size and shape of the debonded region. This indicates that the debonded region along the crack of a CFRP overlaid specimen is

dependent not only on the fatigue detail and crack length, but also on the applied maximum fatigue load and the mechanical properties of the bonded interface.

4.4 Summary

A series of numerical simulations of FRP patched single edge-notched tension coupons with different assumed debonded regions was conducted. Results showed that the stress intensity factor at the crack tip in the steel was proportional to area of the debonded region. Furthermore, since the crack growth rate was proportional to the stress intensity factor raised to the 3.29 power, different shapes and sizes of the debonded regions along the crack resulted in substantially different crack growth rate predictions. Therefore, it is important to accurately predict the crack-induced debonding to obtain a more accurate prediction of the fatigue life improvement that can be achieved by patching cracked steel structures with CFRP.

An experimental-numerical investigation was conducted to understand the crack-induced debonding and develop a model that is able to accurately predict the debonding pattern. Experimental results showed that the interfacial debonding was initiated by the crack and is dependent on the crack length. A FE model simulating the tested specimens at different loading stages and crack lengths was developed based on the assumption that the debonding was dependent on the maximum fatigue load. Close agreement between the numerical and experimental results was obtained, thereby validating the model.

Finally, a parametric study was conducted to investigate the influence of the applied far-field stress, σ_f, the interfacial stiffness, k, the interfacial strength, τ_0, and the interfacial energy release rate, G on the debonded region and the crack growth rate using the developed FE model. Results showed that the applied load and the interfacial shear

strength had the most significant impact on the size and shape of the debonded area, the stress intensity factor, and the crack growth rate. Changing the interfacial stiffness and the energy release rate of the interface had relatively minor influences on the size and shape of the debonded region.

Chapter 5 : Numerical framework

This chapter summarizes the FCG analysis of steel element reinforced with the newly developed SMA/FRP composite. There are two highlights in this analysis that have not been presented in previous studies. Firstly, a FE model that is able to predict the interfacial debonding between the FRP overlay and the substrate during crack propagation was implemented in the FCG analysis. Secondly, the crack initiation and the small crack propagation stages (typically when crack length is smaller than 1mm) were taken into account in this study using an equivalent initial flaw size method (Liu and Mahadevan, 2009; Xiang et al., 2010; Shahini and Kashani, 2013). A parametric study was also conducted to better understand the influence of various parameters on the effectiveness of the developed SMA/FRP patching system.

5.1 Description of the numerical framework

Figure 5.1 presents the flow chart of the numerical framework. The individual steps are described in details in the following.

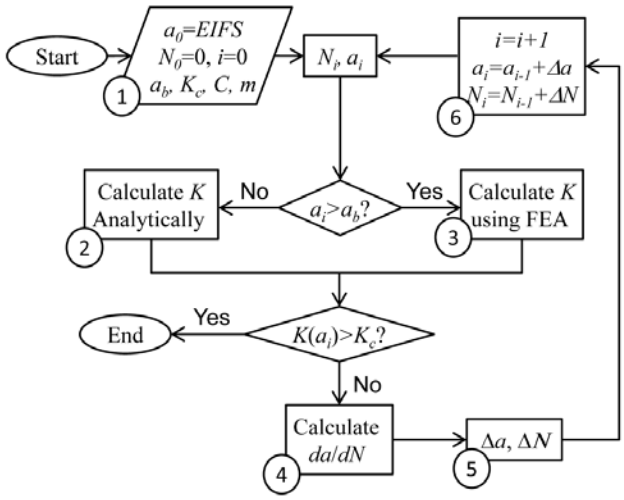

Figure 5.1 Summary of numerical framework

5.1.1 Initial conditions of the FCG analysis (Step 1)

For pre-cracked elements (elements with pre-existing cracks prior to installation of the CFRP patches), the initial crack length, a_0, is equal to the length of the pre-existing crack. For specimens that have no pre-existing crack, a_0 is taken as the EIFS (Pearson, 1975; Lankford, 1982; Kaynak, 1996, Newman et al., 1999, Lukas and Kunz, 2003, Johnson, 2010). In this model, the EIFS was assumed to be a material constant determined from the experimental data of un-patched single edge-notched steel coupons (Liu and Mahadevan, 2009; Xiang et al., 2010; Shahini and Kashani, 2013). The value of the EIFS was selected based on the best match between the calculated and tested fatigue lives of the control coupons under different stress ranges. Details of the selection of EIFS value are discussed in the following section. The corresponding initial fatigue life, N_0, and iteration index, i, are both zero.

In order to facilitate SIF calculation, the entire crack growth of a FRP-patched steel element is divided into the small crack regime and the long crack regime. For specimens with a crack starter of an edge notch, the boundary crack length, a_b, which defines the transition from the short crack growth regime to the long crack growth regime, can be determined mathematically. The mode I SIF, K_I, for long cracks is calculated using the empirical equation proposed by Tada et al. (2000):

$$K_{I-long} = F\sigma\sqrt{\pi(a+c)} \text{ and} \tag{5.1}$$

$$F = \sqrt{\frac{2b}{\pi(a+c)}\tan\frac{\pi(a+c)}{2b}}\cdot\frac{0.752+2.02((a+c)/b)+0.37(1-\sin\frac{\pi(a+c)}{2b})^3}{\cos\frac{\pi(a+c)}{2b}}, \tag{5.2}$$

where a is the crack length, c is the crack starter dimension (shown in Figure 5.2), b is the specimen width, σ is the nominal stress in the steel considering the FRP patching effect,

and F is the geometry coefficient. Figure 5.2(a) shows the illustration of long crack regime of single edge-notched specimen.

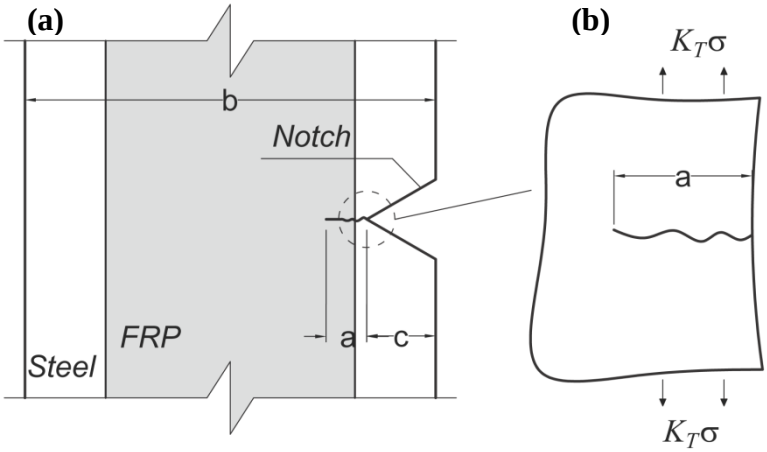

Figure 5.2: Illustrations of: (a) long crack in single edge-notched specimen, (b) small crack

For small cracks, K_I is calculated by assuming an edge crack in a semi-infinite plate with far-field stress of $K_T\sigma$, as shown in Figure 5.2(b):

$$K_{I-small} = 1.12 K_T \sigma \sqrt{\pi a}\,, \tag{5.3}$$

where K_T is the stress concentration factor of the crack starter. The boundary crack length, a_b, can be determined by satisfying the condition:

$$K_{I-small}(a_b) = K_{I-long}(a_b)\,. \tag{5.4}$$

Substituting Eq.(5.1) and Eq.(5.3) into Eq.(5.4) gives:

$$\frac{K_{I-small}(a_b)}{\sigma} = \frac{K_{I-long}(a_b)}{\sigma} = F\sqrt{\pi(a_b + c)} = 1.12 K_T \sqrt{\pi a_b}\,. \tag{5.5}$$

It is seen that the boundary crack length, a_b, in this model is only dependent on the geometry of the steel coupon.

The fracture toughness, K_c, was conservatively taken as 2000 MPa mm$^{1/2}$ based on the test data. The crack growth rate is relatively high when the SIF approaches the

fracture toughness. Therefore the influence of the value of K_c on the resulting calculated fatigue life is minimal. The crack growth rate constants C and m, were determined as 3.38×10^{-14} and 3.29 respectively.

5.1.2 SIF calculation of small crack (Step 2)

The calculation of K_I for the small crack regime and the long crack regime are treated differently. For the small crack regime, the SIF is calculated analytically using Eq. (5.3). The stress concentration factor, K_T, of the 60^o V-shaped single notched plate under pure tension was calculated as described in Noda et al. (1995):

$$K_T = \frac{(K_{ts}-1)(K_{td}-1)}{\sqrt{(K_{ts}-1)^2+(K_{td}-1)^2}}+1, \tag{5.6}$$

where K_{ts} and K_{td} are stress concentration factors of a shallow notch and a deep notch defined as

$$\begin{gathered} K_{ts} = (1.035+0.0261\eta-0.1451\eta^2+0.0842\eta^3)K_{tE} \\ K_{tE} = (1.121-0.2846\eta+0.3397\eta^2-0.1544\eta^3)K_{tH} \\ K_{tH} = 1+2/\eta \\ \eta = \sqrt{\rho/c} \\ K_{td} = \frac{\beta_1-2\beta_2}{1-\frac{\beta_2}{\sqrt{(b-c)/\rho+1}}} \end{gathered}, \tag{5.7}$$

where K_{tE} and K_{tH} are components for calculating K_{ts}, η is geometry constant, ρ is the radius of the notch root, β_1 and β_2 are geometry constants that can be calculated as described in Noda et al. (1995).

5.1.3 SIF calculation of long crack (Step 3)

For the long crack regime, two separate but similar FE models, the debonding model and the SIF model, are used to first calculate the debonding between the FRP and

the steel, and then calculate K_I based on the debonded region. The debonding model described in Figure 4.8 is used to predict the debonded region. Subsequently, the SIF model, described in Figure 4.1, was used to calculate the SIF, K_I, at the crack tip by implementing the size and shape of the debonded region obtained from the previous debonding modeling. The magnitude of the SIF that was obtained from the model is equal to the maximum value in the fatigue cycle, K_{max}, since the maximum value of the tensile fatigue load was applied to the model. The minimum SIF, K_{min}, was scaled proportionally to the applied tension load as $K_{max} \cdot R$, where R is the far-field stress ratio.

5.1.4 Crack growth rate calculation (Step 4)

The modified power relationship proposed by Elber (1971), as shown in Eq. (2.17) was used to calculate the crack growth rate based on the calculated SIF for both the small crack and long crack regimes.

5.1.5 Crack growth curve and fatigue life prediction (Steps 5 and 6)

SIF values and hence crack growth rates were calculated at discrete crack lengths a_i (i = 0 to n) in each iteration, where $K(a_n) < K_c$ and $K(a_{n+1}) > K_c$. The corresponding number of fatigue cycles, N_i, that elapsed as the crack propagated from a_0 to a_i was calculated based on the discrete form of the crack growth model, illustrated in Figure 5.3, as

$$N_i = \sum_{j=0}^{i-1} \frac{a_{j+1} - a_j}{C(U\Delta K\big|_{a=a_j})^m}. \tag{5.8}$$

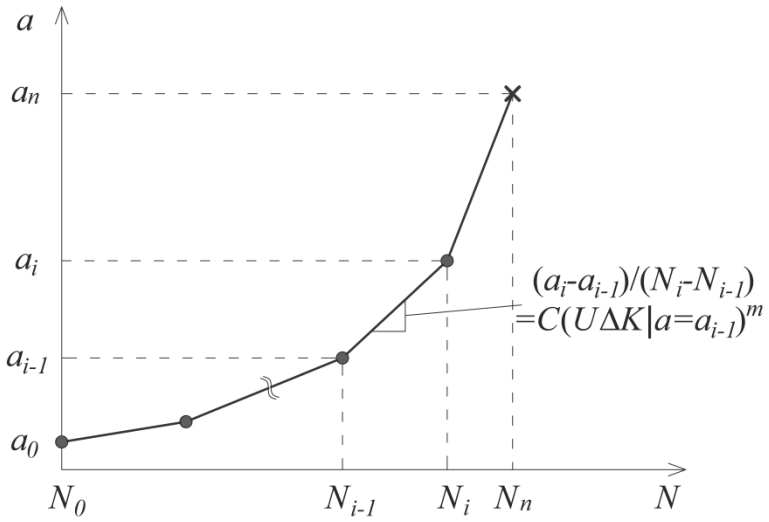

Figure 5.3 Crack growth curve and fatigue life

To obtain a sufficiently smooth crack growth curve, the SIF was evaluated at a minimum of ten crack lengths in the small crack regime and twenty crack lengths in the long crack regime. The crack growth curve is obtained by plotting (N_i, a_i); the fatigue life of the specimen is N_n.

5.2 Experimental validation

The experimental data described in Chapter 3 were used to validate the numerical framework. The data of the control group were used to calibrate the initial conditions of the numerical framework. The fatigue lives and FCG curves of the CFRP and SMA/CFRP groups were compared with the predicted results for validation.

5.2.1 Value of EIFS

The fatigue lives of the control group coupons were calculated using similar steps as shown in Figure 5.1 except that the stress intensity factor calculated in step 4 was obtained from the handbook solution given in Eq.(5.1) rather than by FE analysis. Figure 5.4 shows the coefficient of determination between the calculated and tested fatigue lives

for EIFS ranging from 20 to 36 μm. It is seen that when the EIFS is equal to 28 μm, R^2 reaches the maximum value of 0.996, which indicates the best prediction of the fatigue lives of the control coupons tested at 93 MPa, 155 MPa and 217 MPa stress ranges. Therefore, the value EIFS was selected to be equal to 28 μm for all the numerical simulations.

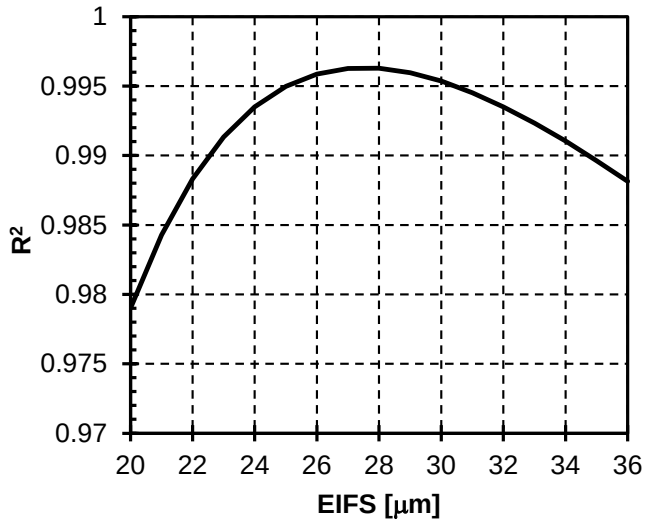

Figure 5.4 Calibration of EIFS value

5.2.2 Boundary crack length

The 60° notch root radius, ρ, was measured using a Mitutoyo Radius Gage Set with measuring scale of 0.254 to 12.7 mm. The measured radius was 0.5 mm. The stress concentration factor, K_T, at the notch root was determined using Eq. (5.6) as 5.38. By substituting the width of the coupon, b, and the notch depth, c, into Eq. (5.1) and (5.3), the relationship between the normalized stress intensity factor, K/σ, and the crack length, a, is plotted in Figure 5.5 for the short and long crack regimes. The intersection of the two curves is the boundary crack length, a_b, that was used in this study which taken equal

to 250 μm for all of the specimens and defines the transition from small crack to long crack calculation.

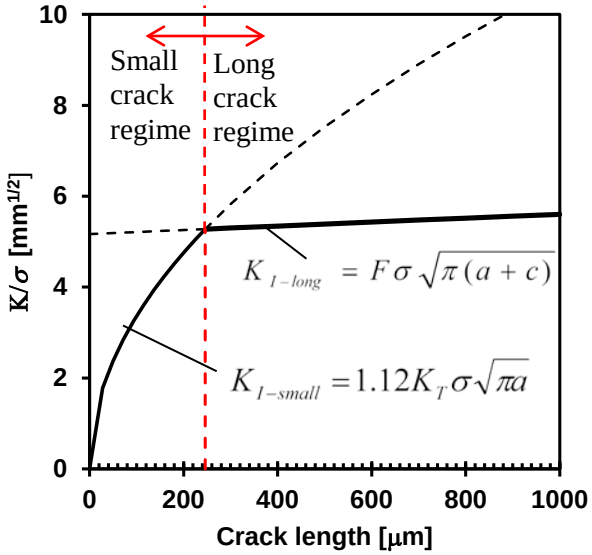

Figure 5.5 Boundary crack length

5.2.3 SIF calculation

The SIF for specimens in the small crack regime was calculated using Eq. (5.3). Figure 5.6 shows the maximum SIF, K_{max}, in the small crack regime for the CFRP and SMA/CFRP groups. It is seen that the SMA/FRP group coupons exhibited slightly lower K_{max} values than those of the FRP group coupons under the same stress range, which is due to the recovery stress provided by the SMA wires.

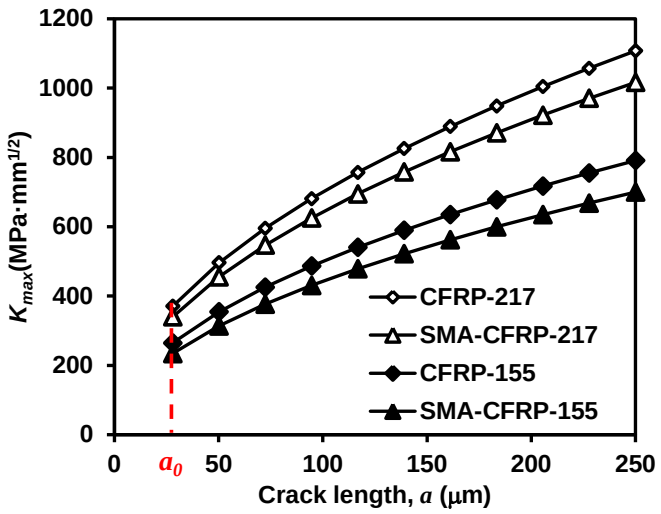

Figure 5.6 K_{max} in small crack regime

For the long crack regime, the SIF was calculated using the consecutive FE model. In the debonding model, a fine mesh size with a maximum edge length of 1.5 mm was used for the FRP and the overlaid segment of the steel substrate. In the steel substrate, away from the patched area, a coarser mesh with a maximum element edge length of 6 mm was used. The steel part consisted of 22,000 elements and 34,000 nodes; the FRP part consisted of 9,200 elements and 14,000 nodes. Parameters, τ_0, G and k in the governing bilinear traction-separation model were 20 MPa, 1.2 N/mm and 600 MPa/mm, respectively (Fawzia, et al 2010; Wu, et al 2012). Static tensile pressures of 240 and 170 MPa were applied at the end of the coupon to represent the maximum stresses in the fatigue cycles for the stress ranges of 217 and 155 MPa, respectively. Since the axial stiffness of the SMA wires, EA_{SMA}, relative to the steel plate and FRP patch is relatively small (only 2% of the total stiffness of the patched coupons), and since the wires were activated prior to installation of the CFRP overlay, their presence was not expected to have significantly influenced the near-crack debonding. As such, the presence of the SMA wires was not considered in the prediction of the size and shape of

the debonded region. Figure 5.7 compares the debonded region of coupon SMA-CFRP-217-1 with crack length of 70 mm that was predicted by the numerical model (left image) and calculated from the experimental data (right image). The left image shows the distribution of the damage parameter, λ, as shown in Eq. (4.2), at the interface. The region where λ is equal to 1 is debonded. The predicted debonded region is indicated by a dashed line. The right image shows the strain gradient distribution on the surface of the FRP obtained from the DIC data. The high strain gradient indicates high interfacial shear stress. The region that is bounded by the high shear stress and has less than 0.002 μm/m/m strain gradient, is considered as the debonded region. The close correlation between the numerically and experimentally obtained debonded regions validates the suitability of the FE model to predict the near-crack debonding of the SMA/FRP patches.

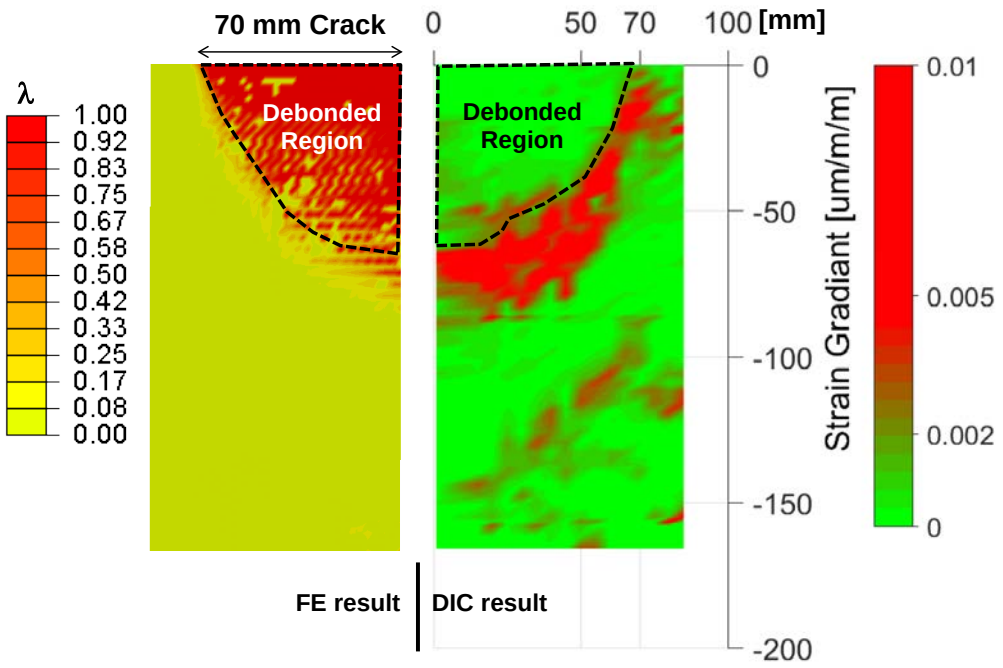

Figure 5.7 Debonded region obtained from numerical and experimental results

The predicted debonded regions corresponding to different crack lengths were then used in the SIF FE models to calculate the SIF for different crack lengths in the long crack regime. In the SIF FE model, the effect of the SMA wires was represented by applying a prestressing force to the FRP overlay so that the resulting compressive stress in the steel is equivalent to that which was produced by the SMA wires. Figure 5.8 shows the calculated maximum SIF, K_{max}, in the long crack regime for CFRP and SMA/CFRP groups.

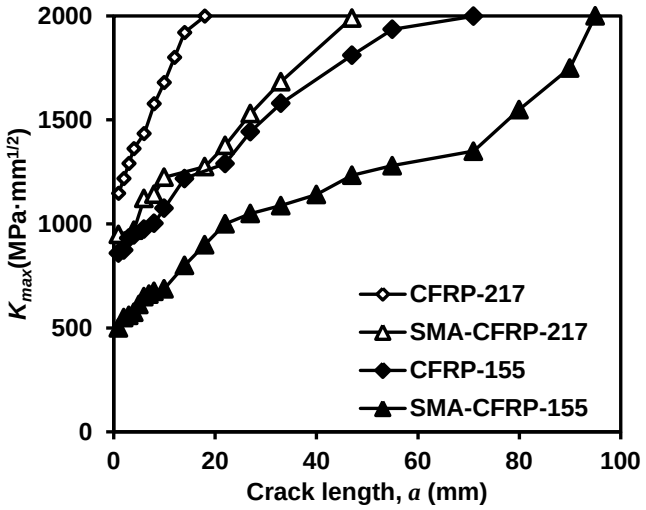

Figure 5.8 K_{max} in long crack regime obtained from FE model

Table 5.1 Calculated and measured critical crack lengths

Group	Measured critical crack length [mm]			Calculated critical crack length [mm]
	1	2	3	
CFRP-217	22	25	33	18
CFRP-155	71	80	85	71
SMA/CFRP-217	70	70	73	47
SMA/CFRP-155	78	94	94	94

It is seen that coupons in the SMA/CFRP group exhibit much lower K_{max} values than those in the CFRP group. Based on the crack growth curves of the control coupons and the C and m values, the fracture toughness, K_c, of the steel used in this research was higher than 2000 MPa·mm$^{1/2}$, which was conservatively taken as the fracture toughness

in this research. Table 5.1 summarizes the calculated and measured critical crack lengths of the tested specimens. It is seen that the calculated critical crack lengths are generally conservative compared with the measured ones.

5.2.4 Fatigue life and FCG prediction

By substituting the calculated SIF values into Eq.(5.8), the fatigue lives were calculated and compared with the tested fatigue lives in Figure 5.9. Close agreement can be observed between the predicted fatigue lives and the tested fatigue lives. The outlined results of the coupons in the CFRP-217 group exhibited premature plate-end debonding. The reinforcing effect of the FRP patch was substantially reduced due to the premature debonding, which was not captured by the proposed numerical framework and may have influenced the prediction error.

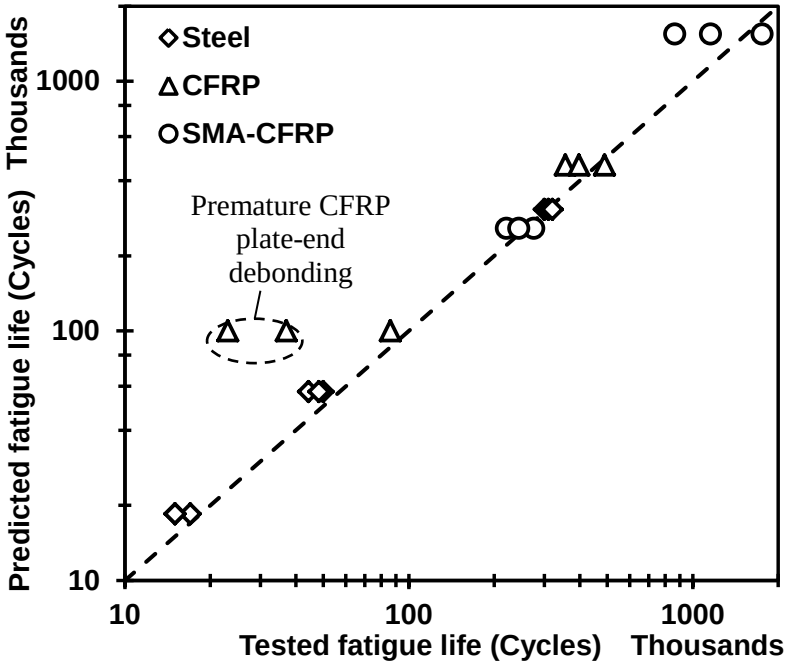

Figure 5.9 Predicted and tested fatigue lives of all of the coupons

Figure 5.10 shows the comparison of the FCG curves between the numerical and experimental results of the CFRP group of coupons. Close agreement can be found in Figure 5.10 (a) for the unstressed CFRP-155 specimens. In Figure 5.10 (b), the outliners are the coupons exhibited premature plate-end debonding of the CFRP reinforcement. The FCG analyses of small crack regime and long crack regime are indicated in the figure.

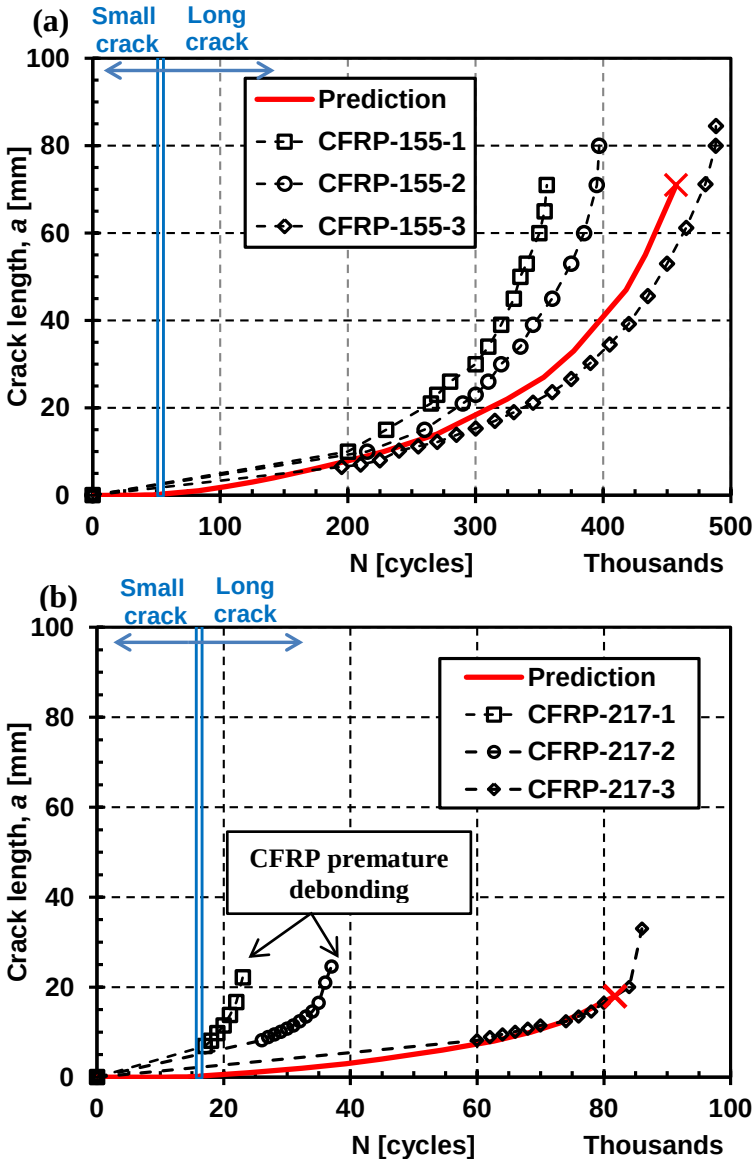

Figure 5.10 Predicted and experimental FCG curves for FRP groups

It is seen that the predicted fatigue cycles spent to propagate crack length from 28 μm to 250 μm were 11.4% and 16.1% of the entire fatigue life for CFRP-155 and CFRP-217 respectively. This indicates that the small crack regime is essential for FCG analysis.

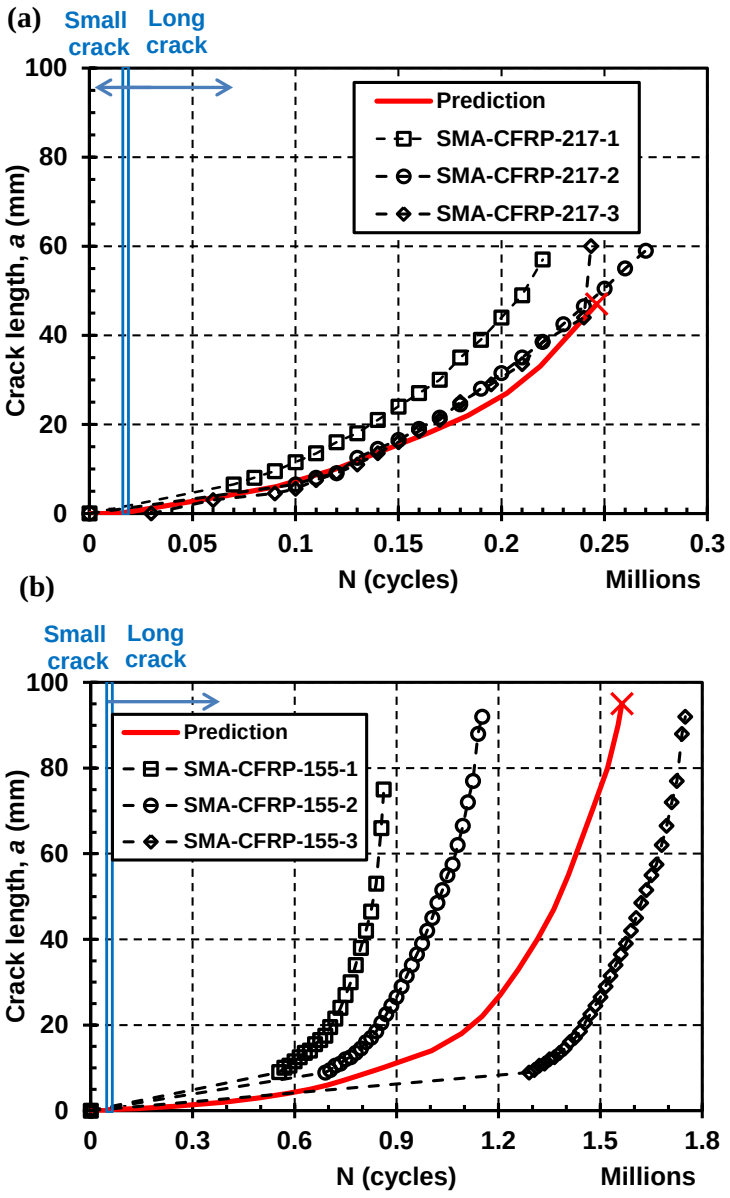

Figure 5.11 Predicted and experimental FCG curves for SMA/CFRP groups

Figure 5.11 shows the comparison of the FCG curves between the numerical and experimental results of the SMA/CFRP group of coupons. A scatter can be seen for the

experimental data of the three specimens in SMA/CFRP-155 group (Figure 5.11(b)). This is caused by the inherent variability of the specimens such as the initial curvature of the steel plate, the detail of the 60^o notch, the resulting position of the SMA/CFRP patch and the recovery stress distribution among the SMA wires. The predicted FCG curve is approximately parallel with the experimental data, which indicates close agreement with the crack growth rate. Figure 5.11(b) shows the close FCG curve prediction of the SMA/CFRP-217 group. The predicted fatigue lives spent in small crack regime were 3.5% and 7.1% for SMA/FRP-155 and SMA/CFRP-217 respectively.

5.3 Parametric study of the SMA/CFRP system

In order to better understand the effect and guide the application of the developed SMA/CFRP strengthening system, a parametric study was conducted using the established numerical framework. The considered parameters were: i) the number of the SMA wires, n_{SMA}, (and the corresponding compressive stress in steel, σ_p); ii) the applied far-field stress range, $\Delta\sigma_f$; and iii) the crack length at the time of installing the reinforcement, a_0. The patch configuration of 46 SMA wires and far-field stress range of 217 MPa were used as baseline model. Table 5.2 summarizes the modeling matrix for the parametric study. Group 1 studies the influence of n_{SMA} on the SIF values and fatigue lives under different far-field stress ranges. Group 2 studies the influence of a_0 on the fatigue lives at different far-field stress ranges.

Table 5.2 Parametric study matrix

Group	n_{SMA}	σ_p [MPa]	$\Delta\sigma_f$ [MPa]	a_0 [mm]
1	0, 10, 20, 30, 40, 46	0, 3.7, 7.4, 11, 14.8,17	217, 155, 185, 125	2.8×10^{-5}
2	46	17	217, 155	2.8×10^{-5}, 5, 10,15,20

5.3.1 Influence of the number of SMA wires

The prestress of the developed SMA/CFRP system is achieved by thermally activating the embedded SMA wires. The prestress level is proportional to the number of the embedded SMA wires in the system, which is limited by the width of the SMA/CFRP patch since the minimum spacing between neighboring wires is equal to the wire diameter (El-Tahan et al., 2015). The diameter of the wires used in this research was 0.79 mm. Thus, a maximum of 46 wires can be embedded in a 76 mm wide patch. Therefore, the number of SMA wires was set equal to 0, 10, 20, 30, 40 and 46, while two layers of FRP were considered. Figure 5.12 plots the predicted fatigue lives of the coupons with different number of SMA wires in the S-N chart. The fatigue lives of details in categories A, B, B', C and D, and the constant-amplitude fatigue thresholds (CAFT) of categories A and B (AASHTO, 2012) are indicated in the figure. It is seen that increasing the number of SMA wires from 0 to 46 increases the fatigue life of the edge notched details by two AASHTO fatigue categories (2012) at all of the stress ranges considered.. By comparing the increase at different stress ranges, the figure indicates that increasing the number of SMA wires in the SMA/FRP patch yields greater fatigue life improvements at lower stress ranges. Comparing using 46 SMA wires to no SMA wires, at stress range of 217 MPa the increase of fatigue life is 130,000 cycles representing an increase of 260% while at stress range of 125 MPa the increase of fatigue life is 3.4 million cycles representing an increase of 410%. The fatigue life of coupons with 46 SMA wires exceeds the CAFT of category A details at 125 MPa stress range suggesting a theoretically infinite fatigue life for this repaired configuration.

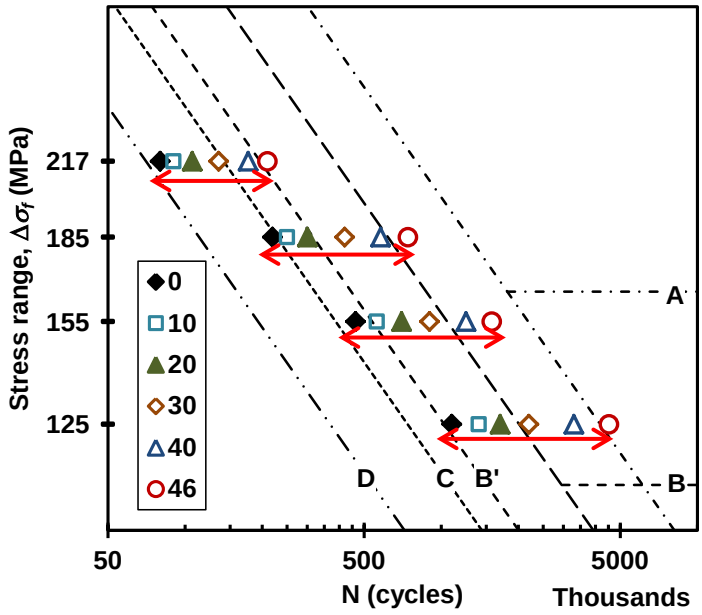

Figure 5.12 Influence of the number of SMA wires on the fatigue life

The crack growth curves of the coupons under 217 MPa stress range are presented in Figure 5.13. It is seen from the figure that increasing the number of SMA wires decreases the crack growth rate. The figure also shows that increasing the number of SMA wires allows the crack to propagate further before fracture failure when the maximum SIF reaches the fracture toughness. As indicated in the figure, the critical crack lengths are 18, 27, 33, 38, 43 and 47 mm corresponding to 0, 10, 20, 30, 40 and 46 SMA wires. Similar trends were observed for the other stress ranges considered, but the increase of the critical crack length was most pronounced at the highest stress range. The combined effect of slower propagation rate and longer propagation path due to the SMA wires improves the fatigue capacity of the reinforced coupons.

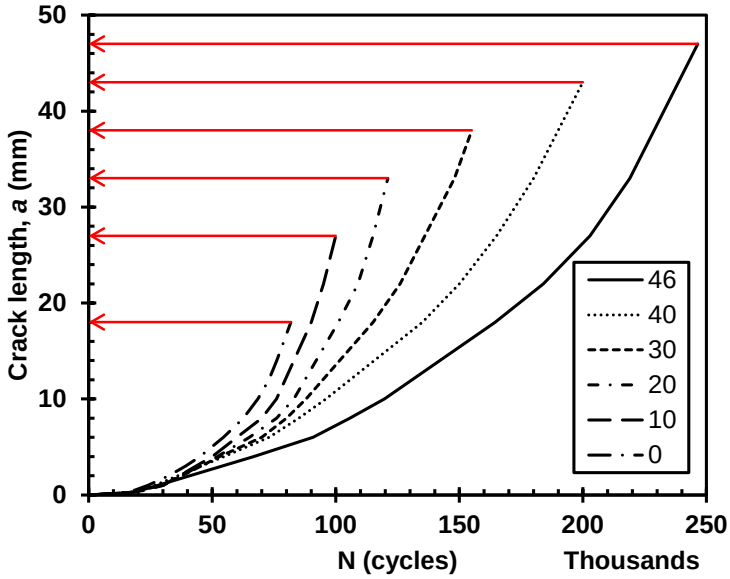

Figure 5.13 Influence of the number of SMA wires on the K_{max} at different crack lengths

5.3.2 Influence of the initial crack length at time of strengthening

The FCG curves of the coupon reinforced with SMA/FRP patches at crack lengths of 28 μm, 5 mm, 10 mm, 15 mm and 20 mm were calculated. Figure 5.14 (a) and (b) shows the results for 155 and 217 MPa stress ranges, respectively. It is seen that if the fatigue detail is reinforced before the generation of a visible crack, the fatigue life is improved by 27 and 14 times. If the fatigue detail is reinforced when the crack length is appreciable, for example 20 mm under 155 MPa stress range, the fatigue life is improved by 8 times. This indicates the significance of earlier strengthening of a fatigue detail. Nevertheless, the SMA/FRP patch is promising as a method of emergency repair. For example, when the stress range is 217 MPa and the crack length is 10 mm, the remaining fatigue life is 2,400 cycles. By applying the SMA/FRP patch, the remaining fatigue life is increased to 139,000 cycles. The 217 MPa stress range represents maximum stresses of 60% of yielding stress, which is relatively high. Given average daily traffic that is

equivalent to 400 loading cycles of 217 MPa stress range to a member, an unrepaired crack would cause failure within six days. In contrast, installing a SMA/FRP patch on the crack would extend the life to 340 days providing significant opportunity to implement a long-term solution even for a severely deteriorated structure.

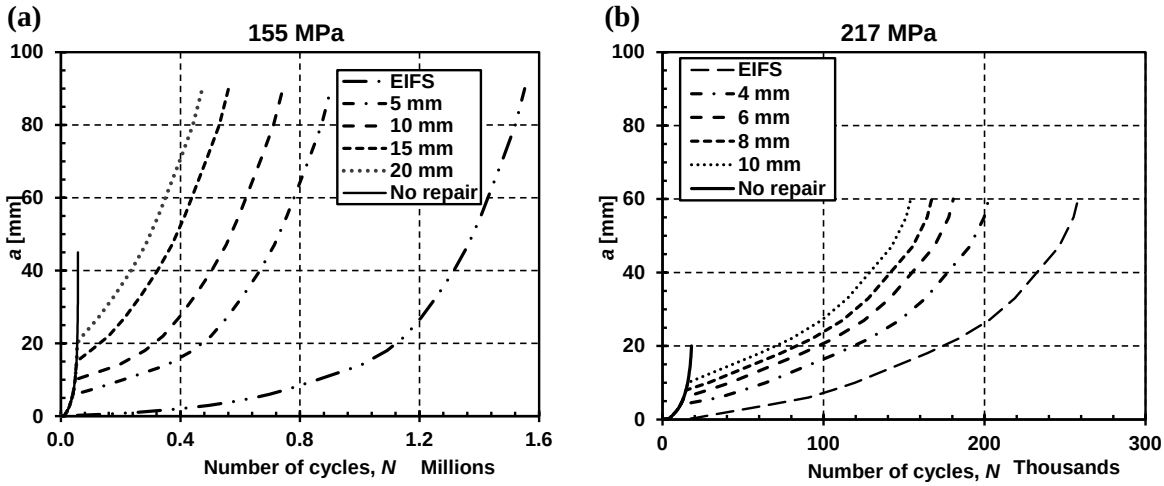

Figure 5.14 Fatigue crack growth curves of coupons strengthened at different crack lengths

5.4 Discussions

A LEFM-based numerical framework was established to predict the FCG of steel elements strengthened with a newly developed SMA/CFRP composite patch. The framework takes into account the small crack growth and the interfacial debonding during the crack propagation. An approach to determine the boundary crack length which differentiates between the small crack and long crack regimes was proposed. In the small crack regime, the SIF was calculated using the analytical model; while in the long crack regime, a multi-step FE model was used to calculate the SIF. The same crack propagation law was used in both the small and long crack regimes, which was corrected by adoption

of an EIFS. Finally, the FCG curve and fatigue life prediction was conducted by iterative analysis.

An experimental study consisting of one group of control coupons and two groups of coupons reinforced with CFRP and SMA/CFRP patches was used to validate the proposed framework. A parametric study was carried out using the developed numerical framework to further understand the strengthening effect of the SMA/CFRP system. The considered parameters were the number of SMA wires, the applied far-field stress range, and the crack lengths at which the SMA/CFRP was installed. It was found that increasing the number of SMA wires increased the fatigue life of the edge notch detail by two AASHTO fatigue categories at all of the stress ranges considered in the study. The patch was more effective at lower stress ranges. SMA wires decreases the crack growth rate while also allowing the crack to propagate further before failure. The combined effect substantially increased the fatigue life of the coupons. Finally, it was found that earlier installation maximizes the fatigue life extension that can be achieved using the patching technique. However, the patch can still substantially increase the remaining fatigue life of a member that would otherwise fail in a short amount of time and, therefore, could also be useful for emergency repairs.

Chapter 6 : Summary, Conclusions and Future work

This dissertation presents the original experimental and numerical work of investigating a thermally activated SMA/FRP patching system for fatigue strengthening of steel structures. The effectiveness of using the composite patch to elongate fatigue life of steel element was quantified by fatigue testing of 27 specimens. The fatigue crack induced interfacial debonding was studied using DIC technique and FE analysis. A numerical framework was developed to predict the behavior of steel elements patched with the SMA/FRP composite. The conclusions of each part and the recommended future work are summarized in this chapter. Putting into the context of practical applications, however, there are still technical questions to be investigated.

6.1 The effectiveness of the SMA/FRP patch in fatigue strengthening of steel elements

Four groups of single edge notched coupons were reinforced with: (i) un-strengthened, (ii) CFRP only, (iii) prestressed SMA patches only (without the CFRP overlay), and (iv) SMA/CFRP composite patches. They were tested under tension-tension fatigue loading up to failure at stress ranges of 93, 155 and 217 MPa. The beach marking technique was used to record the crack fronts, and the DIC technique was used to record the strain contour at the surface of the reinforcement. The findings are listed as follows:

- The SMA/CFRP composite patch was able to increase the average fatigue lives of the single edge-notched steel plates to 26.7 and 15.3 times those of the unpatched plates at 155 and 217 MPa stress ranges respectively. This validates the central

hypothesis of this research that the fatigue life of crack-sensitive steel elements can be significantly extended using this newly developed SMA/CFRP patch.

- There is a synergistic effect between the two components of the patching system: CFRP overlay and prestressed SMA wires. At stress range of 155 MPa, the steel plates patched only with CFRP overlay exhibited 8.7 times average fatigue life that of the unpatched samples; those patched prestressed SMA wires alone exhibited 1.7 times average fatigue life that of the unpatched coupons. However, patched with the combination of CFRP overlay and SMA wires, the steel plate exhibited 26.7 times the average fatigue life that of the unpatched ones. This indicates that the patching system is more effective than the simple sum of the reinforcing effects of the CFRP and the prestressed SMA wires.
- Near-crack debonding was observed for all of the coupons that were patched with CFRP and SMA/CFRP patches during the fatigue loading by the DIC system. The observations suggest that the fatigue loading does not impact the debonding directly. Rather, fatigue loading causes propagation of the crack in the steel, and the increase of the crack length drives the propagation of the debonded region.
- Plate-end debonding was only observed for the coupons that were patched only with CFRP patches and tested at the 217 MPa stress range. The bonded patch immediately loses the strengthening effect when this type of debonding occurs. Observations suggest that higher applied maximum fatigue load is more likely to induce this type of debonding.

6.2 Near-crack debonding between FRP overlay and steel under fatigue loading

In order to understand the influence of the near-crack debonding on the fatigue crack growth analysis, a series of numerical simulations of FRP patched single edge-notched tension coupons with different assumed debonded regions was conducted. A FE model using traction-separation law to simulate the FRP-steel interface was developed to predict the near-crack debonding. A parametric study was conducted to further understand the influence of different parameters on the debonded region using the developed FE model. The following conclusions are drawn:

- The predicted SIF at the crack tip in the steel was proportional to area of the assumed debonded region. This indicates that it is necessary to use accurate debonded region in the model for accurate prediction of the SIF. Furthermore, since the crack growth rate was proportional to the stress intensity factor raised to the 3.29 power, different shapes and sizes of the debonded regions result in substantially different crack growth rate predictions.
- In the numerical model, only the maximum fatigue load, regardless of the instantaneous applied load, was used to predict the size and shape of the debonded region for each crack length. This is because at a given crack length, the size of the debonded region is maximized when the applied load in the fatigue cycle reaches its maximum value. In the subsequent tens or hundreds of unloading and loading cycles the size and shape of the debonded region remains essentially constant given that the crack propagation is stable and relatively slow.

- A FE model was developed to predict the near-crack debonding under fatigue loading. The interface was simulated using a cohesive zone model with bilinear traction-separation law. The model was validated by the experimental data from DIC system.
- A parametric study was conducted to investigate the influence of the applied far-field stress, σ_f, the interfacial stiffness, k, the interfacial strength, τ_0, and the interfacial energy release rate, G on the debonded region and the crack growth rate using the developed FE model. It was found that the applied load and the interfacial shear strength had the most significant impact on the size and shape of the debonded area, the stress intensity factor, and the crack growth rate. Changing the interfacial stiffness and the energy release rate of the interface had relatively minor influences on the size and shape of the debonded region.

6.3 Numerical framework to perform the FCG analysis

A LEFM-based numerical framework was established to predict the FCG of steel elements strengthened with the SMA/FRP patch. The crack was assumed to start at a virtual length of EIFS. The crack advances incrementally by iterating the steps of the framework until the crack length reaches the critical length where the SIF at the crack tip exceeds the fracture toughness. It takes into account the small crack growth and the interfacial debonding during the crack propagation. A parametric study was conducted to further understand the strengthening effect of the SMA/FRP patch. An approach to determine the boundary crack length which differentiates between the small crack and long crack regimes was proposed. In the small crack regime, the SIF was calculated using the analytical model; while in the long crack regime, a multi-step FE model was used to

calculate the SIF. The same crack propagation law was used in both the small and long crack regimes. The framework was validated by the experimental data of fatigue lives and crack growth curves.

A parametric study was carried out using the developed numerical framework to further understand the influence of the number of SMA wires, the applied far-field stress range, and the crack lengths at which the SMA/FRP was installed on the strengthening effect of the SMA/FRP patch. Results showed that increasing the number of SMA wires allows the crack to propagate further. Because the prestressing force decreases the SIF at the crack tip hence the maximum SIF reaches the fracture toughness when the crack is longer.

It was found that earlier installation maximizes the fatigue life extension that can be achieved using the patching technique. If the fatigue detail is reinforced before the generation of a visible crack, the fatigue life is improved by 27 and 14 times. If the fatigue detail is reinforced when the crack length is appreciable, for example 20 mm under 155 MPa stress range, the fatigue life is improved by 8 times. However, the patch can still substantially increase the remaining fatigue life of a member that would otherwise fail in a short amount of time. For example, when the stress range is 217 MPa and the crack length is 10 mm, given average daily traffic that is equivalent to 400 loading cycles of 217 MPa stress range to a member, the SMA/FRP patch can extend the fatigue life from six days to 340 days.

6.4 Limitations

This research presents the first use of SMA/FRP composite in fatigue strengthening of steel structures. The limitations of this research are:

- The fabrication and testing of the specimens were conducted at room temperature. The mechanical properties of the epoxy, SMA wires, the FRP-SMA interface, and FRP-steel interface are sensitive to the environmental temperature. Therefore, the strengthening effect demonstrated in this research is limited to room temperature.
- The steel plates were reinforced with the SMA/FRP patches on both sides in this research. The patching system might be less effective for one-side strengthening.
- The patch was used to strengthen small scale steel plates. The effectiveness of fatigue strengthening of large scale structure members was not quantified.
- The individual SMA wires were not simulated in the numerical model, which could potentially impact the accuracy of the model.
- Previous studies pointed out the limitations of strain accuracy and inconsistencies of displacement measurement of DIC system and proposed methodologies of mitigating such problems. The accuracy and the post-processing approaches in this research need to be further investigated to better understand the interfacial debonding and guide the numerical simulation.

6.5 Future work

This research demonstrated a promising technique in fatigue strengthening of steel structures. More investigations are needed in order to further understand its applicability for different types of fatigue damage, effectiveness in practical use, and superiority compared with the conventional technologies.

The effectiveness of the patching system on distortion-induced fatigue details needs to be quantified. There is a pressing need for alternative repair techniques for so-called distortion-induced cracks. These types of cracks form at sensitive details

characterized by out-of-plane tearing, also known as Mode III crack propagation. Since the mechanism of Mode III crack propagation is different from traditional stress-induced, Mode I, crack propagation, the effectiveness of the patch to repair these types of cracks needs to be validated.

The influence of surface preparation techniques on patch effectiveness needs to be quantified. Due to the presence of lead-based paint on older steel bridges, grit blasting, the surface preparation method used in this research, requires specific and costly environmental controls which represents a major technical barrier to adoption of this technology. Alternatively, surface preparation using power tools to a textured, bare metal surface following chemical removal of lead paint was recommended as an acceptable surface preparation technique that does not require the same environmental controls. While this technique seems to be viable given the limited area over which surface preparation is required, there has not been any testing or validation to confirm that the bond strength achieved using this technique is adequate. To overcome these technical barriers, experimental and numerical investigations regarding surface preparation are needed.

The developed technique needs to be directly compared with the current leading approaches in repairing fatigue damage, which are drilling crack-stop holes and welding steel cover plate (or the so called ‘fish plate’). In addition to directly comparing the repair techniques, the potential to use the SMA/FRP patches as a complimentary technology may also be investigated. By doing so, the engineering merit of the new technique can be more directly evaluated.

The normal behavior between the FRP and steel needs to be further understood through experimental testing. By incorporating the normal behavior at the interface into the current numerical framework, the plate-end debonding can be captured and the associated fatigue strengthening effect of the SMA/FRP patching system can be predicted.

A novel iron-based SMA sheet material is commercially available. The SMA sheet can potentially be used as an alternative to the SMA/CFRP composite in fatigue strengthening. Experimental investigation of using the iron-based SMA sheet to strengthen fatigue sensitive elements is needed to evaluate the effectiveness of this alternative.

References

AASHTO (American Association of State Highway and Transportation Officials). (2012). "LRFD bridge design specifications," Washington, DC.

ABAQUS version 6.12-1 [Computer software]. Dasault Systèmes Simulia, Providence, RI.

Andrawes, B., McCormick, J., & DesRoches, R. (2004). "*Effect of cyclic modeling parameters on the behavior of shape memory alloys for seismic applications.*" In A. B. Flatau (Ed.), SPIE (Vol. 5390, pp. 324–334).

ARAMIS [Computer software]. Gom mbH, Braunschweig, Germany.

ASTM International. (2010). "Standard test method for tensile properties plastics." *D-638-10*, West Conshohocken, PA.

ASTM International. (2012). "Standard test method for Notched Bar Impact Testing of Metallic Materials." *E-23-12c*, West Conshohocken, PA.

ASTM International. (2013a). "Standard Test Methods for Tension Testing of Metallic Materials." *E-8-13*, West Conshohocken, PA.

ASTM International. (2013b). "Standard test method for measurement of fatigue crack growth rates." *E-647-13a*, West Conshohocken, PA.

ASTM International. (2014). "Standard test method for tensile properties of polymer matrix composite materials." *D-3039-14*, West Conshohocken, PA.

Beizaee, S., Xotta, G., & Willam, K. J. (2016). "*Perforation studies on flat bars for XFEM-based failure analysis*." Engineering fracture mechanics, 155, 67–87.

Bollas, D., Pappas, P., Parthenios, J., & Galiotis, C. (2007). "*Stress generation by shape memory alloy wires embedded in polymer composites.*" Acta Materialia, 55(16), 5489–5499.

Chikh, B. O., Imad, A., & Benguediab, M. (2008). "*Influence of the cyclic plastic zone size on the propagation of the fatigue crack in case of 12NC6 steel*." Computational Materials Science, 43(4), 1010–1017.

Colomb, P., Bassetti, A., & Nussbaumer, A. (2003). "*Crack growth induced delamination on steel members reinforced by prestressed composite patch.*" Fatigue & Fracture of Engineering Materials & Structures, 26, 429–437.

Colombi, P., Fava, G., & Sonzogni, L. (2015). "*Fatigue crack growth in CFRP-strengthened steel plates.*" Composites Part B: Engineering, 72, 87–96.

Di Cocco, V., Iacoviello, F., Maletta, C., & Natali, S. (2014). "*Cyclic microstructural transitions and fracture micromechanisms in a near equiatomic NiTi alloy.*" International Journal of Fatigue, 58, 136–143.

Dolce, M., & Cardone, D. (2001). "*Mechanical behaviour of shape memory alloys for seismic applications 2. Austenite NiTi wires subjected to tension.*" International Journal of Mechanical Sciences, 43(11), 2657–2677.

Domazet, Ž. (1996). "*Comparison of fatigue crack retardation methods.*" Engineering Failure Analysis, 3(2), 137–147.

Elber, W. (1970). "*Fatigue crack closure under cyclic tension.*" Engineering Fracture Mechanics, 2, 37–45.

Elber, W. (1971). "*The significance of fatigue crack closure.*" Damage Tolerance in

Aircraft Structures ASTM STP 486.

El-Tahan, M., & Dawood, M. (2016). "*Fatigue behavior of a thermally-activated NiTiNb SMA-FRP patch.*" Smart Materials and Structures, 25(1), 015030.

El-Tahan, M., Dawood, M., & Song, G. (2015). "*Development of a self-stressing NiTiNb shape memory alloy (SMA)/fiber reinforced polymer (FRP) patch.*" Smart Materials and Structures, 24(6), 065035.

Fawzia, S., Zhao, X.-L., & Al-Mahaidi, R. (2010). "*Bond–slip models for double strap joints strengthened by CFRP*." Composite Structures, 92(9), 2137–2145.

Feng, P., Hu, L., Zhao, X.-L., Cheng, L., & Xu, S. (2014). "*Study on thermal effects on fatigue behavior of cracked steel plates strengthened by CFRP sheets.*" Thin-Walled Structures, 82, 311–320.

Forman, R. G., Kearney, V. E., & Engle, R. M. (1967). "*Numerical Analysis of Crack Propagation in Cyclic-Loaded Structures.*" Journal of Basic Engineering, 89(3), 459.

Ghafoori, E., & Motavalli, M. (2011). "*Analytical calculation of stress intensity factor of cracked steel I-beams with experimental analysis and 3D digital image correlation measurements.*" Engineering Fracture Mechanics, 78(18), 3226–3242.

Ghafoori, E., Motavalli, M., Nussbaumer, A., Herwig, A., Prinz, G. S., & Fontana, M. (2015). "*Design criterion for fatigue strengthening of riveted beams in a 120-year-old railway metallic bridge using pre-stressed CFRP plates.*" Composites Part B: Engineering, 68, 1–13.

Ghafoori, E., Schumacher, a., & Motavalli, M. (2012). "*Fatigue behavior of notched steel beams reinforced with bonded CFRP plates: Determination of prestressing level for*

crack arrest." Engineering Structures, 45, 270–283.

Ghfiri, R., Amrouche, A., Imad, A., & Mesmacque, G. (2000). "*Fatigue life estimation after crack repair in 6005 A-T6 aluminium alloy using the cold expansion hole technique.*" Fatigue Fracture of Engineering Materials and Structures, 23(11), 911–916.

Graesser, E., & Cozzarelli, F. (1991). "*Shape-memory alloys as new materials for aseismic isolation.*" Journal of Engineering Mechanics, 117(11), 2590–2608.

Hart-Smith, J. (1973). "*Adhesive-bonded double-lap joints.*" Technical Rep. NASA CR-112235, Douglas Aircraft Company, Long Beach, CA.

Hmidan, A., Kim, Y. J., & Yazdani, S. (2014). "*Correction factors for stress intensity of CFRP-strengthened wide-flange steel beams with various crack configurations.*" Construction and Building Materials, 70, 522–530.

Hu, L. L., Zhao, X. L., Asce, F., & Feng, P. (2016). "*Fatigue Behavior of Cracked High-Strength Steel Plates Strengthened by CFRP Sheets.*" Journal of Composites for Construction.

Huawen, Y., König, C., Ummenhofer, T., Shizhong, Q., & Plum, R. (2010). "*Fatigue Performance of Tension Steel Plates Strengthened with Prestressed CFRP Laminates.*" Journal of Composites for Construction, 14(5), 609–615.

Hussain, K. (1997). "*Short fatigue crack behaviour and analytical models: a review.*" Engineering Fracture Mechanics, 58(4), 327–354.

Irwin, G. (1957). "*Analysis of stresses and strains near the end of a crack traversing a plate.*" Journal of Applied Mechanics, 361–364.

Johnson, W. S. (2010). "*The history, logic and uses of the Equivalent Initial Flaw Size approach to total fatigue life prediction.*" Procedia Engineering, 2(1), 47–58.

Jones, S., & Civjan, S. (2003). "*Application of fiber reinforced polymer overlays to extend steel fatigue life.*" Journal of Composites for Construction, (November), 331–338.

Kaynak, C., Ankara, A., & Baker, T. J. (1996). "*A comparison of short and long fatigue crack growth in steel*." 18(1), 17–23.

Kim, Y. J., & Harries, K. A. (2011). "*Fatigue behavior of damaged steel beams repaired with CFRP strips.*" Engineering Structures, 33(5), 1491–1502.

Klaiber, F. W., Dunker, K. F., Wipf, T. J., & Sanders, W. W. (1987). "Methods of strengthening existing highway bridges." Washington, DC.

Komano, K., Ishihara, S., McEvily, A. J., & Shibata, H. (2007). "*Effect of Microstructure on Small Fatigue Crack Initiation and Propagation Behavior of Ti-6Al-4V Alloy.*" Key Engineering Materials, 353-358, 1215–1218.

Kumar, R. (1992). "*Review on crack closure for constant amplitude loading in fatigue.*" Engineering Fracture Mechanics, 42(2), 389–400.

Lal, D., & Weiss, V. (1978). "*A notch analysis of fracture approach to fatigue crack propagation.*" Metallurgical Transactions A, 9(March), 413–426.

Lam, A. C. C., Yam, M. C. H., Cheng, J. J. R., & Kennedy, G. D. (2010). "*Study of Stress Intensity Factor of a Cracked Steel Plate with a Single-Side CFRP Composite Patching.*" Journal of Composites for Construction, 14(6), 791–803.

Lankford, J. (1982). "*The growth of small fatigue cracks in 7075-T6 aluminum.*" Fatigue

& Fracture of Engineering Materials & Structures, 5(3), 233–248.

Lau, K., Chan, A. W., Shi, S., & Zhou, L. (2002). "*Debond induced by strain recovery of an embedded NiTi wire at a NiTi r epoxy interface : micro-scale observation.*" Materials & Design, 23, 265–270.

Lee, W., & Lee, J.-J. (2005). "*FRP repaired aluminum plate.*" Journal of Composite Materials, 39(16), 1449–1463.

Liu, H., & Zhao, X.-L. (2013). "*Prediction of Fatigue Life for Cfrp Strengthened Steel Connections Under Combined Loads.*" International Journal of Structural Stability and Dynamics, 13(04), 1250059.

Liu, H., Al-Mahaidi, R., & Zhao, X.-L. (2009). "*Experimental study of fatigue crack growth behaviour in adhesively reinforced steel structures.*" Composite Structures, 90(1), 12–20.

Liu, H., Xiao, Z., Zhao, X.-L., & Al-Mahaidi, R. (2009). "*Prediction of fatigue life for CFRP-strengthened steel plates.*" Thin-Walled Structures, 47(10), 1069–1077.

Liu, Y., & Mahadevan, S. (2009). "*Probabilistic fatigue life prediction using an equivalent initial flaw size distribution.*" International Journal of Fatigue, 31(3), 476–487.

Lukas, P; Kunz, L. (2003). "*Small cracks-nucleation, growth and implication to fatigue life.*" International Journal of Fatigue, 25(9-11), 855–862.

Malécot, P., Lexcellent, C., Folte^te, E., & Collet, M. (2006). "*Shape Memory Alloys Cyclic Behavior: Experimental Study and Modeling.*" Journal of Engineering Materials and Technology, 128(3), 335–345.

Maletta, C., Sgambitterra, E., Furgiuele, F., Casati, R., & Tuissi, A. (2012). "*Fatigue of pseudoelastic NiTi within the stress-induced transformation regime: a modified Coffin–Manson approach.*" Smart Materials and Structures, 21(11), 112001.

McCormick, J., DesRoches, R., Fugazza, D., & Auricchio, F. (2007). Seismic "*Assessment of Concentrically Braced Steel Frames with Shape Memory Alloy Braces.*" Journal of Structural Engineering, 133(6), 862–870.

McEvily, A.. (1996). "*The growth of short fatigue cracks: a review.*" Transactions on Engineering Sciences, 13, 93–107.

Miyazaki, S., Imai, T., Igo, Y., & Otsuka, K. (1986). "*Effect of cyclic deformation on the pseudoelasticity characteristics of Ti-Ni alloys.*" Metallurgical Transactions A, 17(1), 115–120.

NASA. (2000) [Computer software]. "NASGRO" Version 3.0. Houston, TX.: Johnson Space Center.

Newman, J., Phillips, E., & Swain, M. (1999). "*Fatigue-life prediction methodology using small-crack theory.*" International Journal of Fatigue, 21, 109–119. Retrieved from

Paris, P., & Erdogan, F. (1963). "*A critical analysis of crack propagation laws.*" Journal of Basic Engineering Transactions ASME, 85(4), 528–534.

Paris, P., Gomez, M., & Anderson, W. (1961). "*A rational analytic theory of fatigue.*" The Trend in Engineering, 13, 9–14.

Pearson, S. (1975). "*Initiation of fatigue cracks in commercial aluminium alloys and the subsequent propagation of very short cracks.*" Engineering Fracture Mechanics, 7,

235–247.

Poon, C., Lau, K., & Zhou, L. (2005). "*Design of pull-out stresses for prestrained SMA wire/polymer hybrid composites.*" Composites Part B: Engineering, 36(1), 25–31.

Poon, C., Zhou, L., Jin, W., & Shi, S. (2005). "*Interfacial debond of shape memory alloy composites.*" Smart Materials and Structures, 14(4), N29–N37.

Rice, J. (1968). "*A path independent integral and the approximate analysis of strain concentration by notches and cracks.*" Journal of Applied Mechanics, 35, 379–386.

Sabelkin, V., Mall, S., & Avram, J. B. (2006). "*Fatigue crack growth analysis of stiffened cracked panel repaired with bonded composite patch.*" Engineering Fracture Mechanics, 73(11), 1553–1567.

Sanford, R. (2003). "Principles of fracture mechanics." Upper Saddle River, NJ.: Prentice Hall.

Schnerch, D., Dawood, M., Rizkalla, S., & Sumner, E. (2007). "*Proposed design guidelines for strengthening of steel bridges with FRP materials.*" Construction and Building Materials, 21(5), 1001–1010.

Shahani, A. R., & Moayeri Kashani, H. (2013). "*Assessment of equivalent initial flaw size estimation methods in fatigue life prediction using compact tension specimen tests.*" Engineering Fracture Mechanics, 99, 48–61.

Shimamoto, A., Ohkawara, H., & Nogata, F. (2004). "*Enhancement of mechanical strength by shape memory effect in TiNi fiber-reinforced composites.*" Engineering Fracture Mechanics, 71(4-6), 737–746.

Shin, M., & Andrawes, B. (2010). "*Experimental investigation of actively confined*

concrete using shape memory alloys." Engineering Structures, 32(3), 656–664.

Tada, H., Paris, P. C., & Irwin, G. R. (2000). "*The Stress Analysis of Cracks Handbook (Third Edition).*" New York, NY: ASME Press.

Täljsten, B., Hansen, C. S., & Schmidt, J. W. (2009). "*Strengthening of old metallic structures in fatigue with prestressed and non-prestressed CFRP laminates.*" Construction and Building Materials, 23(4), 1665–1677.

Tamai, H., & Kitagawa, Y. (2002). "*Pseudoelastic behavior of shape memory alloy wire and its application to seismic resistance member for building.*" Computational Materials Science, 25(1), 218–227.

Tavakkolizadeh, M., & Saadatmanesh, H. (2003). "*Fatigue Strength of Steel Girders Strengthened with Carbon Fiber Reinforced Polymer Patch.*" Journal of Structural Engineering, 129(2), 186–196.

Teng, J. G., Yu, T., & Fernando, D. (2012). "*Strengthening of steel structures with fiber-reinforced polymer composites.*" Journal of Constructional Steel Research, 78, 131–143.

Tobushi, H., Yamada, S., Hachisuka, T., Ikai, A., & Tanaka, K. (1996). "*Thermomechanical properties due to martensitic and R-phase transformations of TiNi shape memory alloy subjected to cyclic loadings.*" Smart Materials and Structures, 5(6), 788–795.

Torra, V., Isalgue, A., Auguet, C., Carreras, G., Lovey, F. C., Soul, H., & Terriault, P. (2009). "*Damping in Civil Engineering Using SMA. The Fatigue Behavior and Stability of CuAlBe and NiTi Alloys.*" Journal of Materials Engineering and

Performance, 18(5-6), 738–745.

Tsoi, K. a., Schrooten, J., Zheng, Y., & Stalmans, R. (2004). "*Part II. Thermomechanical characteristics of shape memory alloy composites.*" Materials Science and Engineering: A, 368(1-2), 299–310.

Tsouvalis, N. G., Mirisiotis, L. S., & Dimou, D. N. (2009). "*Experimental and numerical study of the fatigue behaviour of composite patch reinforced cracked steel plates.*" International Journal of Fatigue, 31(10), 1613–1627.

Turner, D. Z. (2015). Peridynamics-Based Digital Image Correlation Algorithm Suitable for Cracks and Other Discontinuities. Journal of Engineering Mechanics, 141, 1–10.

Tyber, J., McCormick, J., Gall, K., DesRoches, R., Maier, H. J., & Abdel Maksoud, A. E. (2007). "*Structural Engineering with NiTi . I: Basic Materials Characterization.*" Journal of Engineering Mechanics, 133(9), 1009–1018.

Vardar, Ö. (1988). "*Effect of single overload in FCP*." Engineering Fracture Mechanics, 30(3), 329–335.

Wang, H., Wu, G., Wu, Z., & Asce, M. (2014). "*Effect of FRP Configurations on the Fatigue Repair Effectiveness of Cracked Steel Plates.*" Journal of Composites for Construction.

Wang, Q. Y., Bathias, C., Kawagoishi, N., & Chen, Q. (2002). "*Effect of inclusion on subsurface crack initiation and gigacycle fatigue strength.*" International Journal of Fatigue, 24, 1269–1274.

Wu, C., Ling, X., Kong, W., Al-mahaidi, R., & Duan, W. (2013). "*Effect of fatigue loading on the bond behaviour between UHM CFRP plates and steel plates.*"

Composites : Part B, 50, 344–353.

Wu, C., Zhao, X., Hui Duan, W., & Al-Mahaidi, R. (2012). "*Bond characteristics between ultra high modulus CFRP laminates and steel.*" Thin-Walled Structures, 51, 147–157.

Xiang, Y., Lu, Z., & Liu, Y. (2010). "*Crack growth-based fatigue life prediction using an equivalent initial flaw model. Part I: Uniaxial loading.*" International Journal of Fatigue, 32(2), 341–349.

Yu, Q. Q., Chen, T., Gu, X. L., & Zhao, X. L. (2016). "*Boundary element analysis of edge cracked steel plates strengthened by CFRP laminates.*" Thin-Walled Structures, 100, 147–157.

Yu, Q. Q., Chen, T., Gu, X. L., Zhao, X. L., & Xiao, Z. G. (2013). "*Fatigue behaviour of CFRP strengthened steel plates with different degrees of damage.*" Thin-Walled Structures, 69, 10–17.

Yu, Q., Chen, T., Gu, X., Zhao, X., Asce, F., & Xiao, Z. (2015). "*Boundary Element Analysis of Fatigue Crack Growth for CFRP-Strengthened Steel Plates with Longitudinal Weld Attachments.*" Journal of Composites for Construction.

Zhang, Y., & Zhu, S. (2008). "*Seismic Response Control of Building Structures with Superelastic Shape Memory Alloy Wire Dampers.*" Journal of Engineering Mechanics, 134(3), 240–251.

Zheng, B., & Dawood, M. (2016). "*Debonding of Carbon Fiber–Reinforced Polymer Patches from Cracked Steel Elements under Fatigue Loading.*" Journal of Composites for Construction.

Zheng, X., & Hirt, M. (1983). “*Fatigue crack propagation in steels.*” Engineering Fracture Mechanics, 18(5), 968–973.

Appendix A SMA activation data

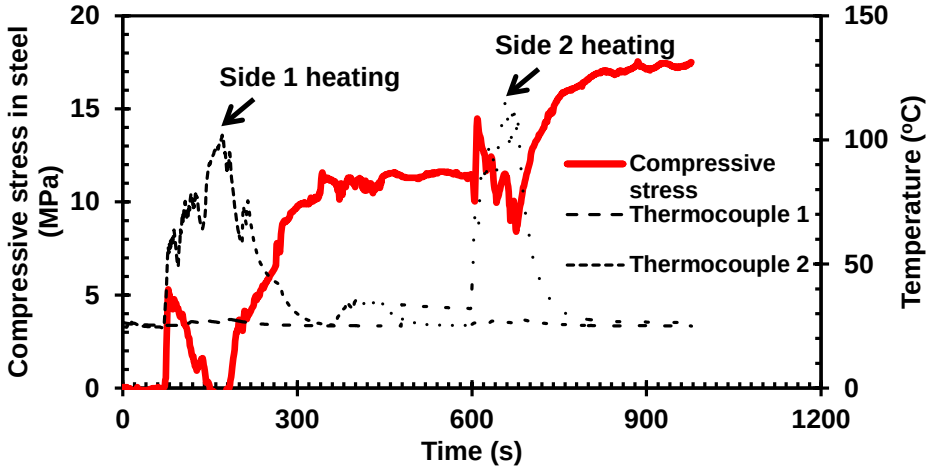

Figure A.1 SMA activation of SMA/CFRP-217-1

Appendix B DIC data of SMA/CFRP group of specimens

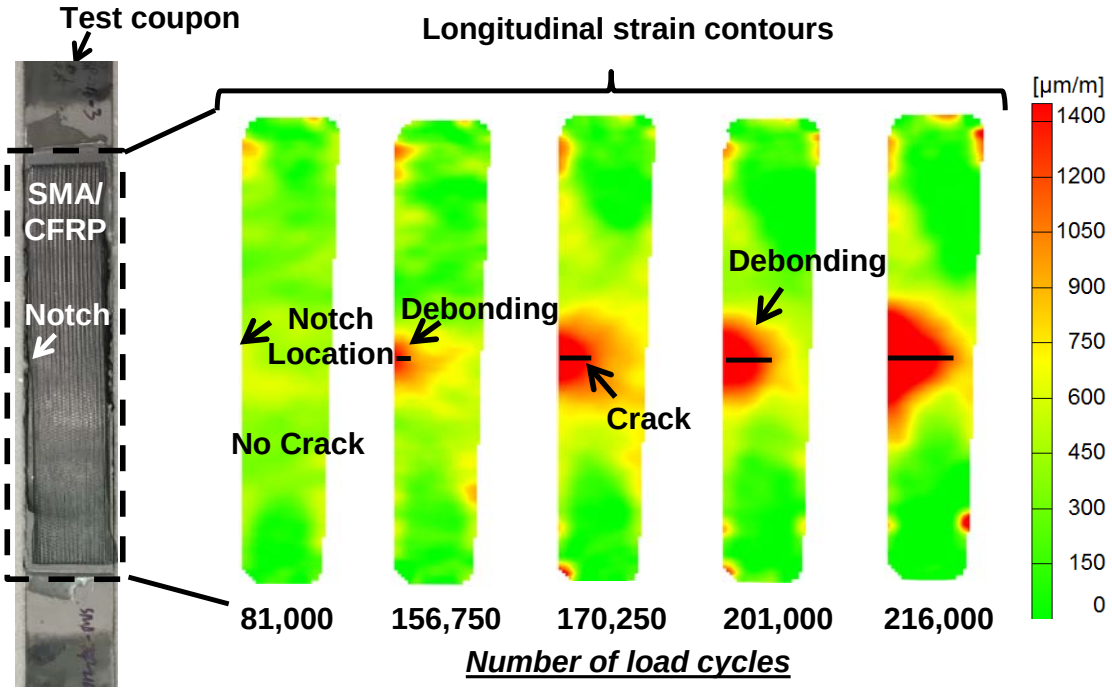

Figure B.1 SMA-CFRP-217-1

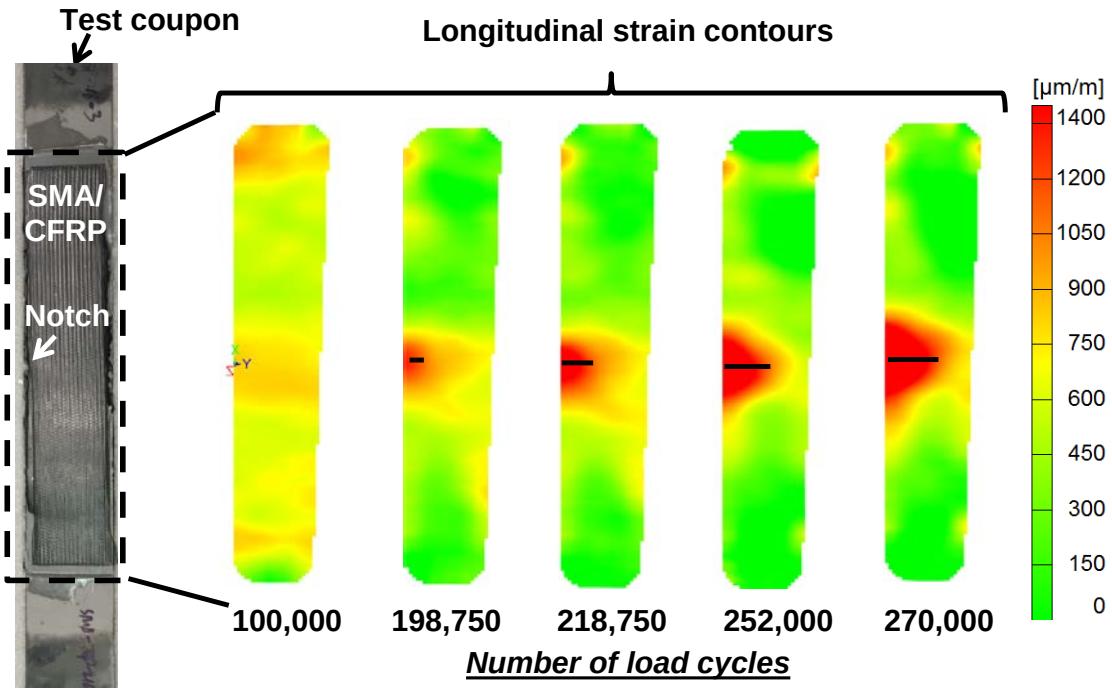

Figure B.2 SMA-CFRP-217-2

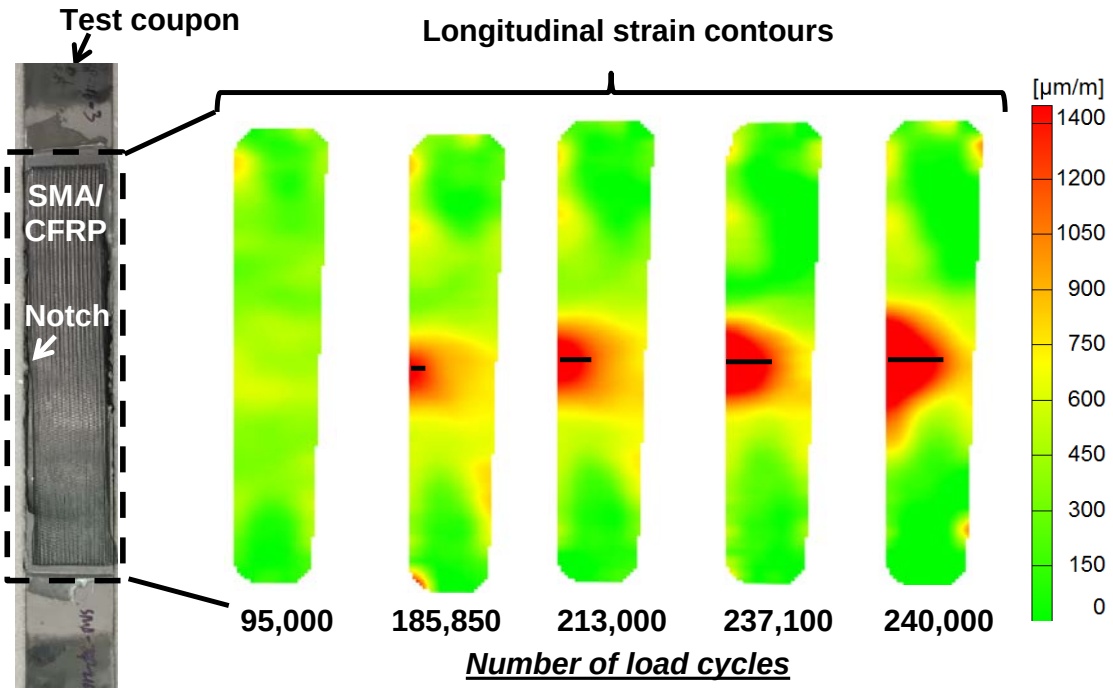

Figure B.3 SMA-CFRP-217-3

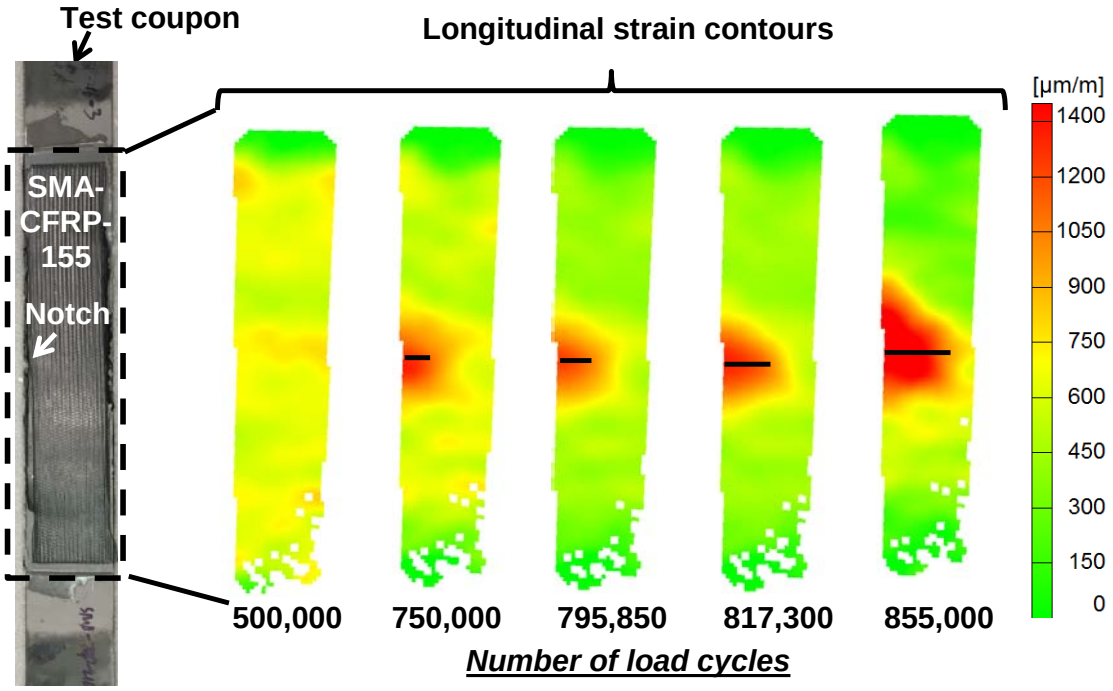

Figure B.4 SMA-CFRP-155-1

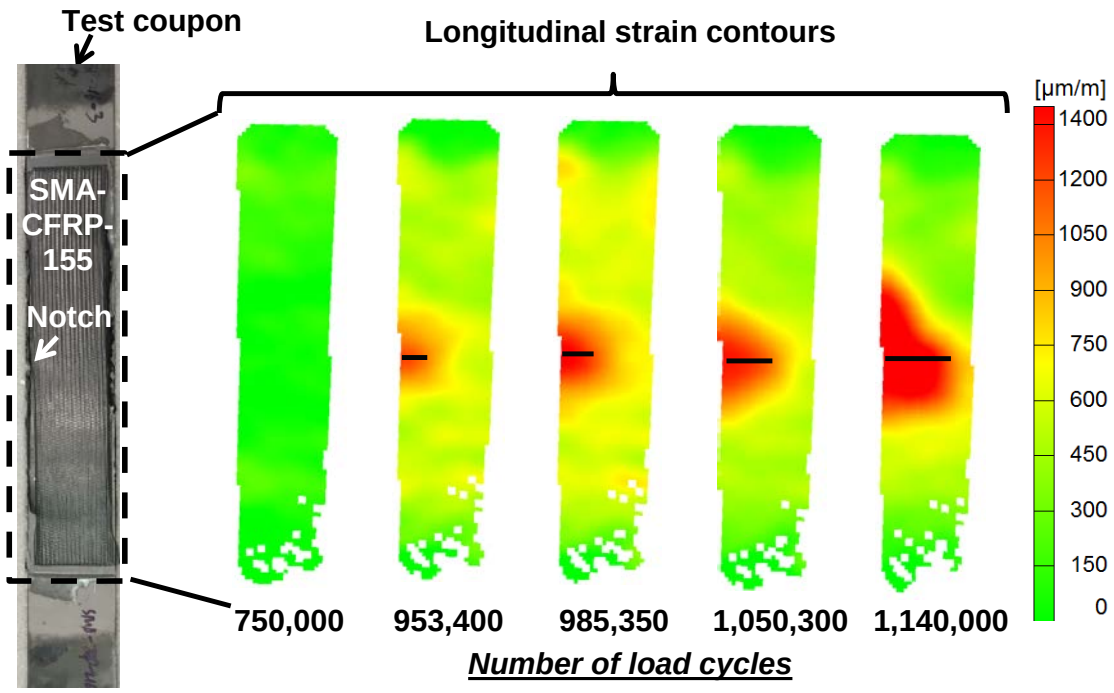

Figure B.5 SMA-CFRP-155-2

Appendix C DIC data of CFRP group of specimens

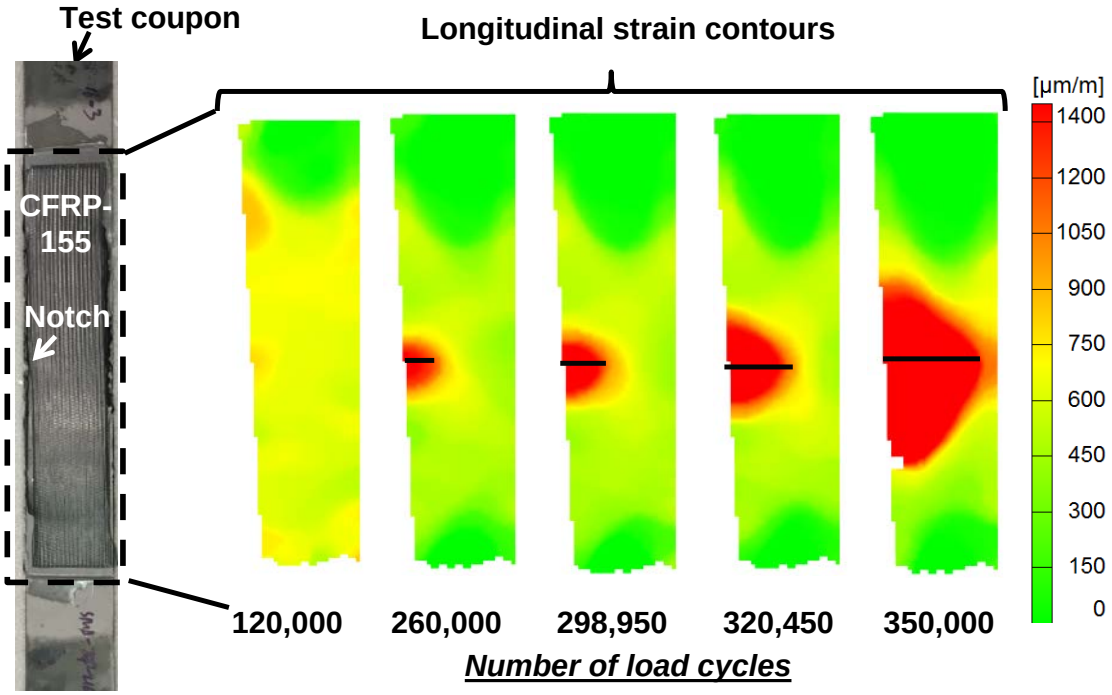

Figure C.1 CFRP-155-1

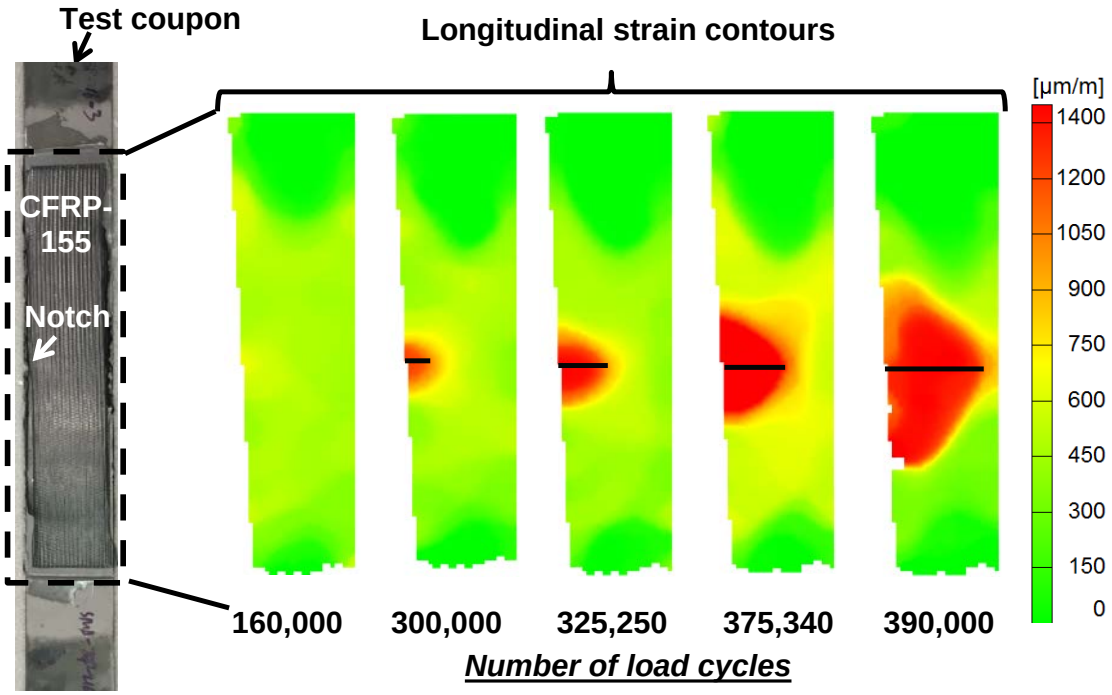

Figure C.2 CFRP-155-2